Metal Oxide Semiconductor Materials for Photo-oxidation of Water and Organic Amine Groups

by

Kayla J. Pyper

A dissertation submitted in partial fulfillment
of the requirements for the degree of
Doctor of Philosophy
(Chemistry)
in the University of Michigan
2015

Doctoral Committee:

Associate Professor Bart M. Bartlett, Chair
Professor Mark Banaszak Holl
Professor Joanna Millunchick
Professor Vincent Pecoraro

To Jesus my Savior, my family, and my youth pastor Patrick D. McGoldrick

ACKNOWLEDGEMENTS

Firstly, I would like to start by acknowledging that I have not accomplished this feat by any strength of my own. All of my strength, knowledge, and understanding has come from my Lord and Savior Jesus Christ. He is the only reason I am able to wake up every morning and He is the only one I live and breathe for. Thank you Lord for the knowledge and endurance you have given me to complete this degree.

Secondly, I could not have made it through without the love and support of my family. It has become abundantly clear these past five years that I have the best family in the entire world. Mom and Dad, thank you for the endless support and prayer you have provided me. Mom, you have always worked so hard and have been so selfless and I am so grateful for you. Thank you for being a picture of Christ's abundant love and charity. It has deeply impacted the way I approach the world. Thank you for the countless hours you spent coming out to visit me in Ann Arbor. Dad, you are the spiritual leader and I have always looked up to you and respected you for all you have done for our family. Thank you for the many spiritual conversations and wisdom over the years. I am like you in so many ways and I would not trade it for the world. The excitement we share in discussing the scriptures and what the Lord is teaching us is something that will never wax or wane. Joshua, you are my brother. That is all. Just kidding. We have become increasingly close as we have gotten older and I know it is due to the fact that we are both

becoming more like Christ. Thank you for the advice, love and support you and Gretchen have given me. I love you all very much.

The support of my entire family is not one to be missed. Grandma Jean and Grandpa John, I am happy to share your name and I thank you for raising my dad to be the Christian man he is today so that I too can share in the glory of our Savior as a result of it. You have been the most supporting and loving grandparents. Grandpa and Grandma Lewis, thank you for being such a big part of my life. Your affection and encouragement have been a blessing to me. To the rest of my family and cousins, I could not ask for a better clan. I love you all.

I also need to thank those who believed in me and helped me get to graduate school to complete this journey. Mr. Amick, you were a great high school science teacher. Who would have thought I would end up here? Mr. H, you were a great junior high science teacher, role model, coach and class sponsor. Thank you for investing in me since I was a tot and GO BLUE! Dr Ross, you were the best chemistry teacher I could have asked for. Thank you for pushing me and believing in me at Cottey. Dr. Powell, there are so many thanks in order. Thank you for being not only my research mentor at ACU, but also a spiritual mentor. As I was far from home you took me in as one of your own. I am ever grateful that you invited me into your home for thanksgiving meals and always represented a listening ear. Because of you I found out that grad school in chemistry was an actual thing that people did. I was really worried about grad school and that I wasn't ready or smart enough and I will never forget the story you told me and the advice you gave me. You told me a story about one of the smartest students you had from ACU in the past 20 years. You told me she dropped out because it was really difficult and

research was unlike anything she encountered up to this point and the failure rate of projects and progress was high. You looked me in the eye and said “Kayla, grad school isn’t about how smart you are. It is about endurance. At one point or another everyone feels like they aren’t smart enough or good enough and if they tell you they haven’t felt like that they are lying. You may not have a good result for 6 months and then you get one good result and you may have to hang onto that good result for another 6 months. You have that endurance. Keep God number one, find a good group of Christian friends, and keep that endurance.” I couldn’t have known how much that advice would be relevant to me and help me through a lot of hard times during grad school. I am forever grateful for your mentorship at ACU, phone calls throughout grad school, and now beyond. Thank you from the bottom of my heart.

Bart, thank you for the guidance and feedback. I think we learned a lot from one another. I would not be the person or chemist I am today if I did not come through your lab. I wish you well for the future of your lab. I must also thank Kathleen Nolta for all of the support in my teaching experiences in the chemistry department. You have been a tremendous help and resource. Thank you for the opportunities and advice you have given me. I would also like to thank my committee members Professors Banaszak Holl, Vince Pecoraro, and Joanna Millunchick. Thank you for the feedback and support. I must also acknowledge the members of the Bartlett Lab. We have the best lab members hands down. Tanya, thanks for being a founding member and for all of the help back in the day when I was a newbie. Xiao, you are crazy, but I do have to say I’m glad I know you. Joe, thank you for being my mentor in lab. You taught me so much and filled in to teach me a lot of things that weren’t necessarily your job to teach me. Your success is evident

because of your hard work and dedication to science. I am forever grateful for the help, the scientific discussions, and of course the many laughs. Not only were you a great labmate, but you are also a great friend. Fights and all I wouldn't have traded it. Emily, you are the best labmate, friend and confidant a girl could ask for. I loved getting to know you the past 5 years and I am so thankful for your friendship. You have taught me so much and I am always at my deepest comfort when I am hanging out with you. Ben, we've been through a lot together and it was always nice to have someone who understood what I was going through in the lab. Whether talks about science, soccer, God or life, I knew I could always count on you for a listening ear. Ben and Amy, thanks to both of you for being great friends. Jimmy, we thought you were weird at first, but soon we came to find out just how awesome you were. Thanks for being an awesome friend. You were one of the reasons I could bear showing up to lab every day because being miserable together was always better than being miserable alone. Angelo's breakfasts with you, Kim, and Emily were a highlight for sure and I shall never forget Montreal (You've got to cultivate that). Charles, thanks for being an awesome deskmate all these years, for the laughs, and the times of commiseration. Sam, Frankie (my twin), Adam, and Aaron, you guys are awesome and I'm so glad I've gotten to spend time in lab with you all. I wish everyone well in his or her future endeavors and I am so blessed to have all of my labmates as friends. Last but not least I need to thank some undergraduates. Joshy, thanks for being an awesome undergrad and friend even though you weren't my undergrad. We had a ton of fun and Joe always got mad at us, which made it even more fun. Taylor, you were an awesome undergrad and I hope you learned a lot while working in our lab. I enjoyed mentoring you and I wish you well as you finish up grad school and

go on to future chemistry endeavors. Scotty B, we had a lot of fun in lab and I will miss your weirdness. Thanks for bringing fun back to lab and being a good friend. Elayne, Scott T., Wes, and Kris, you guys are great and it was fun having you around. I wish all of you well with your future endeavors.

Lastly I want to thank all of the friends that helped me get through grad school. Shawn Eady, I feel like we were down in the trenches since the beginning. We were always working on homework and had many late nights in the lab. Thanks for always being someone to talk to and a great friend. Evonne Koo, you are one of my dearest friends and I could not imagine this journey without you. You are a constant by my side supporting me, encouraging me, and spurring me on toward Christ. Thank you for your friendship. Stephen and Sarah Canfield, thank you for the support and prayer and advice as I have navigated through grad school. Ryan and Bekah Wallace (and Hannah), you have made such an impact on my life. Thank you for investing in me and displaying the truth of Christ in front of me. I am blessed to have your friendship as we walk along side one another. Stella, I am so thankful God gave us one another and that we have kept in touch and grown as friends all of these years. You are an amazing friend and I could not ask for more support or love. Dena and Patrick McGoldrick, the influence you have had on my life is immeasurable. Thank you to my Grace Ann Arbor family and community group, Jordan Goeglein, Jess Kempf, Madelyn, Rosemarie, Yasmin, Aaron, Earl and Nancy, Esther, Julie, Steve, Jay. Thank you to those who have supported me from afar all along. Karen and Ken Kopchick and Kimberly, Lisa and Allen Kotal and Valerie, Kim and Alan Lyons

TABLE OF CONTENTS

LIST OF TABLES

LIST OF APPENDICES

ABSTRACT

With environmental decline due to increasing CO_2 and pollution levels, sustainability and ecofriendly improvements are necessary to maintain quality of life here on earth. In order to move in this direction, new sources of energy must be identified and sustainable methods must be realized. The overarching themes of sustainable energy addressed in this thesis are developing clean fuel, advancing energy efficiency, and advancing clean energy. These themes lend toward removal of our current reliance on unclean sources like oil and coal, and useless nonrenewables, toxic substances, and chemical waste. The future energy source we chose to focus on is hydrogen by photoelectrochemical water splitting using metal oxide semiconductors and visible sunlight. To advance clean energy we have chosen to focus on a greener approach to organic oxidations, specifically amine oxidation, by use of a semiconductor metal oxide and visible sunlight.

With a Z-scheme approach for water splitting the central material focused on this work is $CuWO_4$, an *n*-type visible- light absorbing semiconductor, for the water oxidation half reaction. An emphasis is also placed on the use of $CuWO_4$ to provide sustainable pathways for organic amine oxidation reactions. Another *n*-type material from the tungstate family, α-$SnWO_4$, was also synthesized and explored for sustainable water oxidation.

$CuWO_4$ was evaluated for mechanistic insight into water oxidation under visible-light illumination. Electrode construction and electron transfer was probed by inserting single-layer graphene between the conductive substrate and $CuWO_4$. A higher current density was produced with inclusion of graphene, which resulted in a smaller resistance to water oxidation at the surface. This resistance was measured and determined by electrochemical impedance spectroscopy (EIS). Increasing the thickness of $CuWO_4$ photoelectrodes to increase the number or photogenerated carriers led to no enhancement in water oxidation rate, so the carrier dynamics near the photocurrent onset were probed by EIS as a function of illumination intensity, buffer concentration, and pH to elucidate mechanistic information. A mid-gap energy state (rather than the valence band) was identified as the carrier source in the water oxidation reaction on the surface of polycrystalline sol-gel $CuWO_4$ electrodes. This state is likely composed of Cu(3d) character, and may be a direct result of Jahn-Teller distortion due to d^9 Cu^{2+}, or it may be caused by underbonding termination at the crystal surface. Similar experiments carried out on (010) single crystals of $CuWO_4$ also confirm a mid-gap state interaction.

Although the partially filled d shell may slow down the four-electron oxidation of water, these less oxidizing Cu-based holes may be beneficial for chemoselective organic oxidation reactions. As a test reaction, we have chosen primary amine oxidation (benzylamine) on $CuWO_4$ as a photoelectrode and photocatalytic powder in nonaqueous solution. $CuWO_4$ performs benzylamine oxidation to benzylidenebenzylimine with 89% Faradic efficiency, which was confirmed by gas chromatography.

The best way to improve materials for water oxidation is to identify more in depth information on how the reaction takes place on the material surface. These EIS studies on

$CuWO_4$ have provided us with chemical information to improve the reactivity of $CuWO_4$. It has also expanded the scope to a subset of organic reactions potentially catalyzed by these Cu^{2+} sites with orbital energies within the band gap.

Chapter 1

Introduction

1.1 Sustainability and the Great Energy Ultimatum

There are environmental consequences for the fossil fuel exploitation of the 20th century such as pollution and greenhouse gas emission. Coal is an abundant, cheap resource, but it is the most environmentally unclean fuel, causing an overwhelming climatic impact. CO_2 levels and pollution overwhelm busy areas that rely on electricity, transportation, and plant production all from coal production and consumption as well as fossil fuel consumption. As governmental authorities place emission limits on harmful emissive gases a change in energy source will be required. The demand for new energy sources will not be due to running out of coal or oil at the present time, but will demand change to maintain quality of life on our earth.

Solar energy is an alternative energy form that can replace coal and fossil fuels and is green, abundant, and a source long lasting source of energy. Solar energy can be broken up into subcategories of solar thermal conversion, solar electricity, and solar fuels. Other renewable energy sources include wind and hydroelectric energy. Solar thermal conversion involves the heating of liquid to supply hot water or heat in the home. These types of systems are attractive because they do not require concentrated sunlight and are not complex to construct and implement. Replacing fossil fuels with solar energy

as a means of heating water reported the prevention of the production of 25-30 million tons of CO_2.[1] Research in this area focuses on developing and testing materials that are resistive to corrosion and can withstand high temperatures.

Photovoltaic (PV) cells encompass the most promising method for solar electricity. A PV cell consists of a semiconductor able to absorb photons from the sun in which electrons and holes are created and travel to opposite electrodes where current is generated and electricity is captured. According to NREL (national renewable energy laboratory), efficiencies have been reported up to 45.7% for concentrator photovoltaic (CPV) systems where 234 suns were used.[2] Dye sensitized solar cells (DSSCs) are also developing for solar to electrical conversion (highest reported efficiency 11.9% according to NREL) that consist of a photosensitized semiconductor in contact with an electrolyte and redox shuttle that regenerates the dye on the surface.[3]

Solar research in PVs and DSSCs are important and gains in efficiency are still critical. However, liquid fuels generated from solar energy conversion are the most sought after due to transportation and storage capabilities. This approach uses the sun's energy and abundant, affordable, robust materials, such as water and metal oxides, and is the main type of solar energy I will focus on. The goal is to use the sun to split water into oxygen and hydrogen, via a metal oxide semiconductor photocatalyst, in order to store chemical energy in the form of hydrogen bonds. Water splitting entails two molecules of water producing one molecule of oxygen and two molecules of hydrogen (Equation 1) and can be separated into two half-cell reactions (Eq. 2 and 3).[4]

$$2H_2O + h\nu \rightarrow O_2 + 2H_2 \qquad (1)$$

$E^\circ = 1.23$ V vs NHE $\qquad 2H_2O \rightarrow O_2 + 4H^+ + 4e^- \qquad (2)$

$E°$ = 0 V vs NHE $\quad 2H^+ + 2e^- \rightarrow H_2 \quad$ (3)

A visible light absorbing semiconductor, with an adsorbed water molecule, reduces the overpotential to drive this endergonic reaction.[5]

1.2 Semiconductors for Water Oxidation

There are five key characteristics a selected semiconductor should possess to carry out overall water splitting (both hydrogen evolution and oxygen evolution half reactions): 1) A band gap, E_g, no greater than 2 eV to exploit the amount of visible light offered by the solar spectrum; 2) the valence band (VB) and conduction band (CB) must energetically straddle the two half reactions; 3) chemical stability in a highly oxidizing environment 4) high surface area and numerous surface catalytic sites; 5) suppression of recombination.[4,5]

The electronic structure requirements for this reaction have been in place for the past 40 years, yet the most efficient semiconductor systems still remain at very low percentages. Various semiconductors possess suitable band structures for water splitting, however, inherent problems exist that hinder their usefulness. For example CdS (E_g = 2.5 eV) is visible light responsive and contains appropriate band positions, but upon the harsh conditions of water oxidation decomposes as S^{2-} is preferentially oxidized to S_8^0 ($E^o_S{}^{0/2-}$ = +0.14 V).[6] Therefore, an important focus is on metal oxides due to their chemical inertness. A stable metal oxide capable of water splitting is TiO_2, but contains an overall band gap of 3.0-3.2 eV suffering from absorption of only ultraviolet light.[7] Based on the requirements, the performance of overall water splitting using a single material is demanding, therefore the approach is to separate the two half reactions into separate cells. Thus the photoelectrons generated at the anode (i.e. photoanode) will be transferred to a

redox mediator, such as $[Fe(CN)_6]^{3-}$ or IO_3^-, in connection with the cell containing the photocathode to carry out water splitting at no applied bias. Therefore we will separate the two half reactions and study materials specific to water oxidation as it requires a difficult 4-electron stepwise redox process.

The first step is identifying a photocatalyst to meet the key characteristics required. α-Fe_2O_3 and WO_3 are the leading candidates for water oxidation. α-Fe_2O_3 has an appropriate band gap of 2.1 eV, yet has a very low charge carrier mobility and short diffusion length (10^{-2} $cm^2/V^{-1}s^{-1}$ and 2-20 nm) based on the localized nature of unpaired spins in compact 3d orbitals.[8,9] However, these limitations can be overcome with strict morphology control.[10, 11, 12] Conversely WO_3 (E_g = 2.7 eV) has shown high catalytic activity to oxidize water and has a charge carrier mobility and diffusion length of 10 $cm^2/V^{-1}s^{-1}$ and 150 nm respectively[13], which brings it to the forefront as a leading candidate for water oxidation. Although charge carrier mobility is much improved compared to α-Fe_2O_3, it is important to point out three large drawbacks of WO_3: 1) it has a band gap of 2.7 eV, which does not use the visible spectrum effectively; 2) it is not stable at pH > 5, where the W-O bonds are attacked to form soluble tungstates; 3) it is not selective toward water oxidation with other oxidizable anions like Cl^- in solution.[13] It is still advantageous to use WO_3 as a guide because it has been extensively studied in the literature. Also, it remains in our best interest to use the strengths of WO_3 (high photocatalytic activity to oxidize water and carrier mobility), while realizing that a more stable, selective, visible light responsive compound is required. In that case moving to metal tungstates is desirable, as the CB may still comprised of W 5d orbitals, yet we now benefit from a more energetically favorable VB.

Our lab has specifically targeted metal tungstates (AWO_4, A=Cu, Sn), which possess a CB of W 5d orbitals (located below the proton reduction potential, E° = 0 V vs NHE) and a VB comprised of metal and oxygen orbitals, unlike WO_3 in which the VB is only comprised of oxygen. Therefore, I will focus on how the incorporation of metal orbitals to the valence band, specifically Cu and Sn, alters the performance of water oxidation at the surface of these materials. I will also focus on electrode construction.

1.3 $CuWO_4$ as a Photoanode

$CuWO_4$ is an *n*-type material with VB composed of O(2p) and Cu(3d) orbitals and conduction band of W(5d) character and likely Cu(3d) character. Due to its ability to absorb visible light with a band gap, E_g, of 2.3 eV and appropriate valence and conduction band edges (+2.7 V and +0.4 V *vs* RHE respectively) $CuWO_4$ has been synthesized in our lab as a photoanode for water oxidation. It has been deposited onto fluorinated tin oxide (FTO) using electrodeposition by co-depositing copper and tungsten using precursors of $Cu(NO_3)_2$-nH_2O and $H_2W_2O_{11}$ using cyclic voltammetry.[14] The band gap was identified as indirect with E_g = 2.3 eV by UV-Vis spectroscopy. The ligand to metal charge transfer bands was identified at 391 nm, with a Cu-W metal to metal charge transfer band occurring as a shoulder at ~450 nm.[15] Since Cu^{2+} is d^9, localized *d-d* transitions were also identified from 700-800 nm. The d^9 configuration of Cu^{2+} in this ternary phase distinguishes it from the typical d^0 materials such as WO_3, TiO_2, and $BiVO_4$.

$CuWO_4$ has also been deposited onto FTO by sol-gel spin coating after heating a mixture of $Cu(NO_3)_2 \bullet 3H_2O$ and ammonium metatungstate in an ethylene glycol/water solution. The band gap was identified as 2.45 eV due to the thin nature of the electrodes

(200 nm *vs* 2-3 μm for electrodeposited $CuWO_4$). The $CuWO_4$ sol-gel electrodes generate oxygen from water with 100% and 96% Faradaic efficiency in potassium phosphate and potassium borate buffers respectively, and are highly stable in potassium borate buffer at pH 7 (93% of the initial photocurrent is retained after 12 h of continuous illumination at 1.23 V *vs* RHE).[16] Despite the difference in thickness the sol-gel films showed similar activity to that of electrodeposited $CuWO_4$. An indirect band gap material requires a thicker absorber layer due to extra momentum from a phonon required to excite the electron into the CB. However, increasing the thickness of the sol-gel $CuWO_4$ layer only resulted in lower photocurrent profiles. It should be pointed out that these electrodes are polycrystalline and therefore increasing the thickness likely increases recombination at these domain interfaces. There are many possibilities as to why an improvement is not observed such as low conductivity, low mobilities, material defects, recombination due to polycrystallinity, and recombination at the solution surface as well as recombination at the conductive substrate.

1.4 Methods for Improvement of Electrode Construction

Suppression of recombination in semiconductor materials is an important property to control in photoelectrochemical applications.[17,18] There are many reasons to study charge transfer in electrochemical systems, which include the ability to obtain kinetic information, the identification of resistance to charge transfer at an interface, or the route of recombination of charges to name a few.[19] Polycrystalline semiconductor materials are used for a variety of systems such as p-n junctions,[20] photovoltaics,[21] LEDs,[22] solar cells,[23] and water splitting applications,[24] as a result of their abundance, low cost and compatibility. However, due to polycrystallinity and low conductance, recombination is

prevalent especially when employed for multi-electron processes.[25] When a $CuWO_4$ electrode is placed in solution the interaction with solution is described by Figure 1.1 where the bands bend at the surface to equilibrate with the water oxidation half reaction. Some common examples of recombination are also shown in this figure as a) interfacial electron transfer over the electrochemical potential barrier, b) tunneling through the electric potential barrier, c) in the near surface region, d) in the depletion region, and e) in the bulk quasi-neutral region.[26]

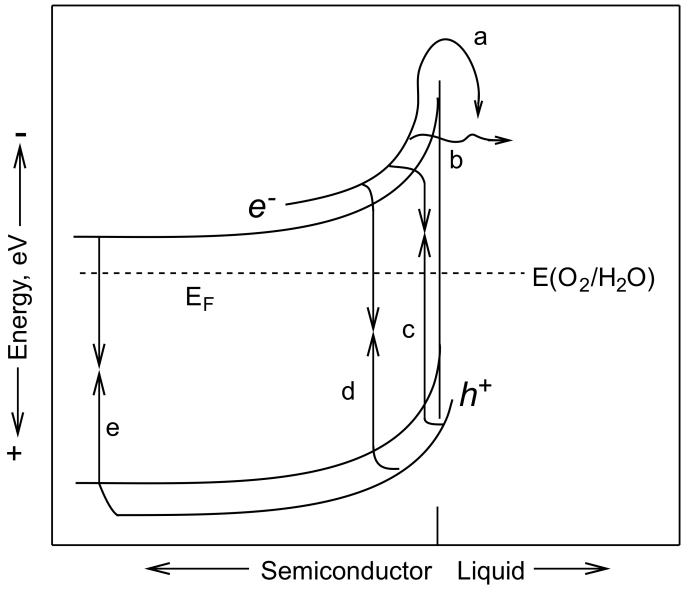

Figure 1.1 Band bending at an n-type semiconductor-solution interface where VB is the valence band and CB the conduction band. E_F describes the Fermi level equilibrated at 1.23 V, the thermodynamic potential of water oxidation. Recombination pathways a-e are discussed in the text. Electron and hole are represented after excitation as e^- and h^+.

Many advances have been made to support metal oxide films or nanoparticles with a co-catalyst to prevent surface recombination by providing a separate reaction site for either holes or electrons. For example, a cubane-like cluster of cobalt oxide stabilized by phosphate (CoP_i) has been photodeposited onto the surface of Fe_2O_3,[27] $BiVO_4$,[28] WO_3[29] acting as a hole scavenger preventing detrimental surface recombination due to

slow surface kinetics associated with the 4-proton and 4-electron water oxidation reaction. Aside from recombination at the semiconductor-solution interface another possible energy loss mechanism is recombination at the conductive substrate or Ohmic contact.[30] Fluorinated tin oxide (FTO) is the standard conductive substrate used for analysis of thin films in the field of photoelectrochemical water splitting because it is transparent over the entire solar spectrum and inexpensive. It is used as an Ohmic contact to semiconductor materials deposited onto it, in which an Ohmic contact is defined as one where there is an unimpeded transfer of majority carriers from one material to another, i.e., the contacts do not limit the current.[31] The way to achieve such a contact is by doping the semiconductor heavily enough that tunneling is possible (tin oxide heavily doped with fluorine). Ohmic contact between the semiconductor and conductive substrate requires equilibration of the Fermi level (Figure 1.2a), and poor equilibration results in Fermi level pinning, thus generating a Schottky barrier at the substrate-semiconductor junction (Figure 1.2b).[32] Therefore, it is possible that FTO does not create an Ohmic contact but instead creates a Schottky barrier at the FTO-semiconductor interface which provides resistance to electron transfer across this junction. Since all semiconductors likely suffer from recombination whether at the contact or on the surface, the focus becomes that of prevention. For this reason, we have explored the use of graphene as an interlayer to improve charge transfer at the substrate-semiconductor interface to ultimately improve the ability to perform water oxidation on the surface.

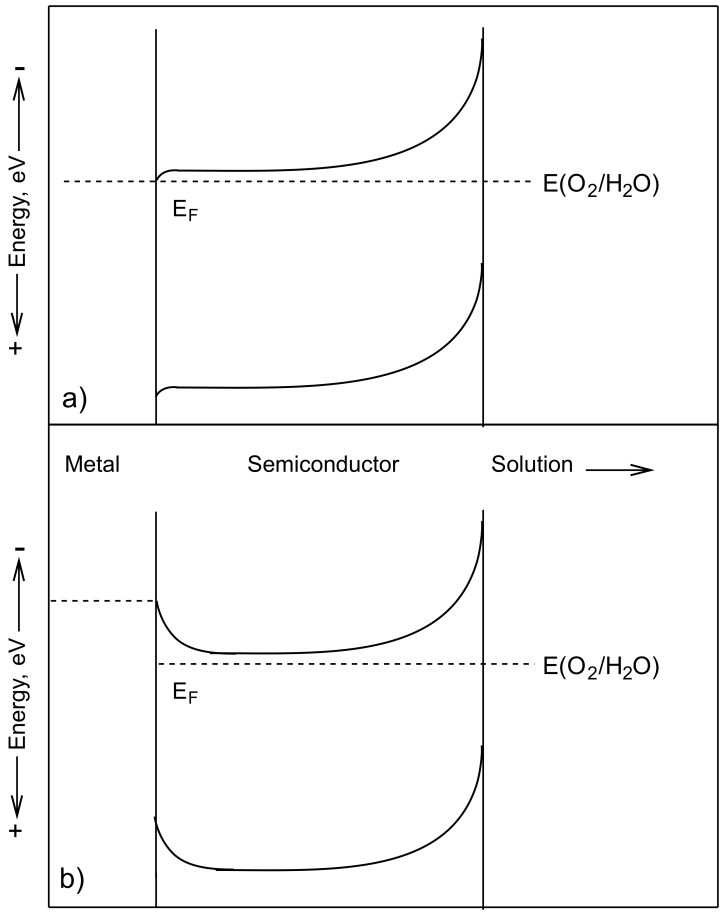

Figure 1.2 Band bending highlighted at the substrate (metal or FTO in our case)-semiconductor for an a) Ohmic contact and b) Schottky contact.

Graphene composites have gained attention in many applications such as batteries,[33] gas sensing,[34] oxygen reduction[35] and electrocatalysis[36] due to its exceptional electron mobility (as high as 200,000 $cm^2/V^{-1}s^{-1}$ at T=20K)[37] and high conductivity compared to the mobilities observed in metal oxides (10^{-3} – 10 $cm^2/V^{-1}s^{-1}$)[38] due to its sp^2-hybridized two-dimensional carbon network, resulting in an abundance of delocalized electrons. These characteristics, coupled with its high specific surface area (2630 m^2g^{-1}),[39] make it an advantageous material for improving charge transfer. Most composites have been formed by the use of graphene oxide and various graphite exfoliation techniques. The exploration of graphene in the field of photoelectrochemical water

splitting has so far mainly focused on the synthesis of metal oxide/graphene powder composites. Specifically, WO_3@graphene composite powders have been synthesized for oxygen evolution by Guo et al producing 388 μmol L^{-1} for the WO_3@GR composite and 186 μmol L^{-1} for the WO_3 control.[40] Other powder composites of Bi_2WO_6/graphene and TiO_2/graphene have also been shown to more efficiently perform dye degradation than without the graphene support.[41]

One example in the literature of metal oxide/graphene films consists of a general study using composites of TiO_2 (Degussa P25), WO_3, and $BiVO_4$ showing improved current when graphene was included.[42] A $BiVO_4$ film composite by Ng et al. shows more photocurrent is produced by a film that has been constructed from metal oxide/graphene composite powder than with the powder electrode alone.[43] In order to electrochemically characterize any enhancement made with graphene; these materials (with and without graphene) must be made into an electrode and tested, which is the focus of my second chapter. The characteristics and engineering of photoelectrodes becomes increasingly important to minimize losses that will affect overall efficiency.

1.5 Water Oxidation at the Surface of $CuWO_4$

During the process of testing these $CuWO_4$ films with a graphene interlayer it was thought that W(5d) alone contributed to the CB with a hybridized O(2p) + Cu(3d) VB. However a cyclic voltammogram of $CuWO_4$ seemed to suggest Cu(3d) states dominating the bottom of the conduction band. $CuWO_4$ has a distorted wolframite structure and is in the space group *P*-1 and due to the Jahn-Teller distortion of the CuO_6 octahedra it would not be unlikely to observe Cu(3d) character near the CB edge or even within the gap. DFT calculations by Lalić *et al*,[44] provide theory that is in alignment with Cu(3d) states

composing the top of the VB and also the bottom of the CB. The Jahn-Teller distortion of Cu^{2+} gives rise to a d-orbital splitting in which the degeneracy of the σ-antibonding orbitals is broken[45] and in the spin-polarized Pauli model, the singly-occupied d_{x2-y2} orbital splits.[46] Although a graphene interlayer could improve charge transfer at the substrate, if localized Cu(3d) bands below the CB are dominating the mechanism for oxygen evolution, then we would continue to observe low performance as we increased the thickness of the $CuWO_4$ layer. Therefore in chapter 3 of this thesis I will not only discuss how these Cu(3d) orbitals may contribute to the VB, but I will also discuss how the splitting of the Cu(3d) orbitals introduce efficiency loss via a Cu(3d) mid-gap state. As mentioned briefly, cobalt oxide or cobalt oxide stabilized by phosphate has been deposited onto metal oxide surfaces like that of Fe_2O_3,[47] $BiVO_4$,[48] WO_3[49] acting as a hole scavenger preventing detrimental surface recombination due to slow surface kinetics associated with the 4-proton and 4-electron water oxidation reaction. However, when these cobalt oxide species are deposited onto $CuWO_4$, there is a decrease in photocurrent observed for the water oxidation reaction. This decrease is likely due to the role of these Cu(3d) orbitals within the gap preventing the oxidation of Co^{3+} to Co^{4+} therefore rendering it much less active for water oxidation.

1.6 Other Tungstates for Water Oxidation: α-$SnWO_4$

In order to remove the localized d-orbital contribution to the electronic structure we focused our attention on α-$SnWO_4$, which is an orthorhombic *n*-type material belonging to the space group *Pnna*, and contains Sn atoms positioned in between layers of corner-sharing WO_6 octahedra. Unlike $CuWO_4$, it possesses a closed *d* shell, which inhibits the possible loss of energy through trap states and therefore potentially increases

mobility similar to its tungsten-containing counterpart, WO_3. Overall, there has not been extensive research focusing on α-$SnWO_4$ for overall water splitting or water oxidation, however theory suggests an E_g < 2.0 eV. Cho *et al*. has performed DFT calculations and shown the predicted E_g to be 1.65 eV with suitable band energies for water oxidation.[50] This small predicted band gap is extremely significant because as other previously studied semiconductor materials as I mentioned either have too large a band gap (TiO_2, E_g = 3.2 eV) or a small band gap (CdSe, E_g = 1.7 eV) that is not stable towards water oxidation. Another compound that has been widely studied for its small band gap (E_g = ~2.3 eV) and high photocatalytic activity is $BiVO_4$.[51] In this compound, the contribution of bismuth raises the VB to decrease the E_g. α-$SnWO_4$, which is isoelectronic to $BiVO_4$, is calculated to have a CB comprised of W 5*d* and Sn 5*p* character, while the VB consists of O 2*p* and Sn 5*s* orbitals. The effective mixing of the Sn 5*s* and O 2*p* orbitals raises the VB and results in an overall smaller band gap.

Despite its calculated band gap of 2.5 eV,[52] there are several synthetic challenges for producing α-$SnWO_4$ due to the relative instability of Sn^{2+} compared to Sn^{4+}. Several groups have produced powder samples of orthorhombic α-$SnWO_4$ as well as cubic β-$SnWO_4$ by calcining in either an inert or vacuum atmosphere as well as by hydrothermal processes[53 54]. Inert or vacuum atmosphere is necessary because Sn^{2+} is readily oxidized to Sn^{4+} in air. There are examples of forming α-$SnWO_4$ by hydrothermal synthesis methods using surfactants under milder, less oxidizing conditions[55]. However, these syntheses start from an amorphous precipitate having a 1:1 Sn:W ratio. Therefore synthetic methods with these restrictions become increasingly more complicated when

extrapolated to thin film synthesis. The focus of chapter five is developing a novel thin film synthesis of α-$SnWO_4$ to test as a photoanode for water oxidation.

1.7 Use of Metal Oxides for Sustainable Organic Transformations

In addition to researching alternative energies to help solve future energy crises, there are ways we can focus our attention on processes that may be implemented here and now. One of those ways is greener methods and alternatives to oxidation of organic compounds. The environmental impact of many organic transformations relates to 1) use of external sacrificial oxidants, 2) expensive catalysts and catalytic supports, 3) low catalyst lifetimes 4) and high temperatures. Specifically as an example and outlook, I will focus on the oxidation of a primary amine group to its respective imine. Compared to the biomimetic or enzymatic reactions of amine oxidation, industrial processes for these reactions require external oxidants and reactions temperatures often times over 100 °C.[56] Amine oxidations are important from the standpoint of not only improving synthetic organic processes, but also biological implications. We focus on addressing each problem above by utilizing semiconductor photocatalysts. Specifically, visible light absorbing metal oxides can alleviate the issues by 1) removal of waste—generating external oxidants by using only O_2, 2) use of abundant, cheap semiconductor catalysts 3) durable and reusable metal oxides and 4) use of sunlight to drive the reaction.

TiO_2 has been studied for a wide range of applications especially within the field of photocatalysis. It has been exploited for alcohol and amine oxidation by Zhao *et al*, in which the importance of O_2 in the catalytic cycle was realized as the mechanism goes through a benzaldehyde intermediate for both alcohol and amine oxidation.[57,58] However, the problems associated with TiO_2 when it comes to organic oxidations are overoxidation

due to the highly oxidizing 3 eV energy of the valence band holes and a large band gap (E_g = 3-3.2 eV), which only absorbs UV light.[59] Another metal oxide photocatalyst that has been used for selective amine oxidation is Nb_2O_5 in which the band gap is 3.2 eV, yet claims to use visible light up to 450 nm for alcohol and amine oxidation.[60] For both alcohol and amine oxidation, the claim is that once the alcohol or amine species binds it represents an "in situ doping" where an electron is excited from this new donor level and the reaction is propelled forward under this new visible light excitation. For this reason the authors claim the selectivity increases over Nb_2O_5 for amine oxidation (98%) over that of TiO_2 and ZnO (89% and 94%).

Designing a catalyst able to selectively oxidize an organic substrate, but not overoxidize that substrate is a need in the synthetic field. For example some common chemical oxidants used in organic reactions are permanganate ($KMnO_4$) and Cr^{6+} compounds such as H_2CrO_4 and $K_2Cr_2O_7 \bullet H_2SO_4$. With the field moving toward sustainable reaction chemistry in aqueous conditions these external oxidants will oxidize all organic groups to their most oxidized form. Also, chromates are not ideal due to their high toxicity level. For selectivity and low toxicity, homogeneous catalysts, such as Cu-based catalysts have been implemented using O_2 as an oxidant.[61,62] However, the stability and ease with which to recover the catalyst are still problems that need to be addressed with these homogenous catalysts. Selectivity issues have been addressed with both heterogeneous and homogenous catalysts. With the use of the heterogeneous catalyst $CuWO_4$, we will attempt to address some of these issues and utilize the shortcomings identified in this material for water oxidation. As discussed previously, $CuWO_4$ has a raised valence band compared to that of TiO_2 and Nb_2O_5 (2.7 eV vs 3-3.2 eV) due to the

Cu(3d) orbitals; therefore it has a lesser oxidizing power from valence band holes. The mechanistic pathway of water oxidation on $CuWO_4$ which is discussed in chapter 3 lends to a possibility for selective oxidation of alcohol groups through a similar mechanistic pathway to that of water oxidation (oxidation through Cu(3d) states within the gap) while an amine oxidation may react instead directly with valence band holes. Even if amine oxidation does in fact still take place via oxidation through use of Cu(3d) states in the gap, if there is a different kinetic reaction mechanism, selectivity may still be imparted. With a large overpotential for photoelectrochemical oxidation of water due to this mid-gap state interaction it is possible to control selectivity based on applied potential for the same mechanistic reason described above. By operation at a lower potential where there are slow kinetics to oxidize an alcohol group, selectivity in that case may be high for primary amine oxidation.

1.8 Scope of Thesis

This thesis focuses on the use of metal oxides, $CuWO_4$ and α-$SnWO_4$, to perform water oxidation and amine oxidations with a starting focus on identifying issues with $CuWO_4$ electrodes and how we can address those issues. Chapter 2 presents modification of a $CuWO_4$ electrode with GR in order to improve charge transfer at the substrate-semiconductor interface to in turn improve the rate of water oxidation at the surface. Chapter 3 focuses on the material interaction with solution by electrochemical impedance spectroscopy to better understand how $CuWO_4$ performs water oxidation. It is important to look at the shortcomings of materials like $CuWO_4$ for water oxidation so we may better know how to improve them. Chapter 4 focuses on the exploration of another tungstate material, α-$SnWO_4$ for water oxidation seeking to correct the shortcomings of

d^9 $CuWO_4$ by the use of a completely closed shell material. Chapter 5 focuses on the outlook of utilizing the shortcomings of $CuWO_4$ for organic amine and alcohol oxidation with some preliminary data presented for greener alternatives to organic oxidation of primary amines.

1.9 References

1. Armaroli, N.; Balzani, V. The Future of Energy Supply: Challenges and Opportunities Angew. Chem. Int. Ed. 2007, 46, 52-66.
2. NREL, NREL Demonstrates 45.7% Efficiency for Concentrator Solar Cell, www.nrel.gov/news/press/2014/15436.html (accessed April 2, 2015).
3. NREL, www.nrel.gov/ncpv/images/efficiency_chart.jpg (accessed April 2, 2015).
4. Currao, A. Photoelectrochemical Water Splitting Chimia 2007, 67, 815-819.
5. Kudo, A.; Miseki, Y. Heterogeneous Photocatalyst Materials for Water Splitting Chem. Soc. Rev. 2009, 38, 253-278.
6. Gerisher, H. On the Stability of Semiconductor Electrodes Against Photodecomposition J. Electroanal. Chem. 1977, 82, 133-143.
7. Fujishima, A.; Honda, K. Electrochemical Photolysis of Water at a Semiconductor Electrode Nature 1972, 238, 37.
8. Gardner, R. F. G.; Sweett, F.; Tanner, D. W. The Electrical Properties of Alpha Ferric Oxide—I.: The Impure Oxide J. Phys. Chem. Solids 1963, 24, 1175-1181.
9. Dare-Edwards, M. P.; Goodenough, J. B.; Hammet, A.; Trevellick, P. R. Electrochemistry and Photoelectrochemistry of Iron(III) Oxide J. Chem. Soc. Faraday Trans. 1 1983, 79, 2027-2041.
10. Cornuz, M.; Grätzel, M.; Sivula, K. Preferential Orientation in Hematite Films for Solar Hydrogen Production via Water Splitting Chem. Vap. Dep. 2010, 16, 291-295.
11. Cesar, I.; Sivula, K.; Kay, A.; R. Zboril, R.; Grätzel, M. Influence of Feature Size, Film Thickness, and Silicon Doping on the Performance of Nanostructured Hematite Photoanodes for Solar Water Splitting J. Phys. Chem. C. 2009, 113, 772-782.
12. Sivula, K.; Brillet, J.; Grätzel, M. Controlling Photo-Activity of Solution-Processed Hematite Electrodes for Solar Water Splitting Proc. of SPIE 2010, 7770, 77700G1-6.
13. Heumann, Th.; Stolica, N. The Electrochemical Behaviour of Tungsten—II. The Dissolution of Tungsten in NaOH Solutions Electrochim. Acta 1971, 16, 1635-1646.
14. Yourey, J. E.; Bartlett, B. M. Electrochemical Deposition and Photoelectrochemistry of $CuWO_4$, a Promising Photoanode for Water Oxidation J. Mater. Chem. 2011, 21, 7651-7660.
15. Dey, S.; Ricciardo, R.A.; Cuthbert, H.L.; Woodward, P.M. Metal-to-Metal Charge Transfer in AWO4 (A = Mg, Mn, Co, Ni, Cu, or Zn) Compounds with the Wolframite Structure Inorg. Chem. 2014, 53, 4394-4399.
16. Yourey, J. E.; Pyper, K. J.; Kurtz, J. B.; Bartlett, B. M. Chemical Stability of $CuWO_4$ for Photoelectrochemical Water Oxidation J. Phys. Chem. C 2013, 117, 8708-8718.
17. Turner, J. A. A Realizable Renewable Energy Future Science 1999, 285, 1493.

18. Bolton, J. R.; Strickler, S. J.; Connolly, J. S. Limiting and Realizable Efficiencies of Solar Photolysis of Water Nature 1985, 316, 495.
19. Bard, A.J.; Faulkner, L. R. Electrochemical Methods: Fundamentals and Applications January 2002
20. Nozik, A.J. Photochemical Diodes, Appl. Phys. Lett. 1977, 30, 567.
21. Fornarini, L.; Nozik, A.J.; Parkinson, B.A. The Energetics of p/n Photoelectrolysis Cells, J. Phys Chem. 1984, 88, 3238.
22. Zhang, X.; Liu, W.; Wei, G.Z.; Banerjee, D.; Hu, Z.; Li, J. Systematic Approaches in Designing Rare-Earth-Free Hybrid Semiconductor Phosphors for General Lighting Applications, J. Am. Chem. Soc. 2014, 136, 14230-14236.
23. Gratzel, M. Photoelectrochemical Cells Nature 2001, 414, 338-344.
24. Fujishima, A.; Honda, K. Electrochemical Photolysis of Water at a Semiconductor Electrode Nature 1972, 238, 37-38.
25. Fu, Z.; Jiang, T.; Liu, Z.; Wang, D.; Wang, L.; Xie, T. Highly Photoactive Ti-doped α- Fe_2O_3 Nanorod Arrays Photoanode Prepared by a Hydrothermal Method for Photoelectrochemical Water Splitting Electrochimica Acta 2014, 129, 358-363.
26. Serpone, N.; Pelizzetti, E.; Photocatalysis Fundamentals and Applications New York: John Wiley & Sons, Inc, 1989. Print.
27. McDonald, K.J.; Choi, K.-S. Photodeposition of Co-Based Oxygen Evolution Catalysts on α-Fe_2O_3 Photoanodes Chem. Mater. 2011, 23, 1686-1693.
28. Jeon, T.H.; Choi, W.; Park, H. Cobalt-Phosphate Complexes Catalyze the Photoelectrochemical Water Oxidation of $BiVO_4$ Electrodes Phys. Chem. Chem. Phys. 2011, 13, 21392-21401.
29. Seabold, J. A.; Choi, K.-S. Effect of a Cobalt-Based Oxygen Evolution Catalyst on the Stability and the Selectivity of Photo-Oxidation Reactions of a WO3 Photoanode Chem Mater. 2011, 23, 1105-1112.
30. Konin, A. Interface Recombination Feature in Metal-Semiconductor Junction at High Photoexcitation Semicond. Sci. Technol. 2014, 29, 095009.
31. Kröger, F.A.; Diemer, G.; Klasens, H.A. Nature of an Ohmic Metal-Semiconductor Contact Phys. Rev. 1956, 103, 279.
32. Brillson, L.J.; Lu, Y. ZnO Schottky Barriers and Ohmic Contacts J. Appl. Phys. 2011, 109, 121301.
33. Wang, G.; Liu, T.; Luo, Y.; Zhao, Y.; Ren, Z.; Bai, J.; Wang, H. Preparation of Fe_2O_3/Graphene Composite and its Electrochemical Performance as an Anode Material for Lithium Ion Batteries Journal Alloys and Compounds 2011, 509, L216-L220.
34. Qin, J.; Cao, M.; Li, N.; Hu, C. Graphene-wrapped WO3 Nanoparticles with Improved Performances in Electrical Conductivity and Gas Sensing Properties J. Mater. Chem. 2011, 21, 17167.
35. Guo, S.; Sun, S. FePt Nanoparticles Assembled on Graphene as Enhanced Catalyst for Oxygen Reduction Reaction J. Am. Chem. Soc. 2012, 134, 2492-2495.
36. Li, Y.; Zhou, W.; Wang, H.; Xie, L; Liang, Y; Wei, F.; Idrobo, J.-C.; Pennycook, S.J.; Dai, H. An Oxygen Reduction Electrocatalyst Based on Carbon Nanotube-Graphene Complexes Nature Nanotechnology 2012, 7, 394-400.

37. Du, X.; Skachko, I.; Barker, A.; Andrei, E.Y. Approaching Ballistic Transport in Suspended Graphene Nature Nanotechnology 2008, 3, 491-495.
38. Zhong, D. K.; Sun, J.; Inumaru, H.; Gamelin, D.R. Solar Water Oxidation by Composite Catalyst/α- Fe_2O_3 Photoanodes J. Am. Chem. Soc. 2009, 131, 6086-6087.
39. Rao, C.N.R.; Sood, A.K.; Subrahmanyam, K.S.; Govindaraj, A. Graphene: The Two-Dimensional Nanomaterial Angew. CHem. Int. Ed. 2009, 48, 7752.
40. Guo, J.; Li, T.; Zhu, S.; Chen, Z.; Liu, Q.; Zhang, D.; Moon, W-J.; Song, D-M. Synthesis of WO3@Graphene Composite for Enhanced Photocatalytic Oxygen Evolution from Water RSC Adv. 2012, 2, 1356-1363.
41. Min, Y.-L.; Zhang, K.; Chen, Y.-C.; Zhang, Y.-G. Enhanced Photocatalytic Performance of Bi2WO6 by Graphene Supporter as Charge Transfer Channel Separation and Purification Technology 2012, 86 ,98-105.
42. Ng, Y.H.; Iwase, A.; Bell, N.J.; Kudo, A.; Amal, R. Semiconductor/reduced Graphene Oxide Nanocomposites Derived from Photocatalytic Reactions Catalysis Today 2011, 164, 353-357.
43. Ng, Y.H.; Iwase, A; Kudo, A.; Amal, R. Reducing Graphene Oxide on a Visible-Light $BiVO_4$ Photocatalyst for an Enhanced Photoelectrochemical Water Splitting J. Phys. Chem. Lett. 2010, 1, 2607-2612.
44. Lalić, M. V.; Popović, Z. S.; Vukajlović, F. R. Electronic Structure and Optical Properties of $CuWO_4$: An Ab Initio Study Comp. Mat. Sci. 2012, 63, 163-167.
45. Ruiz-Fuertes, J.; Segura, A.; Rodriguez, F.; Errandonea, D.; Sanz-Ortiz, M. N. Anomalous High-Pressure Jahn-Teller Behavior in $CuWO_4$ Phys. Rev. Lett. 2012, 108, 166402.
46. Doumerc, J.-P.; Hejtmanek, J.; Chaminade, J.-P.; Pouchard, M.; Krussanova, M. A Photoelectrochemical Study of $CuWO_4$ Single Crystal Phys. Stat. Sol. 1984, 82, 285-294.
47. McDonald, K.J.; Choi, K.-S. Photodeposition of Co-Based Oxygen Evolution Catalysts on α- Fe_2O_3 Photoanodes Chem. Mater. 2011, 23, 1686-1693.
48. Jeon, T.H.; Choi, W.; Park, H. Cobalt-Phosphate Complexes Catalyze the Photoelectrochemical Water Oxidation of $BiVO_4$ Electrodes Phys. Chem. Chem. Phys. 2011, 13, 21392-21401.
49. Seabold, J. A.; Choi, K.-S. Effect of a Cobalt-Based Oxygen Evolution Catalyst on the Stability and the Selectivity of Photo-Oxidation Reactions of a WO3 Photoanode Chem Mater. 2011, 23, 1105-1112.
50. Cho, I.-S.; Kwak, C.H.; Kim, D.W.; Lee, S.; Hong, K.S. Photophysical, Photoelectrochemical, and Photocatalytic Properties of Novel $SnWO_4$ Oxide Semiconductors with Narrow Band Gaps J. Phys. Chem. C 2009, 113, 10647-10653.
51. Huang, Z-F.; Pan, L.; Zou, J-J.; Zhang, X.; Wang, L. Nanostructured Bismuth Vanadate-Based Materials for Solar-Energy-Driven Water Oxidation: A Review on Recent Progress Nanoscale 2014, 6, 14044-14063.
52. Lacomba-Perales, R.; Ruiz-Fuertes, J.; Errandonea, D.; Martínez-García, D.; Segura, A. Optical Absorption of Divalent Metal Tungstates: Correlation Between the Band-Gap Energy and the Cation Ionic Radius Europhys. Lett. 2008, 83, 37002.
53. Jeitschko, W.; Sleight, A.W. Synthesis, Properties and Crystal Structure of β-$SnWO_4$, Acta Cryst. 1972, B28, 3174-3178.

54. Dong, H.; Li, Z.; Ding, Z.X. Nanoplates of α-$SnWO_4$ and SnW_3O_9 Prepared via a Facile Hydrothermal Method and Their Gas-Sensing Property Sensors and Actuators B, 2009, 140, 623-628.
55. Zhu, G.Q.; Que, W.X.; Zhang, J.; Zhong, P. Photocatalytic Activity of $SnWO_4$ and SnW3O9 Nanostructures Prepared by a Surfactant-Assisted Hydrothermal Process Materials Science and Engineering B 2011, 176, 1448-1445.
56. Murahashi, S-I. Synthetic Aspects of Metal-Catalyzed Oxidations of Amines and Related Reactions Angew. Chem. Int. Ed. Engl. 1995, 34, 2443-2465.
57. Lang, X.; Ma, W.; Zhao, Y.; Chen, C.; Ji, H.; Zhao, J. Visibe-Light-Induced Selective Photocatalytic Aerobic Oxidation of Amines into Imines on TiO2 Chem. Eur. J. 2012, 18, 2624-2631.
58. Zhang, M.; Wang, Q.; Chen, C.; Zang, L.; Ma, W.; Zhao, J. Oxygen Atom Transfer in the Photocatalytic Oxidation of Alcohols by TiO2: Oxygen Isotope Studies Angew. Chem. Int. Ed. 2009, 48, 6081-6084.
59. Li, N.; Lang, X.; Ma, W.; Ji, H.; Chen, C.; Zhao, J. Selective Aerobic Oxidation of Amiens to Imines by TiO2 Photocatalysis in Water Chem. Commun. 2013, 49, 5034-5036.
60. Furukawa, S.; Ohno, Y.; Shishido, T.; Teramura, K.; Tanaka, T. Selective Amine Oxidation Using Nb2O5 Photocatalyst and O2 ACS Catal. 2011, 1, 1150-1153.
61. Hoover, J.M.; Stahl, S.S. Highly Practical Copper(I)/TEMPO Catalyst System for Chemoselective Aerobic Oxidation of Primary Alcohols J. Am. Chem. Soc. 2011 133, 16901-16910.
62. Hoover, J. M.; Ryland, B. L.; Stahl S. S.; Copper/TEMPO-Catalyzed Aerobic Alcohol Oxidation: Mechanistic Assessment of Different Catalyst Systems ACS Catal. 2013, 3, 2599-2605.

Chapter 2

Improving Charge Transfer at the $CuWO_4$-FTO Interface with Graphene Modification

2.1 Introduction

Suppression of recombination in semiconductor materials is an important property to control in photoelectrochemical applications.[1,2] The ability to obtain kinetic information, the identification of resistance to charge transfer at an interface, and the route of recombination of charges are important reasons to study charge transfer in electrochemical systems.[3] Aside from recombination at the semiconductor-solution interface another possible energy loss mechanism is recombination at the conductive substrate or Ohmic contact.[4] Fluorinated tin oxide (FTO) is the standard conductive substrate used for analysis of thin films in the field of photoelectrochemical water splitting because it is transparent over the entire solar spectrum and inexpensive. It is used as an Ohmic contact to semiconductor materials deposited onto it. Since all semiconductors likely suffer from recombination whether at the contact or on the surface, the focus becomes that of prevention. For this reason we have determined the use of graphene as an interlayer to improve charge transfer at the substrate-semiconductor interface to ultimately improve the ability to perform water oxidation on the surface.

Graphene possesses a high electron mobility (as high as 200,000 $cm^2/V^{-1}s^{-1}$ at

T=20K)[5] and high conductivity compared to the mobilities observed in metal oxides (10^{-3} – 10 $cm^2/V^{-1}s^{-1}$)[6] due to its sp^2-hybridized two-dimensional carbon network, resulting in an abundance of delocalized electrons. These characteristics, coupled with its high specific surface area (2630 m^2g^{-1}),[7] make it an advantageous material for improving charge transfer. Most composites have been formed by the use of graphene oxide and various graphite exfoliation techniques. The exploration of graphene in the field of photoelectrochemical water splitting has so far mainly focused on the synthesis of metal oxide/graphene powder composites. Specifically, WO_3@graphene composite powders have been synthesized for oxygen evolution by Guo et al producing 388 μmol L^{-1} for the WO_3@GR composite and 186 μmol L^{-1} for the WO_3 control.[8] Other powder composites of Bi_2WO_6/graphene and TiO_2/graphene have also been shown to more efficiently perform dye degradation than without the graphene support.[9,]

One example in the literature of metal oxide/graphene films consists of a general study using composites of TiO_2 (Degussa P25), WO_3, and $BiVO_4$ showing improved current when graphene was included.[10] A $BiVO_4$ film composite by Ng et al. shows more photocurrent is produced by a film that has been constructed from metal oxide/graphene composite powder than with the powder electrode alone.[11] In order to electrochemically characterize any enhancement made with graphene; these materials (with and without graphene) must be made into an electrode. The characteristics and engineering of photoelectrodes becomes increasingly important to minimize losses that will affect overall efficiency.

A direct comparison of our electrode system with and without the presence of graphene (GR), will allow assessment to whether or not electron ejection into FTO plays

a role in recombination. Electrochemical impedance spectroscopy (EIS) will be used to analyze the charge transfer characteristics at this substrate-semiconductor surface.

2.2 Results and Discussion

2.2.1 Graphene Deposition and Characterization on FTO

It is important to begin with a pristine GR monolayer to demonstrate that GR addition results in better electron transport and also to directly pinpoint the chemical and physics reasons for enhanced electron transfer. The quality of the GR sample may be easily affected by impurities, oxidation, and poor transfer among others. Therefore, characteristic properties were determined before metal oxide deposition. A fresh graphene modified FTO (FTO|GR) sample was characterized by XPS, and shows a single C 1s peak at 284.5 eV expected of a pure sample of graphene (Figure A.1). Raman spectroscopy was also used to characterize the GR films with measurements taken on 7 different locations across the film surface. There are two peaks representative of the sample in Figure A.2 that corresponds to the G band (1595 cm^{-1}) and 2D band (2691 cm^{-1}), respectively. The (I_{2D}/I_G) ratio is ~3.21 with exfoliated single layer graphene having a ratio of ~3.79 and expected to have a 2D intensity about four times greater than that of the G band, which we observe in our samples. The FWHM of the 2D peak is ~29 cm^{-1}, in which 30 cm^{-1} is said to be the cutoff for single layer GR.[12,13]

Furthermore, with the use of GR modification for water oxidation one important aspect that must be realized before moving toward metal oxide deposition is GR stability toward oxidation. Running a cyclic voltammogram of the FTO|GR sample in 0.1 M potassium phosphate buffer (KP_i) at pH 5 (Figure A.3) shows an irreversible oxidation that begins at ~0.99 V vs RHE. Characterization of the films after a bulk electrolysis in

the same conditions (Figure A.4) at 1.23 V *vs* RHE (thermodynamic potential for water oxidation) show detection of oxygen containing groups by XPS and a defect peak in the Raman (D band) which arises as a result of sp^3 character on the graphene plane (Figure A.5 and Figure A.6).[13] Therefore, we conduct our electrochemical experiments on pristine GR at electrical potentials less positive than 0.99 V to prevent electrochemical oxidation and appearance of this D band. With the exploration of GR stability in oxidizing environments our results provide a window in which electrochemistry can be performed without the added complications of graphene oxidation. Therefore we refer to the Raman spectrum in Figure A.2 and use a pristine GR sample for these experiments. Although, covering the GR surface with a metal oxide will enhance the stability of GR in aqueous conditions and allow us to scan the potential range past 0.99 V vs RHE.

Electrochemical impedance spectroscopy (EIS) was used to determine the charge-transfer resistance (R_{ct}) from a reversible redox couple at a bare FTO surface versus FTO|GR before any metal oxide deposition. The solution redox couple chosen was $Fe(CN)_6^{3-/4-}$, prepared from equimolar $K_3Fe(CN)_6$ and $K_4Fe(CN)_6$ (0.01 M) in 0.1 M KP_i (pH=5) and 0.1 M KCl in a three-electrode set-up with Pt-mesh as the auxiliary electrode. The potential was examined at 0.25 V (vs. an Ag/AgCl reference; 0.45 V vs SHE), where the $E_{1/2}$ of the $Fe(CN)_6^{3-/4-}$ reaction was determined by cyclic voltammetry (Figure A.7) and matches closely to that of what is reported ($[Fe(CN)_6]^{3-} + e^- \rightarrow [Fe(CN)_6]^{4-}$, $E° = 0.460$ V). Figure 2.1 is the Nyquist plot of data output identifying resistance due to $Fe(CN)_6^{3-/4-}$ electron transfer (R_{ct}) at each electrode surface. This data was fit to the equivalent circuit shown in Figure 2.1. The value of R_{ct} is represented by the diameter of the semicircle on the Z' axis. Z', the real component of the ac impedance represents

impedance due to resistance and the imaginary Z'' component represents impedance due to capacitance. The result supports our hypothesis; the FTO film (R_{ct} = 105 Ω) is five-fold more resistive than FTO|GR (R_{ct} = 20 Ω). The upward trend in the GR sample in the lower frequency region (higher Z' value) signifies impedance due to mass transport. The prominence of this feature called the Warburg impedance, *RW,* in FTO|GR also indicates faster electron transfer than in FTO alone. This data was corroborated by observing the slope in the corresponding linear sweep voltammogram (LSV) in the same aqueous conditions by plotting current density (j) *vs.* overpotential (η) (Figure A.8 and Figure A.9). The negative reciprocal of the slope where the curve passes through the origin represents R_{ct}, where $R_{ct} = -\eta/j$. As highlighted in Table S1, representing the 0.01 M $Fe(CN)_6^{3-/4-}$ solution, the numbers are in reasonable agreement.

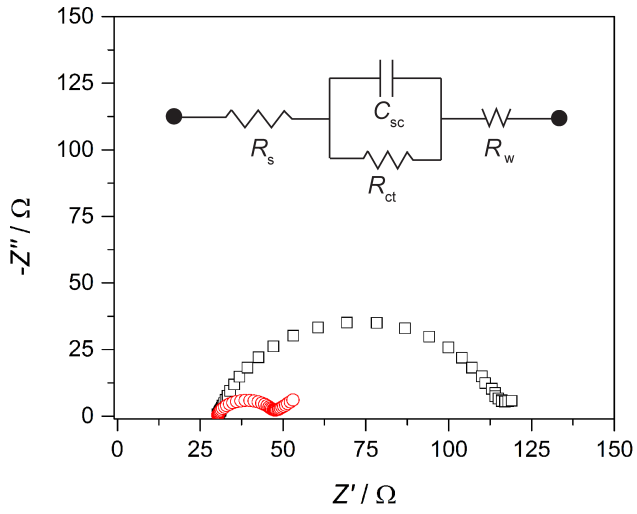

Figure 2.1 Nyquist ac impedance plots of FTO (black squares) vs. FTO|GR (red circles) in a 10 mM solution of $Fe(CN)_6^{3-/4-}$ 0.1 M KP_i.

This result indicates that GR modification will produce an electrode with lower resistance to charge transfer from $CuWO_4$ to FTO, and which should lead to enhanced

photocurrent for water oxidation. We have proven that the GR modified FTO is able to facilitate the oxidation of $[Fe(CN)_6]^{4-}$ much faster than the FTO alone. However, this is only a simple outer sphere electron transfer and mainly proves the validity of using GR as an Ohmic interlayer. With the deposition of a metal oxide on top of the GR layer, we are able to assess the ability of this GR interlayer to transfer electrons while an inner sphere electron transfer in the case of water oxidation or methanol oxidation is taking place at the $CuWO_4$ surface. Therefore, since $CuWO_4$ will interact similarly with the solution with and without the GR present an assessment of improvement due to the GR addition can be made.

2.2.2 $CuWO_4$ Deposition and Film Characterization

The graphene oxidation observed at higher potentials in aqueous solutions is one reason pulsed laser deposition (PLD) was employed to deposit $CuWO_4$. PLD is often used to obtain a crystalline material coating with high surface coverage.[14] Films of $CuWO_4$ were deposited onto FTO and FTO|GR electrodes by pulsed laser deposition (PLD) for a time of 20 minutes (deposition A) and 60 minutes (deposition B) from a crystalline target of $CuWO_4$ produced by solid state synthesis using CuO and WO_3. As the target was struck with a laser pulse, a plasma plume was formed and diffused to the substrate that was heated at 600 ºC. For deposition A the SEM reveals 500 × 100 nm ellipsoid-like shaped particles (Figure 2.2a). The deposition particles differ in size with the addition of GR to smaller ~50 nm particles and larger platelet-like particulates of 500 – 700 nm by length (Figure 2.2b). The deposition coverage does not look consistent and has exposed FTO remaining. For this reason we held the deposition temperature at 600 ºC, but increased the deposition time to 60 min. This method produced films with much

better coverage and consistent surface morphology on FTO and FTO|GR deposition (deposition B; Figure 2.2c,d). The morphology can be described by platelets that either sit parallel with the surface or are oriented perpendicular and protrude out of the surface of the film. The protruding platelet-like morphology is shown in the cross sectional SEM with a thickness of ~550 nm for the FTO|$CuWO_4$ film and ~650 nm for the FTO|GR|$CuWO_4$ film (Figure 2.3). Uniform coverage has been achieved using deposition B with minimal cracks and pores where the solution can come into direct contact with GR.

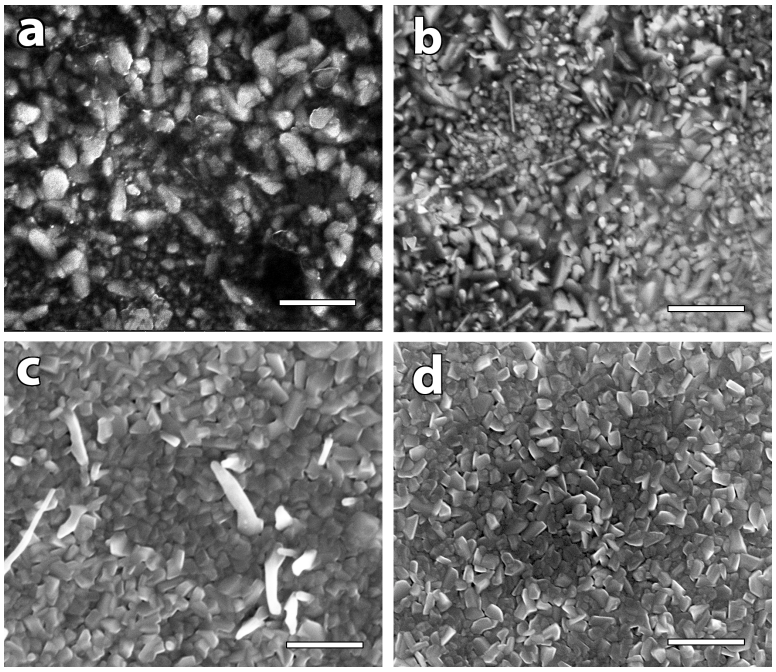

Figure 2.2 SEM images of (a) FTO|$CuWO_4$ prepared by 20 minute deposition at 600 °C; (b) FTO|GR|$CuWO_4$ prepared by 20 minute deposition at 600 °C; (c) FTO|$CuWO_4$ prepared by 60 minute deposition at 600 °C; and (d) FTO|GR|$CuWO_4$ prepared by 60 minute deposition at 600 °C. The scale bar in all images is 2 μm.

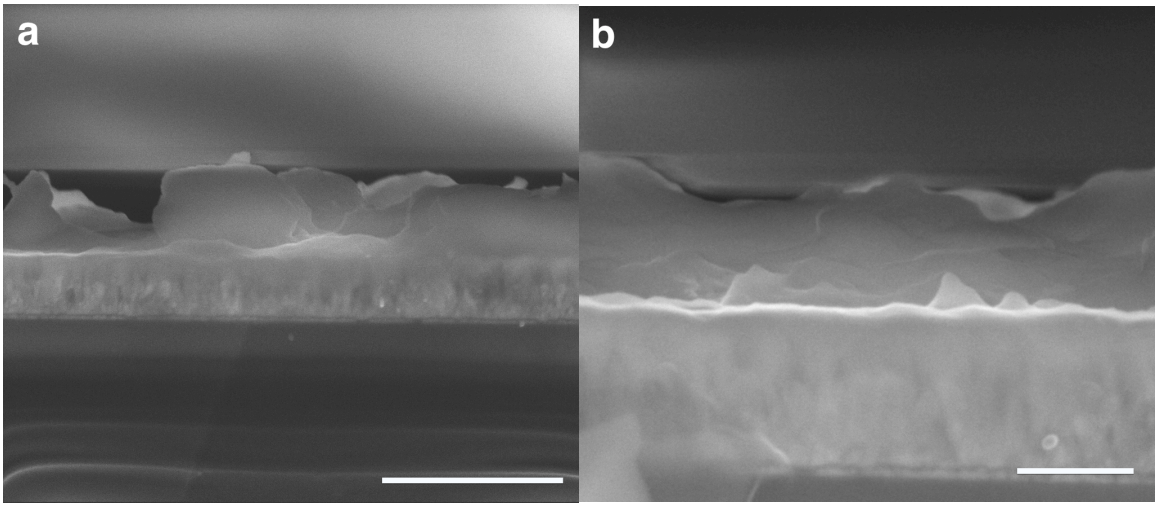

Figure 2.3 Cross Sectional SEM image of (a) FTO|$CuWO_4$ prepared by 60 minute deposition at 600 °C. The scale bar is 2 μm.; (b) FTO|GR|$CuWO_4$ prepared by 60 minute deposition at 600 °C. The scale bar is 500 nm.

Characterization by X-ray diffraction (XRD) (Figure 2.4) shows that crystalline $CuWO_4$ resulted from the deposition at 600 ºC onto FTO for both 20 and 60 minutes with a very small shoulder at 33.24º 2θ representing a slightly W-rich material. Energy dispersive X-ray analysis (EDAX) measurements also confirm this conclusion as we observe a W:Cu ratio of ~1.14 for both samples (XRD for both 20 and 60 minute deposition onto FTO|GR are plotted in Figure A.10 and are identical to those deposited onto FTO). We would expect this observation in both samples since the same target is being used for both depositions. Changing the deposition time also has an impact on the preferred orientation, specifically the (001) and (100) peaks, as is depicted in the change in intensity observed in the XRD of Figure 2.4. Since better coverage and consistent morphology of the films deposited for 60 minutes has been achieved, these films were used for the remainder of the experiments discussed.

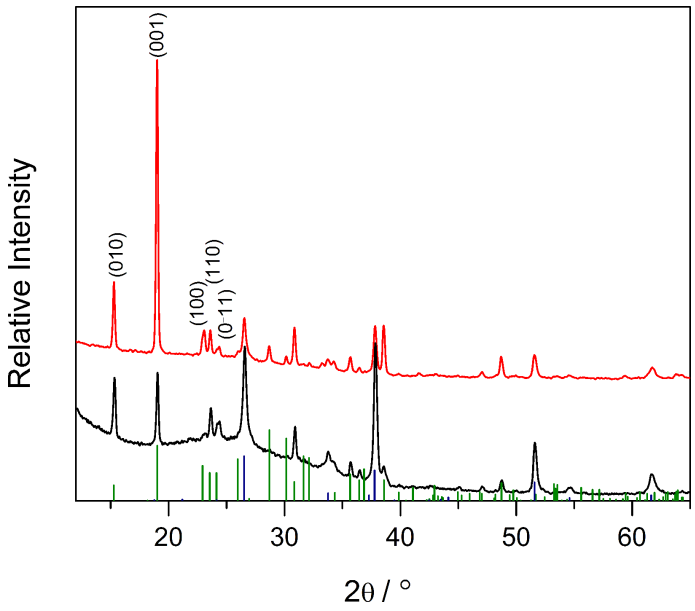

Figure 2.4 XRD patterns of FTO| $CuWO_4$ at 600 °C, 20 minute growth (black) and 60 minute growth (red). FTO peaks are represented by the navy vertical lines and $CuWO_4$ is represented by the green vertical lines.

The optical properties probed by UV-Vis spectroscopy show an indirect band gap of ~2.6 eV, as seen in the Tauc plot inset of Figure 2.5. A larger band gap (E_g) than is seen for previous reports of $CuWO_4$ (2.4 eV)[16] is due to poor ability to absorb light because the $CuWO_4$ layer is only 200 nm. An indirect material is known to benefit from a thicker absorber layer due to the necessity of a phonon as well as a photon for excitation.[15] The PLD method was not necessarily optimized to yield the highest absorbing thick films.

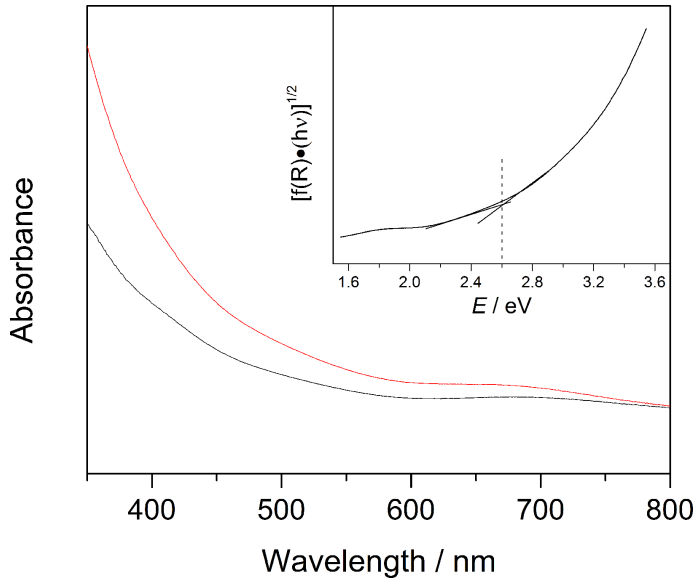

Figure 2.5 Absorption spectra of FTO|$CuWO_4$ (black) and FTO|GR|$CuWO_4$ (red) with Tauc plot inset both films showing a 2.6 eV E_g.

2.2.3 Photoelectrochemistry: Linear Sweep Voltammetry, Electrochemical Impedance Spectroscopy, and MeOH oxidation

The photoelectrochemical analysis after metal oxide deposition correlates to the results we observe for improved electron transfer when just comparing FTO to FTO|GR in the $[Fe(CN)_6]^{3-/4-}$ solution. The films were deposited by PLD due to the advantages of deposition in vacuum and production of crystalline $CuWO_4$ with uniform film coverage. Since no additional annealing or conditioning step was needed, the comparison between the two films stayed consistent with no change to the GR layer. Moving further from a simple 1-electron redox couple, the electrodes were tested in conditions suited for multi electron water oxidation. The LSV with chopped light in Figure 2.6 shows the comparison between the $CuWO_4$ film deposited onto the FTO (FTO|$CuWO_4$) and the $CuWO_4$ deposited onto the GR modified electrode (FTO|GR|$CuWO_4$) in a 0.1 M KP_i pH 5 solution under standard 1-sun illumination (100 mW/cm^2). There is a current doubling effect observed in the film with GR modification showing greater ability to perform the

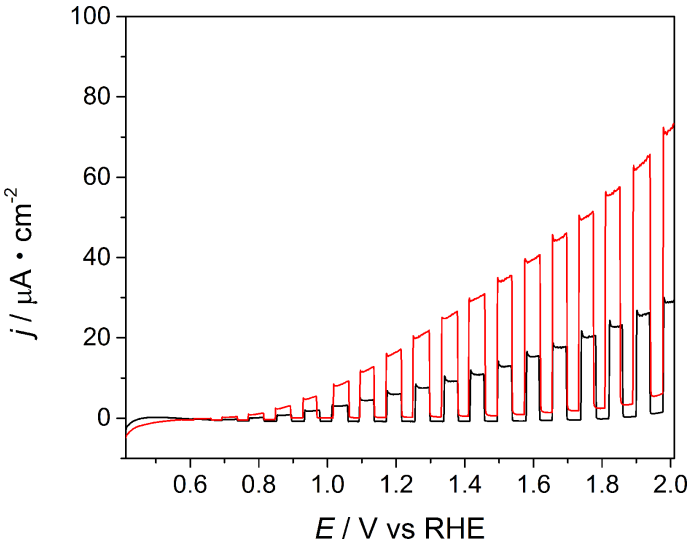

Figure 2.6 Chopped light linear sweep voltammogram of the FTO| $CuWO_4$ electrode (black) and FTO|GR| $CuWO_4$ (red) in 0.1 M KP_i, pH 5 at 100 mW/cm^2.

water oxidation reaction. To validate the ability to perform this reaction more efficiently with GR present, we performed EIS on these films to monitor the resistance to water oxidation at the surface. Under 1-sun in 0.1 M KP_i at pH 5, there is less resistance to water oxidation again with the GR modified sample as shown in the Nyquist plot in Figure 2.7. The charge transfer resistance, R_{ct}, at 0.89 V for FTO|$CuWO_4$ is 75,276 Ω and the R_{ct} for FTO|GR|$CuWO_4$ = 14,686 Ω shows that the resistance to water oxidation is dramatically decreased for the FTO|GR|$CuWO_4$ electrode. The R_{ct} values for the potential ranges scanned are shown in Table 2.1. Looking at the comparison of R_{ct} across potential ranges with the FTO|$CuWO_4$ vs FTO|GR|$CuWO_4$ gives insight into rate-limiting processes since we know that EIS only determines the resistance from the rate-limiting step. As the potential is increased from 0.89 – 1.29 V vs. RHE with the FTO|$CuWO_4$ electrode, R_{ct} steadily decreases. However, with the FTO|GR|$CuWO_4$ electrode, R_{ct} stays fairly consistent throughout that potential range, implying that the addition of GR is suppressing a resistive component that directly impacts the rate-limiting process being

measured by EIS.

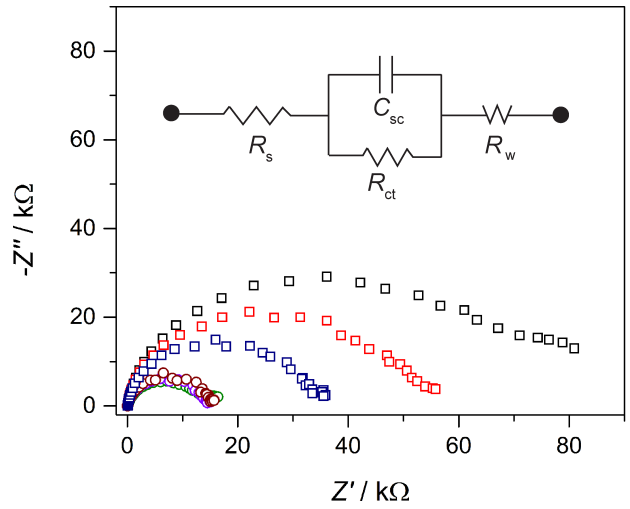

Figure 2.7 Nyquist plot of the resistance to water oxidation on FTO| $CuWO_4$ and FTO|GR| $CuWO_4$ under AM1.5 G, 1-sun illumination (100 mW/cm^2) in 0.1 M KP_i, pH 5 solution. The inset shows the equivalent circuit to which the data was fit.

Table 2.1 Comparison of R_{ct} values for FTO|$CuWO_4$ vs FTO|GR|$CuWO_4$ at 100 mW/cm^2 in the potential range of 0.89 – 1.29 V vs RHE.

Potential (V)	**R_{ct} FTO|$CuWO_4$ (Ω)**	**R_{ct} FTO|GR|$CuWO_4$ (Ω)**
0.89	75,276	14,686
1.09	51,508	14,493
1.29	34,039	14,430

The same comparison using EIS was performed at 5-sun illumination (500 mW/cm^2) (LSV, Figure A.11) in 0.1 M KP_i (pH=5). With a higher number of charge carriers generated by the increase in photon flux, we are able to determine if a plateau had been reached in R_{ct} values at 100 mW/cm^2 with the introduction of the graphene

layer. However, not only do we continue to see a decrease in R_{ct} for the FTO|GR|$CuWO_4$ electrode, but the FTO|GR|$CuWO_4$ film has a higher R_{ct} value at 0.89 V than at 1.09 V and 1.29 V where it seems to plateau again to the same resistive value (7,198 Ω and 7,134 Ω). A lower R_{ct} was also still observed with the FTO|GR|$CuWO_4$ film than FTO|$CuWO_4$ (10,947 Ω *vs* FTO|$CuWO_4$ = 22,576 Ω Figure A.12), although the gap in the difference of R_{ct} has decreased due to higher influx of charges created by the increased power applied (500 mW/cm^2 vs. 100 mW/cm^2). R_{ct} in the FTO|$CuWO_4$ electrode steadily decreases again with each potential at this higher photon flux, just as we saw at 100 mW/cm^2 where no plateau is seen at these potentials. Since R_{ct} for the FTO|GR|$CuWO_4$ film converges to the same value at much lower potentials than that of FTO|$CuWO_4$ (whether at 100 or 500 mW/cm^2), it is evident that the addition of GR helps to reduce the overall resistance of the rate-limiting process being measured (water oxidation at the electrode surface) since an increase in photocurrent is observed.

As stated previously, FTO is used as an Ohmic contact, in which an Ohmic contact is defined as one in which there is an unimpeded transfer of majority carriers from one material to another, i.e., the contacts do not limit the current.[16] The way to achieve such a contact is by doping the semiconductor heavily enough that tunneling is possible (tin oxide heavily doped with fluorine). Ohmic contact between the semiconductor and conductive substrate requires equilibration of the Fermi level, and poor equilibration results in Fermi level pinning, thus generating a Schottky barrier at the substrate-semiconductor junction.[17] Therefore, it is possible that FTO does not create an Ohmic contact but instead creates a Schottky barrier at the FTO-semiconductor interface. Potential contributions include the roughness and lattice mismatch of FTO to deposited

semiconductor materials. The structure of FTO is a tetragonal rutile structure, with a =4.74 Å and b = 3.19 Å, and is much different from that of $CuWO_4$, which has a triclinic cuproscheelite structure with a = 4.72, b = 5.82, and c = 4.87. The surface roughness of FTO is also likely a contributing factor with an RMS (root mean square) value of ~11 nm with an average lowest valley to highest peak difference of 144 nm across 5 sample spots. With this large difference in lattice spacing as well as a high surface roughness for FTO, it is feasible that sufficient contact is not formed. This lattice mismatch could contribute to poor contact at this interface. To help ensure contact in Fe_2O_3 deposited onto FTO, high annealing temperatures were employed by Wang et al. causing Sn diffusion into Fe_2O_3, which produced a thin layer of alloyed FTO/Fe_2O_3, or Sn-doped Fe_2O_3 predicted to lower the electron transfer resistance from Fe_2O_3 into FTO.[18]

The introduction of GR between the substrate-semiconductor junction is hypothesized to act as a low-barrier site for electron transfer from an n-type semiconductor. Specifically in our case, low-resistance charge transfer from $CuWO_4$ to GR as electrons reach the metal oxide-GR interface. GR not only has high conductivity and mobility, but could result in a contact with more Ohmic character to better facilitate charge transfer and in turn reduce the resistance to perform water oxidation at the surface. Interaction between $CuWO_4$ and GR enhances the separation of photogenerated electrons in this polycrystalline metal oxide from holes, allowing more holes to be used at the surface for oxidation. GR (instead of FTO) will now be the first electronic contact for electrons from $CuWO_4$ and due to its semi-metal characteristic band structure, it possesses high electron affinity and high electron mobility because of its sp^2 framework. It also is said to have a strong van-der-Waals attraction[19] as well as the ability to conform

to the substrate it is in contact with,[20] which is advantageous in addressing lattice mismatch as well as the substrate surface roughness of FTO. We surmise that these properties of GR do enhance the electron transfer from $CuWO_4$ to FTO and increased the photocurrent generation of our electrodes.

To prove that the increase in photocurrent is due to the introduction of GR, we have employed methanol oxidation for long term bulk electrolysis at 0.89 V in an aqueous solution of 10% methanol in 0.1 Na_2SO_4, 0.1 M KP_i, pH 5 (Figure 2.8). Higher steady state photocurrent is observed with the FTO|GR|$CuWO_4$ electrode at 21 μA vs. the FTO|$CuWO_4$ electrode with 6 μA and no degradation is observed for either electrode over 12 hours of illumination.

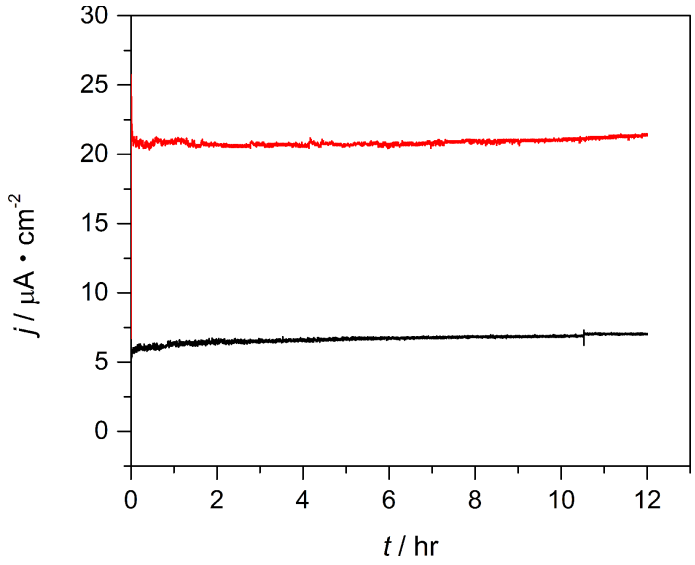

Figure 2.8 Bulk electrolysis of FTO| $CuWO_4$ (black) and FTO|GR| $CuWO_4$ (red) in a 10% MeOH, 0.1 M Na2SO4, 0.1M KP_i solution at 0.894 V vs RHE.

The focus of this experiment is not on the reaction taking place on the surface of $CuWO_4$, but rather to show the stability of the electron transfer associated with $CuWO_4$ to GR to FTO junction and that the increased photocurrent produced with the addition of

GR is continuous and does not drop after an initial period of time. This experimental evidence illustrates the point that GR is contributing to better charge transfer at the substrate-semiconductor interface and is the reason for increased photocurrent. Along with the impedance results, this result solidifies the importance of the addition of the GR layer for a lower barrier to charge transfer and the ultimate effect it has on the overall surface reaction taking place.

2.3 Conclusion

Using the tool of electrochemical impedance spectroscopy, we have measured the electrochemical resistance to perform the water oxidation reaction in order to probe if a difference in R_{ct} rate-limited processes is observed. In the impedance spectrum we observe lower R_{ct} of 14,686 Ω in our film modified with GR to perform water oxidation at low potentials (0.89 V vs RHE) versus that of the unmodified film (75,276 Ω). These resistance values relate directly to the photocurrent doubling effect that is seen in the *j-E* profile showing the improvement of the modified electrode. Furthermore, this result solidifies the importance of the addition of the GR layer for more effective charge transfer. These results also opens the door for GR as a replacement to FTO or other transparent conducting oxides (TCOs) in applications such as tandem devices that use thin layers of FTO or ITO (indium tin oxide) since single layer GR absorbs only ~2% of visible and infrared light passing through it. ITO is more often employed in PV devices because it possesses a smaller resistance even as it approaches thin layers as small as 100 nm. However, using graphene could reduce unwanted light absorption of this intermediate layer and give rise to better electron transfer due to contour ability, mobility, and van der Waals attraction.

2.4 Experimental Selection

2.4.1 Synthesis and Electrode Fabrication

All chemicals were purchased from Aldrich without any further purification. FTO was purchased from Pilkington Glass (Tec 15 2.2 mm thick, 12–14 Ω/sq) and was cleaned by sonication in ethanol, acetone and de-ionized water for 15 min each and dried under N_2.The GR films were deposited by chemical vapor deposition and were provided by Zhong et al. The graphene is grown on a 2 cm^2 piece of copper foil in a tube furnace by mixture of CH_4 and H_2. A poly(methyl methacrylate) (PMMA) protective layer is used to protect the GR layer until use. In order to transfer the GR sample, the copper is etched away in an aqueous iron solution, and the GR layer is lifted up onto the FTO substrate to dry for 24 hours. The PMMA was removed by soaking the film in acetone and isopropanol for 15 minutes each.

$CuWO_4$ was deposited by pulsed laser deposition (PLD) onto FTO and onto FTO|GR. The laser power density was 200 mJ/mm^2 with a pulse frequency of 8 Hz. The substrate temperature was held at 600 °C for 20 minutes or 60 minutes during the deposition with an O_2 partial pressure of 100 mTorr. A vacuum atmosphere with a low partial pressure of O_2 was used during the deposition. We did not perform the heating with FTO|GR films only and no PLD deposition. Without PLD of CuO and WO_3 there is a higher chance GR may be oxidized. Even so there is a possibility for GR oxidation during the PLD process of CuO and WO_3, but due to the increase in photocurrent we observe we do not expect problematic GR oxidation has taken place.

2.4.2 Structural Characterization

X-ray diffraction patterns were recorded on a Bruker D8 Advance diffractometer

equipped with a graphite monochromator, a Lynx- Eye detector, and parallel beam optics using Cu Ka radiation (l 1⁄4 1.54184 Å). Patterns were collected using a 0.6 mm incidence slit, with a step size and scan rate of 0.04°/step and 0.5 s/step respectively. Phases were identified as $CuWO_4$ (JCPDF 72-0616) using MDI Jade version 5.0. Observed $CuWO_4$ Bragg reflections were compared to those calculated from the single crystal X-ray structure. Atomic Force Micrograms were recorded on a Veeco Dimension Icon Atomic Force Microscope using tapping mode. Root mean square and peak-to-peak depth measurements were obtained using SPIP (Scanning Probe Imaging Software). UV-Vis spectra were recorded using an Agilent-Cary 5000 spectrophotometer equipped with an external diffuse reflectance accessory. Spectra were recorded in transmission mode and transformed mathematically into normalized absorbance. Tauc plots were then generated using the Kubelka–Munk function, $F(R) = (1 - R)^2/2R$. Raman spectra were recorded using a Renishaw inVia Raman microscope at 514 nm excitation. Scanning electron microscope images, top down and cross sectional, were obtained using an FEI Nova Nanolab SEM/FIB with an accelerating voltage of 15 kV. X-ray photoelectron spectra were recorded on a Kratos XPS (8 mA, 14 keV, Monochromatic Al). All peaks were calibrated to C(1s) at 284.5 eV. The XPS data was fit using CasaXPS. C(1s) peaks were fit with a Shirley background using a A(0.3,0.38,30)GL(20) fit due to the asymmetry of the peak (Doniach-Sunjic line shape) consistent with highly conductive carbon materials commonly seen with the C(1s) in the literature.[21,22,23] Secondary peaks or peaks due to oxidation representing C-O bonds were fit using a Gaussian/Lorentzian mixing ratio.

Energy dispersive X-ray analysis spectra (EDX) were collected using a Nova

Nanolab SEM/FIB with an accelerating voltage of 20 kV and a working distance of 5 mm. Spectra were quantified using EDAX genesis software and the Cu K and W L emission lines were used. Spectra were collected for 100 live seconds with a dead time (% DT) less than 40% collecting on average 2400 cps.

2.4.3 Photoelectrochemistry and Electrochemical Impedance Spectroscopy

Photoelectrochemical measurements were performed in custom-built Pyrex glass cells with a quartz viewing window. Voltammetry was performed in a single compartment cell and controlled potential coulometry was carried out in a two compartment cell separating the working and counter electrodes. At a given time the cell contained the working thin-film photoanode, Ag/AgCl reference electrode in saturated KCl, and a platinum auxiliary. For water oxidation, the supporting electrolyte used was a 0.1 M potassium phosphate buffer (KP_i) at pH 5. Oxidation of methanol was carried out in a 10% methanol/ 0.1 M KP_i, 0.1 M Na_2SO_4 pH 5 solution. Electrical contact was made to FTO on the working electrode by attaching copper wire purchased from Fisher Scientific and using CG Electronics Silver Print II. Electrodes were sealed using epoxy by JB Weld and tested to determine the epoxy was inert toward reactivity. Voltammetry was performed with a CH Instruments 660C Electrochemical Workstation. The light source was a Newport-Oriel 150 W Xe arc lamp fitted with a Newport AM 1.5G filter to simulate incident solar radiation. For certain experiments the lamp power was adjusted to 100 mW/cm^2 and 500 mW/cm^2 using a Newport 1918-R optical power meter equipped with a Newport 818P-015-19 thermopile detector. A 1 cm^2 area was irradiated through the quartz window in all cases.

Electrochemical impedance spectroscopy analysis was carried out with an Eco Chemie Autolab PGSTAT302N potentiostat with a frequency-response analysis (FRA) module. Measurements were taken from 0.4 – 0.8 V vs Ag/AgCl (0.89 – 1.29 vs RHE) in 200 mV increments with a 5-minute equilibration time at each potential. For clarity all potentials (E, V) mentioned in this manuscript are reported against the reversible hydrogen electrode, RHE, which is related to the Ag/AgCl reference electrode and pH according to the Nernst equation: $E_{RHE} = E_{Ag/AgCl} + 0.199\ V + 0.0591\ V \bullet pH$. A range of frequencies between 65,000 and 0.01 Hz was used with a 10 mV amplitude perturbation. Data were fit using Zview software. The supporting electrolyte used was a 0.1 M potassium phosphate buffer (KP_i) at pH 5. The light source was a Newport-Oriel 150 W Xe arc lamp fitted with an AM 1.5G filter to simulate incident solar radiation at 100 mW/cm^2 and 500 mW/cm^2.

2.5 References

1. J. A. Turner, A Realizable Renewable Energy Future Science 1999, 285, 1493.
2. Bolton, J. R.; Strickler, S. J.; Connolly, J. S.; Limiting and Realizable Efficiencies of Solar Photolysis of Water Nature 1985, 316, 495.
3. A.J. Bard, L. R. Faulkner Electrochemical Methods: Fundamentals and Applications January 2002.
4. Konin, A. Interface Recombination Feature in Metal-Semiconductor Junction at High Photoexcitation Semicond. Sci. Technol. 2014, 29, 095009.
5. Du, X.; Skachko, I.; Barker, A.; Andrei, E. Y. Approaching Ballistic Transport in Suspended Graphene Nature Nanotechnology 2008, 3, 491-495.
6. Zhong, D. K.; Sun, J.; Inumaru, H.; Gamelin, D.R. Solar Water Oxidation by Composite Catalyst/α- Fe_2O_3 Photoanodes J. Am. Chem. Soc. 2009, 131, 6086-6087.
7. Rao, C.N.R.; Sood, A.K.; Subrahmanyam, K.S.; Govindaraj, A. Graphene: The Two-Dimensional Nanomaterial Angew. CHem. Int. Ed. 2009, 48, 7752.
8. Guo, J.; Li, T.; Zhu, S.; Chen, Z.; Liu, Q.; Zhang, D.; Moon, W-J.; Song, D-M. Synthesis of WO3@Graphene Composite for Enhanced Photocatalytic Oxygen Evolution from Water RSC Adv. 2012, 2, 1356-1363.
9. Min, Y.-L.; Zhang, K.; Chen, Y.-C.; Zhang, Y.-G. Enhanced Photocatalytic Performance of Bi2WO6 by Graphene Supporter as Charge Transfer Channel Separation and Purification Technology 2012, 86 ,98-105.

10. Y.H. Ng, A. Iwase, N.J. Bell, A. Kudo, R. Amal, Semiconductor/reduced Graphene Oxide Nanocomposites Derived from Photocatalytic Reactions, Catalysis Today, 2011, 164, 353-357.
11. Ng, Y.H.; Iwase, A; Kudo, A.; Amal, R. Reducing Graphene Oxide on a Visible-Light $BiVO_4$ Photocatalyst for an Enhanced Photoelectrochemical Water Splitting J. Phys. Chem. Lett. 2010, 1, 2607-2612.
12. Lee, S.; Lee, K.; Zhong, Z. Wafer Scale Homogeneous Bilayer Graphene Films by Chemical Vapor Deposition Nano Lett. 2010, 10, 4702-4707.
13. Graf, D.; Molitor, F.; Ensslin, K.; Stampfer, C.; Jungen, A; Hierold, C; Wirtz, L. Spatially Resolved Raman Spectroscopy of Single- and Few-Layer Graphene Nano Lett. 2007, 2, 238-242.
14. Morintale, E.; Constantinescu, C.; Dinescu, M. Thin Films Development by Pulsed Laser-Assisted Deposition Physics AUC 2010, 20, 43-56.
15. Gobeli, G.W.; Allen, F.G. Direct and Indirect Excitation Processes in Photoelectric Emission from Silicon Phys. Rev. 1962, 127, 141-149.
16. Kröger, F.A.; Diemer, G.; Klasens, H.A. Nature of an Ohmic Metal-Semiconductor Contact Phys. Rev. 1956, 103, 279.
17. Brillson, L.J.; Lu, Y. ZnO Schottky Barriers and Ohmic Contacts J. Appl. Phys. 2011, 109, 121301.
18. Wang, L.; Lee, C-Y.; Schmuki, P. Influence of Annealing Temperature on Photelectrochemical Water Splitting of α- Fe_2O_3 Films Prepred by Anodic Deposition Electrochimica Acta 2013, 91, 307-313.
19. Tongay, S.; Lemaitre, M.; Miao, XB. Gila, B.; Appleton, B.R.; Hebard, A.F. Rectification at Graphene-Semiconductor Interfaces: Zero-Gap Semiconductor-Based Diodes Phys. Rev. 2012, 2, 011002.
20. Cullen, W.G.; Yamamoto, M.; Burson, K.M.; Chen, J.H.; Jang, C.; Li, L.; Fuhrer, M.S.; Williams, E.D. High-Fidelity Conformation of Graphene to SiO2 Topographic Features Phys. Rev. Lett. 2010, 105, 215504.
21. Yang, D-Q.; Sacher, E. Carbon 1s X-ray Photoemission Line Shape Analysis of Highly Oriented Graphite: The Influence of Structural Damage on Peak Asymmetry, Langmuir, 2006, 22, 860-862.
22. Leiro, J.A.; Heinonen, M.H.; Laiho, T.; Batirev, I.G. Core-Level XPS Spectra of Fullerene, Highly Oriented Pyrolitic Graphite, and Glassy Carbon, Journal of Electron Spectroscopy and Related Phenomena 2003, 128, 205-213.
23. Estrade-Szwarckopf, H. XPS Photoemission in Carbonaceous Materials: A “Defect” Peak Beside the Graphite Asymmetric Peak Carbon 2004, 42, 1713-1712.

Chapter 3

Reactivity of $CuWO_4$ in Photoelectrochemical Water Oxidation by EIS

Portions of this chapter have been published:
Reproduced with permission from Yourey, J. E.; Pyper, K.J.; Kurtz, J.B.; Bartlett, B.M. *J. Phys. Chem. C* **2013**, *117*, 8708-8718. Copyright 2013 American Chemical Society http://pubs.acs.org/doi/abs/10.1021/jp402048b

Reproduced with permission from Pyper, K.J.; Yourey, J. E.; Bartlett, B.M. *J. Phys. Chem. C* **2013**, *117*, 24726-24732. Copyright 2013 American Chemical Society http://pubs.acs.org/doi/abs/10.1021/jp408434v

3.1 Introduction

As rising energy demands deplete fossil fuel reserves, a new sustainable approach for producing alternative fuels is necessary.[1] One approach uses abundant, affordable, robust metal oxide materials as catalysts to split water with energy from the sun.[2] With visible light irradiation, semiconducting metal oxides can photochemically split water into oxygen and hydrogen storing chemical energy.[3] However, significant focus has been placed on the water oxidation half reaction (1.23 V *vs* NHE) due to the slow kinetics associated with the 4-proton-4-electron coupled process. $CuWO_4$ is an *n*-type material and due to its ability to absorb visible light with a band gap, E_g, of 2.4 eV and appropriate valence and conduction band edges (+2.8 V and +0.4 V *vs* RHE respectively) has been identified as a photoanode for water oxidation.[4] $CuWO_4$ has been shown to generate

oxygen from water with 100% and 96% Faradaic efficiency in potassium phosphate and potassium borate buffers respectively, and is highly stable in potassium borate buffer at pH 7 (93% of the initial photocurrent is retained after 12 h of continuous illumination at 1.23 V *vs* RHE).[5] The d^9 configuration of Cu^{2+} in this ternary phase distinguishes it from the typical d^0 materials such as WO_3, TiO_2, and $BiVO_4$. It is also an indirect band-gap material, which requires a thick layer for maximum visible light absorption (α = 6600 cm^{-1} at 400 nm). Fabricating thicker electrodes by sol-gel processing or by electrodeposition has so far resulted in low external quantum efficiency.[16] In $CuWO_4$ specifically, localized Cu(3d) orbitals may contribute to low carrier mobilities in the bulk as well as recombination at the surface. Electrochemical impedance spectroscopy performed under illumination reveals charge-transfer events and suggests areas for improvement. The slow transfer of holes from the electrode surface to water as well as fast charge-carrier recombination rates contribute to the poor overall efficiency for photoelectrochemical water oxidation on metal oxides.[6–8] In addition, many semiconductors have mid-gap states that hinder the rate of water oxidation at the surface.[9–11]

For example, low carrier mobilities due to antiferromagnetically ordered 3d orbital spins, as well as surface electronic states are observed in hematite (α-Fe_2O_3) and contribute to poor performance.[12–14] Doping and morphology control address the limitations of poor electron mobility in α-Fe_2O_3 (10^{-2} $cm^2/V{\cdot}s$)[15–19], and chemical co-catalysts passivate detrimental surface states to prevent recombination.[20–22] Quantifying the specific charge-storage and charge-transfer properties at the surface and subsequent methods to alter composition and morphology have resulted in a dramatic improvement

in the photocurrent density attainable in hematite from tens of $\mu A/cm^2$ in 1994 to ~3.4 mA/cm^2 in 2011 (at 1.23 V RHE and 1-sun illumination conditions).[23]

Unlike the case of α-Fe_2O_3, many of the charge-storage and charge-transfer characteristics at the $CuWO_4$-water interface have not been identified. Therefore, we have conducted a series of electrochemical impedance experiments to measure capacitive and resistive elements at the surface/solution interface during water oxidation in neutral pH. Electrochemical impedance spectroscopy (EIS) is a technique that deconvolutes the current-voltage characteristics observed in a DC linear sweep voltammogram (LSV) under illumination to individual processes occurring at the surface by applying a small AC perturbation. EIS methods are employed to identify the distribution of electronic states in a semiconductor material, and can be used to identify mid-gap states.[24,25] In an ideal semiconductor, there are no states between the valence and conduction bands. However, in real materials, mid-gap electronic states commonly arise due to surface termination of the crystal lattice, defects at the surface, large differences between the bulk crystal and surface composition, or even donor species adsorbed to the surface.[26] The contribution of additional charged species affects the distribution of electrical potential at the surface, which can lead to Fermi level pinning.[27] Fermi level pinning due to mid-gap states inhibits band equilibration with the applied electrical potential.

We speculate that Cu-based mid-gap states arising from the $3d^9$ subshell play a predominant role in both electron transport throughout the bulk as well as surface mediated events in $CuWO_4$. Herein, EIS measurements were employed as a function of applied potential and light intensity. We identify capacitive and resistive elements responsible for the mechanism of water oxidation on $CuWO_4$, and discuss reasons for

which $CuWO_4$ does not produce the quantum efficiencies predicted by its band gap. The EIS and voltammetry experiments at pH 7.00 and pH 9.24 (pK_a of potassium borate) were also performed to evaluate the pH dependence of the surface band structure. The EIS data show that two separate charge-transfer processes occur during photoelectrochemical water oxidation. A pH-dependent pinning of the Fermi level has also been identified by Mott-Schottky analysis in the dark and under illumination. Our results suggest that $CuWO_4$ does not simply oxidize water through the valence band; rather, the chemistry is dictated by a mid-gap state.

3.2 Photoelectrochemistry and Electrochemical Impedance Spectroscopy

We performed linear sweep voltammetry and potentiometric electrochemical impedance spectroscopy both in the dark and under simulated solar irradiation to probe the electronic structure of $CuWO_4$. A limitation of EIS measurements is that there is no unique electrical circuit to fit the data. However, the equivalent circuit elements selected should correspond to a physical charge-storage or charge-transfer process occurring in the experimental system.[28] Figure 3.1a illustrates one plausible description of the electronic structure of $CuWO_4$ under illumination. In this figure, we show excitation in the bulk near the depletion region and possible subsequent processes for charge transfer. A mid-gap state is displayed between the valence band (VB) and conduction band (CB). Holes from the VB can either directly oxidize water or become trapped in the mid-gap state with subsequent transfer into solution. The photogenerated electrons in the CB can migrate to the back contact, recombine with VB holes, or transfer to the mid-gap state or any surface intermediates formed during the water oxidation reaction. To model all of these pathways requires an overparameterized equivalent circuit. Therefore, we use a

simplified circuit that includes only the rate-limiting (and thus measureable) events. This simplified circuit (Figure 3.1b) describes water oxidation on $CuWO_4$ that proceeds primarily through a mid-gap state as opposed to the valence band. This equivalent circuit accurately models our data, and the EIS results agree well with recent theory in which photoelectrochemical water splitting on a semiconductor film electrode proceeds through a mid-gap state.[29]

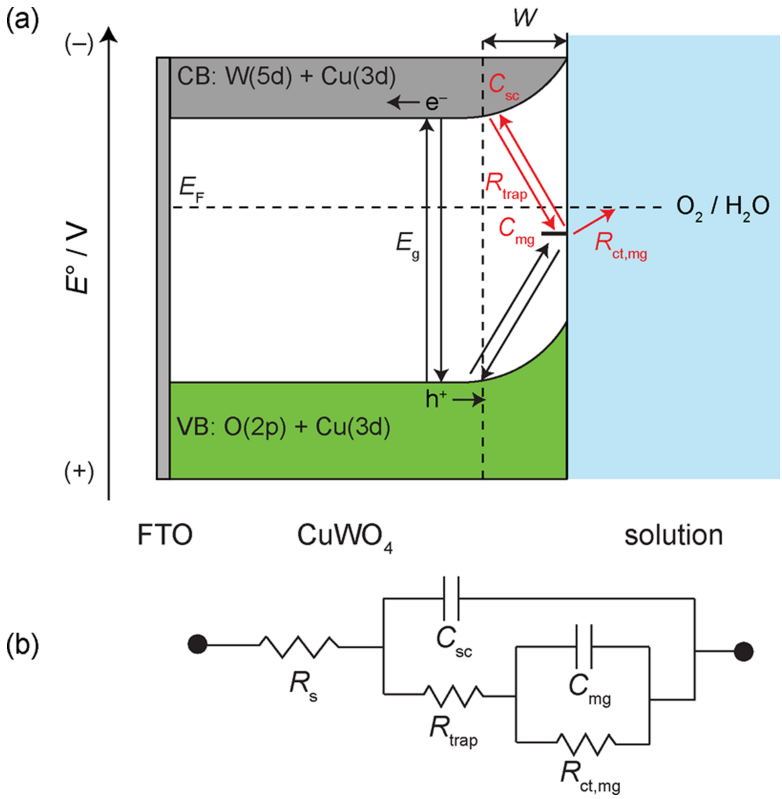

Figure 3.1 a) Proposed physical model for charge-carrier pathways in $CuWO_4$: *W* represents the depletion width, and the red arrows correspond to the charge-transfer processes measured by EIS. b) Equivalent circuit model of water oxidation through a mid-gap state.

Figure 3.2 shows the linear sweep voltammogram (LSV) of $CuWO_4$ in a pH 7.00 borate buffer at varying light intensity. For clarity, as we compare across pH values, all potentials (*E*, V) mentioned in this manuscript are reported against the reversible hydrogen electrode, RHE, which is related to the Ag/AgCl reference electrode and pH

according to the Nernst equation: $E_{RHE} = E_{Ag/AgCl} + 0.199\ V + 0.0591\ V \bullet pH$. The onset of photocurrent takes place at 0.80 V for 100 and 50 mW/cm^2 and 0.90 V for 15 mW/cm^2. Photoelectrochemical voltammetry is interpreted not only by the photocurrent density (j, mA/cm^2) produced, but also by the shape of the j–E curve observed. A system with high quantum efficiency will produce an exponential onset of current at the CB edge. However, the photocurrent onset for $CuWO_4$ obtained from the tangent line of the photocurrent (j_{ph}), is linear, and is ~400 mV more positive than the CB edge for 1-sun illumination (Figure B.1). This observation is typical for slow reactions such as water oxidation that proceed through mid-gap states or high-energy intermediates on poorly catalytic semiconductor surfaces such as Fe_2O_3 and $BiVO_4$.[30,31]

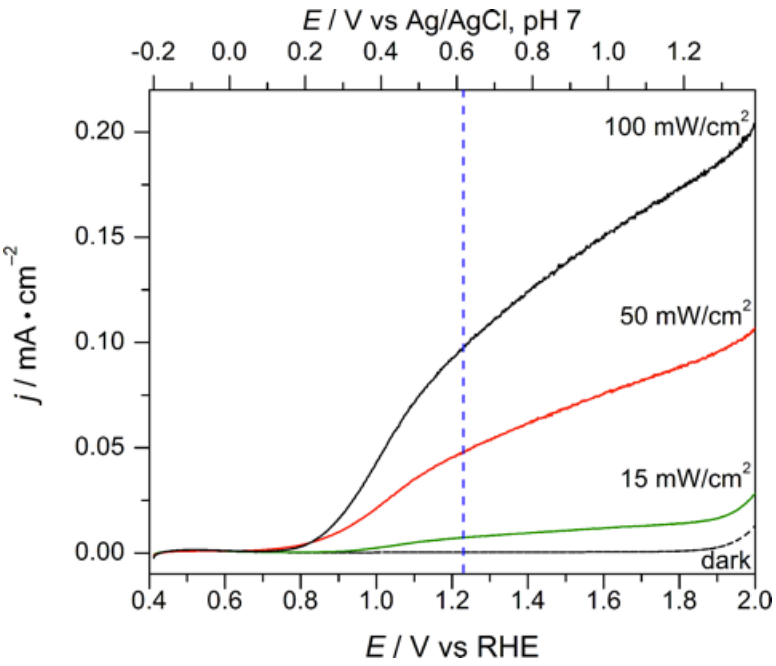

Figure 3.2 Linear sweep voltammogram as a function of light intensity and in the dark (dashed) for $CuWO_4$ thin films in 0.5 M KB_i, 0.2 M KCl buffer at pH 7.00 and AM1.5G irradiation at 100 (black), 50 (red) and 15 (green) mW/cm^2. The vertical blue dashed line represents the standard thermodynamic potential for water oxidation, 1.23 V *vs* RHE.

The processes taking place from 0.81 – 1.01 V were directly measured by EIS analysis to gain more insight into reasons for the large overpotential and slow onset of

photocurrent. It is beneficial to probe the electronics of $CuWO_4$ by measuring the overall capacitive difference in the space charge region as a function of frequency and potential (the Mott-Schottky relationship). This measurement is commonly employed to determine the flat-band potential. A linear relationship of $1/C^2$ (where C is the capacitance) to the applied potential (E) at each frequency is expected with a constant positive slope for n-type materials.[32] Plotting multiple frequencies leads to more accurate results than does plotting a single frequency, and typically a mid-frequency range is used to obtain the flat-band potential. However, we are particularly interested in exploring a large frequency range to search for a frequency dispersion. A measured capacitance that is frequency-dependent is usually associated with contributions from states in the forbidden gap.[33] It is unlikely to identify these mid-gap states in the dark using the frequency range typical for Mott-Schottky analysis, as it excludes electronic transitions to mid-gap states.[34] To see these transitions, it is useful to apply the AC perturbation at low frequencies (0.1 – 10 Hz) in the dark.[35] Low frequencies are required because the time scale of such electronic transitions mandates longer perturbation times in order to obtain measurable changes in capacitance. We have therefore surveyed a large frequency range, specifically focusing on low-frequency perturbations–down to 0.1 Hz. The Mott-Schottky (M-S) data for several frequencies obtained in the dark at pH 7.00 is plotted in Figure B.2. In the low-frequency regime (0.1 – 10 Hz), there is a downward shift in the slope to a near-constant capacitance value in the potential range of ~0.8 – 1.0 V at 0.55 Hz. This change in slope suggests Fermi-level (E_F) pinning due to a mid-gap state.[35] M-S analysis under illumination is also expected to show a frequency dependence as well as E_F pinning. Additionally, since photoexcited charges represent a non-equilibrium condition in the

space charge region and a Faradaic reaction is occurring (unlike in the dark), it is possible for the pinning to be detectable at frequencies above 10 Hz. M-S analysis at 100 mW/cm^2 illumination, plotted at several frequencies for comparison, also demonstrates a frequency dependence; the slope changes between ~0.75 V to 0.95 V at 104 Hz (Figure 3.3), which indicates the presence of a mid-gap state.[36,37] E_F pinning at the lower light intensities of 50 and 15 mW/cm^2 is not obvious above frequencies of 47 and 14 Hz, respectively (Figure B.4 and Figure B.5). The frequency dependence of the pinning in the dark and under illumination as a function of photon flux explains how the occupation of the mid-gap state relates to the Fermi level.[36] Compared to 100 mW/cm^2, the mid-gap state is still observed with 50 and 15 mW/cm^2, but having fewer photogenerated electron-hole pairs results in a decrease in the capacitance of the mid-gap state. Therefore, a lower frequency/longer perturbation time is needed to observe the pinning. As a result, the electric field created by charging the mid-gap state is less disrupted at 104 Hz, and a change in slope is not observed between ~0.75 – 0.95 V in the M-S plot for 50 and 15 mW/cm^2 at this higher frequency (Figure B.4 and Figure B.5). The change in slope in the dark and also under illumination suggests that the mid-gap state is a permanent state as opposed to one that is only photogenerated.[38–40] These results corroborate our LSV data, in which significant photocurrent is not produced until 1.01 V is applied. At this potential, the Fermi level is no longer pinned, resulting in a return to a constant slope.

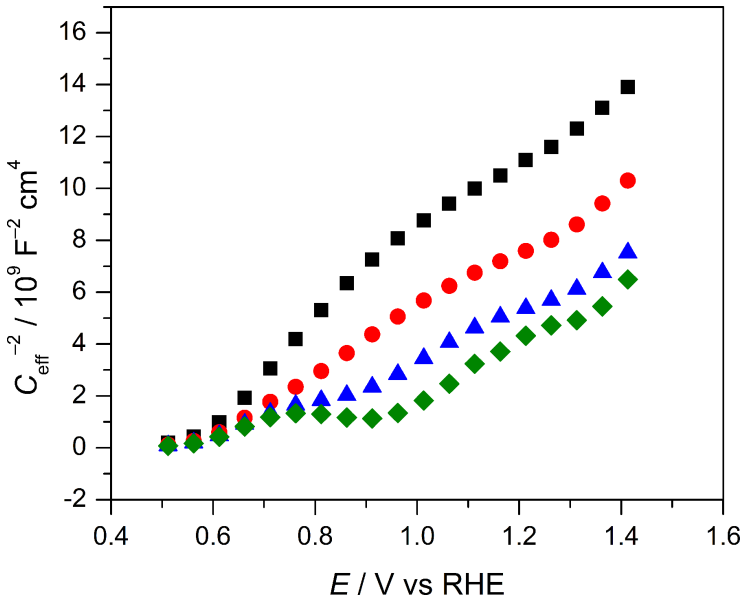

Figure 3.3 Mott-Schottky analysis of impedance data collected at 100 mW/cm^2 in 0.5 M KB_i, 0.2 M KCl buffer (pH 7.00) at varying frequency: 1164 Hz (black squares), 348 Hz (red circles), 104 Hz (blue triangles), and 47 Hz (green diamonds).

In order to elucidate whether water oxidation occurs from the mid-gap state or from the valence band, it is first necessary to discuss the Fermi level in terms of hole transfer. Our EIS data under illumination reveal that any hole transfer from the valence band in the potential range of 0.81 to 1.01 V is improbable due to the Fermi level pinning. EIS does not allow one to pinpoint the specific energetic location of the state, however it does provide experimental evidence to determine at what energy the mid-gap state interacts with solution species to perform the chemical reaction based on the applied potential. The energy at which the Fermi level is pinned is sometimes identified as the energy of the mid-gap state.[41] However, the Fermi level measured is additive (quasi-Fermi level of electrons, E_{Fn} + quasi-Fermi level of the mid-gap state, E_{Fs}) and therefore, it is possible that filling a mid-gap state located energetically below the thermodynamic water oxidation potential causes the total Fermi level, E_F, to pin at more negative potentials than the actual location of the mid-gap state.[41]

We have looked at the M-S data and identified individual frequency-dependent events as a result of measuring charge storage in the space-charge region during the water oxidation reaction. We have also correlated them to the generated photocurrent we observe for $CuWO_4$. However, a complete analysis of how $CuWO_4$ transfers holes to water must address the resistance to charge transfer measured at the surface. A Nyquist plot informs us of the impedance to charge transfer resistance (Z') and impedance due to capacitance (Z'') as a function of frequency. The Nyquist plot for $CuWO_4$ in Figure 3.4 shows two semicircles in pH 7.00 buffer at 0.96 V under 1-sun illumination. A mid-gap state manifests as two separate semicircles, which indicates two separate charge-transfer events occurring at the electrode surface. Each process corresponds to an *RC* circuit: *RC1* is attributed to non-Faradaic capacitive events in the depletion region, and the second semicircle, *RC2*, commonly represents the interaction with the solution, where a Faradaic reaction can be monitored.[42] Non-Faradaic processes typically respond to higher frequency perturbations since interacting with the solution is prevented by the fast voltage switching. The opposite is true for Faradaic processes which need lower-frequency perturbations to measure interfacial electron transfer. The evolution of two processes in the Nyquist plot as a function of applied potential is illustrated in Figure B.6. To focus specifically on the change in capacitive processes as a function of applied potential, we refer to the Bode plots (phase angle and total impedance *vs*. log frequency). A clear frequency dependence as well as deconvolution into more than one capacitive event is evident at the $CuWO_4$-electrolyte interface. The evolution of two capacitive events is presented in the Bode plots of Figure B.7 and Figure B.8—represented by two peaks in the phase angle Bode plot and a large difference in slope in the total *Z* Bode plot.

At low applied bias (from 0.81 – 1.11 V), two processes are modeled that contribute to the water oxidation reaction; at 1.16 V, only 1 process is identified. The EIS data from 0.81 – 1.11 V was fit with the circuit in 1b providing two parallel relationships. R_s represents the additive representation of the electrode and solution resistance.

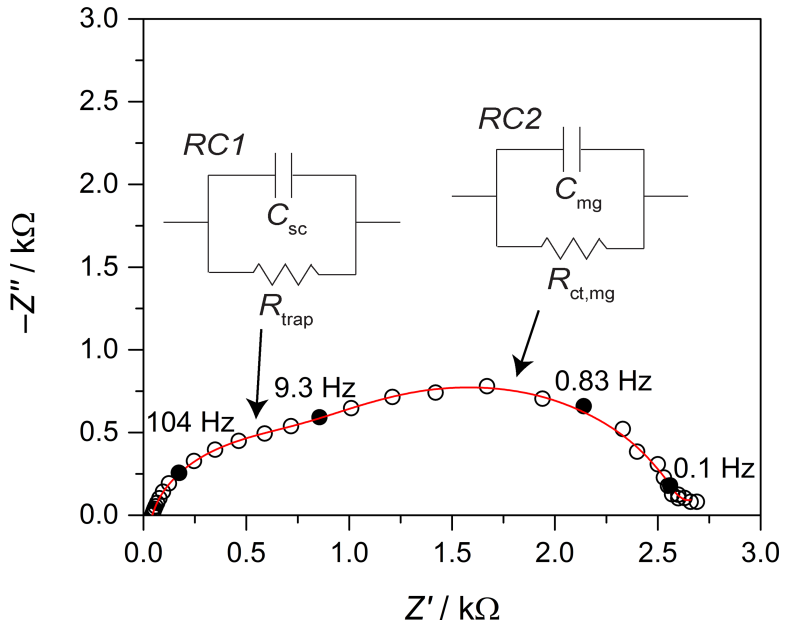

Figure 3.4 Nyquist plot for EIS data measured in 0.5 M KB$_i$ and 0.2 M KCl at pH 7.00, AM1.5G irradiation at 100 mW/cm^2, and 0.96 V *vs* RHE. Data is shown as black circles, and the fit is the red line. The processes are labeled with equivalent circuits and *RC1* and *RC2*, which correspond to those drawn in **Figure 3.1**b.

For $CuWO_4$ under illumination, the semicircle labeled *RC1* in Figure 3.4 is represented as the parallel relationship between R_{trap} and C_{sc}, where R_{trap} is the resistance to trapping/detrapping electrons in/out of the mid-gap state and C_{sc} is the capacitance of the space-charge region. The semicircle *RC2* represents the parallel relationship between $R_{ct,mg}$ and C_{mg}, where $R_{ct,mg}$ is the resistance to charge transfer at the surface/solution interface (to perform water oxidation) from the mid-gap state and C_{mg} is capacitance of the mid-gap state (see Figure 3.1a and b).[29] Fitting the EIS data to a specific circuit provides an output for each circuit element individually. The fitting line is shown in each

Nyquist plot and Table B.1 and Table B.2 present the output data. We have plotted the output data for each circuit element in log form as a function of potential in Figure 3.5. The data in Figure 3.5 will be discussed with respect to 100 mW/cm^2 illumination intensity and is plotted in the black circles. We are now able to track the storage and transfer of electrons within the space-charge region and determine how the mid-gap state contributes to the water oxidation reaction.

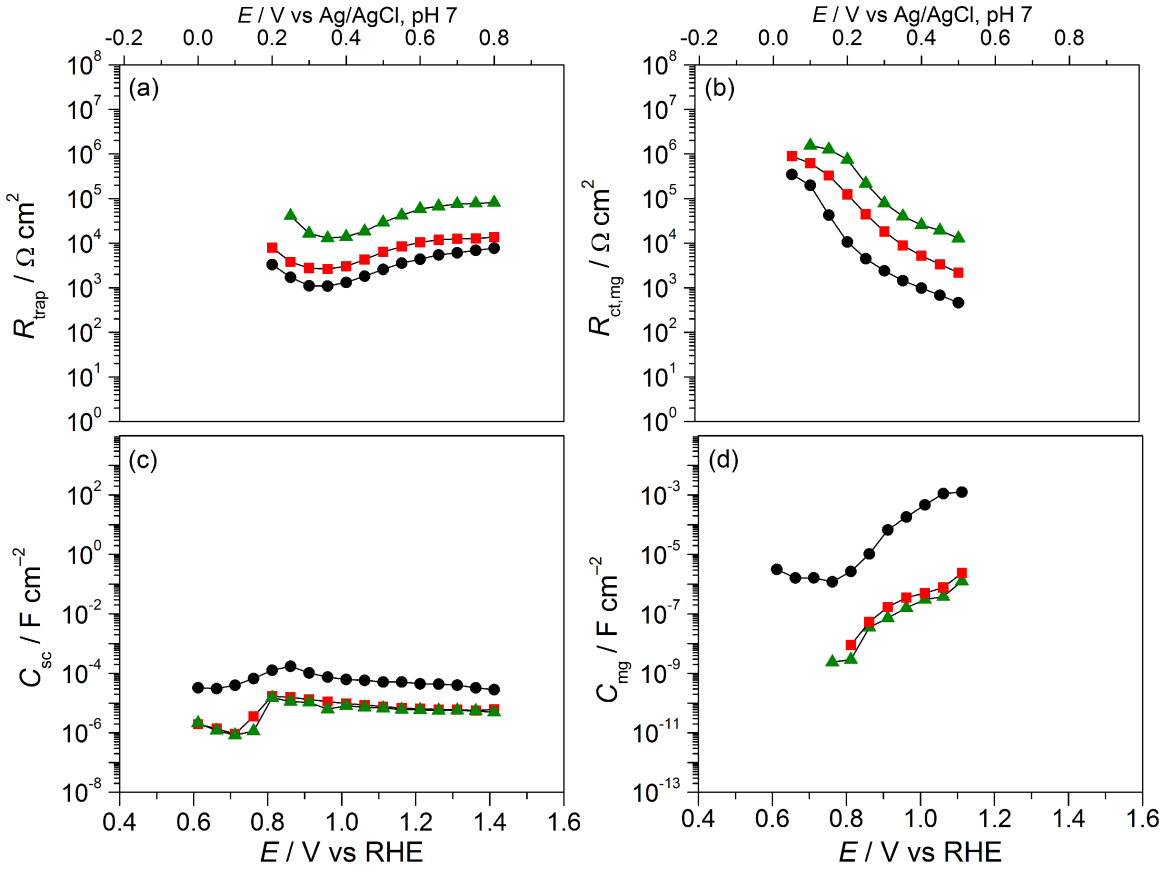

Figure 3.5 Circuit elements as a function of potential and light intensity (100 mW/cm^2, black circles; 50 mW/cm^2, red squares; and 15 mW/cm^2, green triangles). (a) R_{trap} (b) $R_{ct,mg}$ (c) C_{sc} (d) C_{mg}. See **Figure 3.1**a and b for electron-transfer pathways and equivalent circuit.

Figure 3.5a shows that R_{trap} gradually increases from ~3.3 × 10^3 Ω cm^2 at 0.81 V to 7.7 × 10^3 Ω cm^2 at 1.41 V. It becomes the dominant resistive process during the reaction, and therefore one *RC* element representing the parallel relationship of R_{trap} and

C_{sc} is used to fit the single semicircle observed at 1.16 and above (Figure B.9). Therefore, we conclude that R_{trap} represents the non-Faradaic process of electron transfer in the space-charge region to and from the mid-gap state (*RC1*). On the other hand, the resistance associated with *RC2*, $R_{ct,mg}$, decreases from ~3.5×10^5 Ω cm^2 at 0.66 V to 4.6×10^2 Ω cm^2 at 1.11 V, until it is too small to measure (Figure 3.5b). The increase in photocurrent with applied potential in the LSV trace supports that this resistive element, $R_{ct,mg}$ indeed represents the Faradaic charge-transfer associated with water oxidation. Therefore, the decrease in $R_{ct,mg}$ and concomitant increase in R_{trap} prevents photoexcited electrons in the space-charge region from recombining in the mid-gap state, but rather promotes electron transfer to the back contact, thereby activating water oxidation starting at 0.80 V. Table B.3 lists the resistance comparison between $R_{ct,mg}$ and R_{trap} in the 0.81 – 1.21 V region. 1.01 V is the first potential for which $R_{ct,mg}$ is smaller than R_{trap} (9.83×10^2 Ω cm^2 and 1.3×10^3 Ω cm^2 respectively). This crossover is significant because it correlates to the potential where the increase in photocurrent is greatest as observed by the derivative of the LSV trace (Figure B.10). Furthermore, 1.01 V corresponds to the unpinning of the Fermi level. However, even as $R_{ct,mg}$ decreases and j_{ph} increases, we still do not observe saturation of j_{ph} (measured up to 550 mW/cm^2, Figure B.11). These observations are consistent with a mid-gap state from which water oxidation occurs.

The trend in the capacitance as a function of increasing potential also supports the presence of a mid-gap state. Figure 3.5c shows that C_{sc} displays a small discharge at 0.86 V, but is otherwise fairly constant. The nearly uniform capacitance with increasing potential above 0.86 V indicates the continuous flow of electrons to the back contact. The capacitance of the mid-gap state, C_{mg}, increases from 1.2×10^{-6} F cm^{-2} at 0.71 V to ~1.2

$\times 10^{-3}$ F cm^{-2} at 1.11 V (Figure 3.5d). Gaussian behavior is commonly observed for a mid-gap state at the surface, representing the charging and discharging of this state as water oxidation proceeds. We observe the capacitive increase beginning at 0.81 V, which we believe represents the first half and the peak maximum in the Gaussian curve, but we are not able to measure the capacitance of this state at potentials greater than 1.11 V due to the rate-limiting resistance of R_{trap} being so much larger than $R_{ct,mg}$. The peak at 1.06 V is concurrent with the greatest increase in photocurrent (dj/dE) and the unpinning of the Fermi level. This observation indicates that as the reaction proceeds, electrons from solution populate the mid-gap state, and the increase in C_{mg} suggests hole transfer from the valence band to the mid-gap state is rate limiting.

Performing the EIS measurements as a function of light intensity validates our model circuit. We applied a photon flux of 100, 50, and 15 mW/cm^2 illumination, and note that the data trend as expected. First, lower capacitance values confirm the excitation of fewer electrons as intensity decreases. Additionally, resistance increases as light intensity decreases, but still follows the same trend explained previously. Fewer electron-hole pairs generated for 15 mW/cm^2 compared to 100 mW/cm^2 results in a smaller photopotential and thus an overall increase in both the resistance to perform water oxidation from the mid-gap state ($R_{ct,mg}$) and in the resistance to shuttle electrons back-and-forth from the mid-gap state in the space-charge region (R_{trap}).

Finally, if the mid-gap state is in equilibrium with the solution, we should observe a Nernstian shift with pH. We do in fact observe a shift of ~62 mV/pH unit comparing our data at pH 7.00 to a pH 9.24 KB$_i$ buffer. The onset of photocurrent at pH 9.24 is 0.79 V *vs* RHE, the same as pH 7.00 (Figure B.12). Comparing the circuit elements for *RC2*,

which involve the processes at the mid-gap state, the $R_{ct,mg}$ values and peak position of C_{mg} at 100 mW/cm^2 for pH 7.00 and pH 9.24 show that they overlay on one another when corrected for pH and plotted *vs* RHE (Figure 3.6a and Figure 3.6b). The data in Figure 3.6 also support the fact that the fitted circuit elements at pH 9.24 reveal the same trends seen at pH 7.00, and a similar magnitude of C_{mg} 1.7 × 10^{-3} F cm^{-2} is observed at the peak. The same trend in pH is also observed with the Fermi level pinning shown in

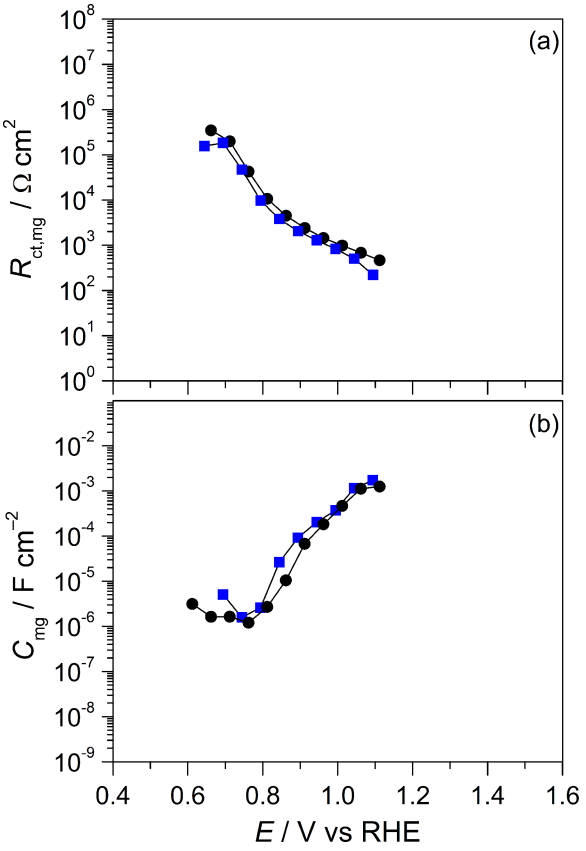

Figure 3.6 (a) $R_{ct,mg}$ and (b) C_{mg} *vs* RHE for the pH dependence of the EIS data under AM1.5G 1-sun illumination at pH 7.00 (black circles) and 9.24 (blue squares) 0.5 M KB$_i$, 0.2 M KCl buffers.

the Mott-Schottky data in the dark (dark M-S at 0.55 Hz in Figure B.13).

We speculate the conduction band of $CuWO_4$ contains Cu(3d) character, in agreement with recent DFT calculations by Lalić et *al.* and our experimental observations.[5,43] The Jahn-Teller distortion of Cu^{2+} gives rise to a d-orbital splitting in

which the degeneracy of the σ-antibonding orbitals is broken.[44] In the spin-polarized Pauli model, the singly-occupied d_{x2-y2} orbital splits,[45] suggesting that this level could produce a mid-gap state comprising copper character. Alternatively, the mid-gap state may be due to the surface relaxation of the crystal termination of $CuWO_4$. X-ray photoelectron spectroscopy shows that the top of the valence band is dominated by Cu(3d) orbitals as well.[46,47] These results support the claim that a mid-gap region is likely composed of Cu-based orbitals. EIS was also performed on single crystals of $CuWO_4$ grown by a molten salt synthesis with 010 faces exposed identified by XRD (Figure 3.9). An area corrected linear sweep voltammogram is shown in Figure 3.7. There is a larger overpotential associated with the single crystals because of the large resistance due to the 10-20 μm thickness of the single crystals grown (single crystal size 0.3 x 0.9 x .02 mm)

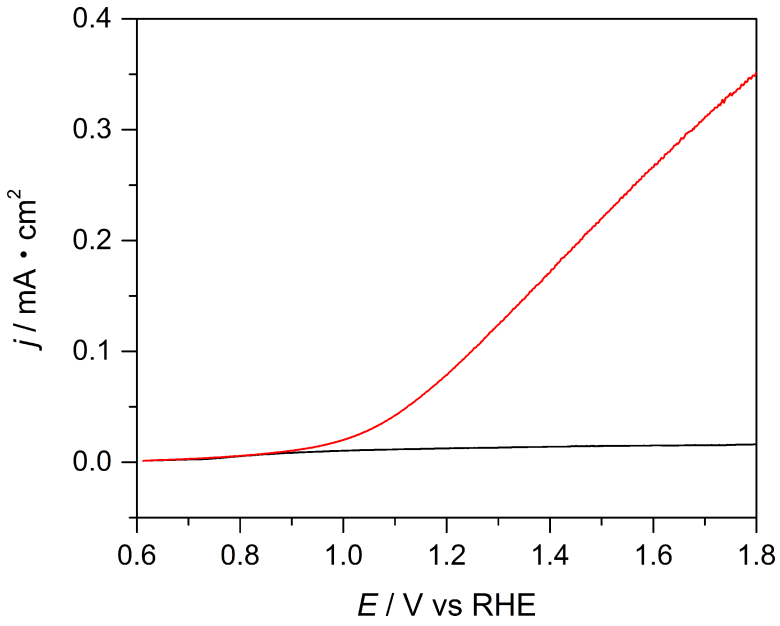

Figure 3.7 Linear sweep voltammogram in the dark (black) and AM1.5G irradiation at 100 mW/cm^2 (red) for $CuWO_4$ single crystal films in 0.5 M KB_i, 0.2 M KCl buffer at pH 7.00.

Nyquist plot under 1 sun illumination at 1.20 V vs RHE plotted in Figure 3.8. Two charge transfer events are identified in the Nyquist plot with the same evolution of

semicircles observed with the $CuWO_4$ electrodes produced by sol-gel. Experimental evidence obtained thus far points to a permanent mid-gap state as an inherit property of

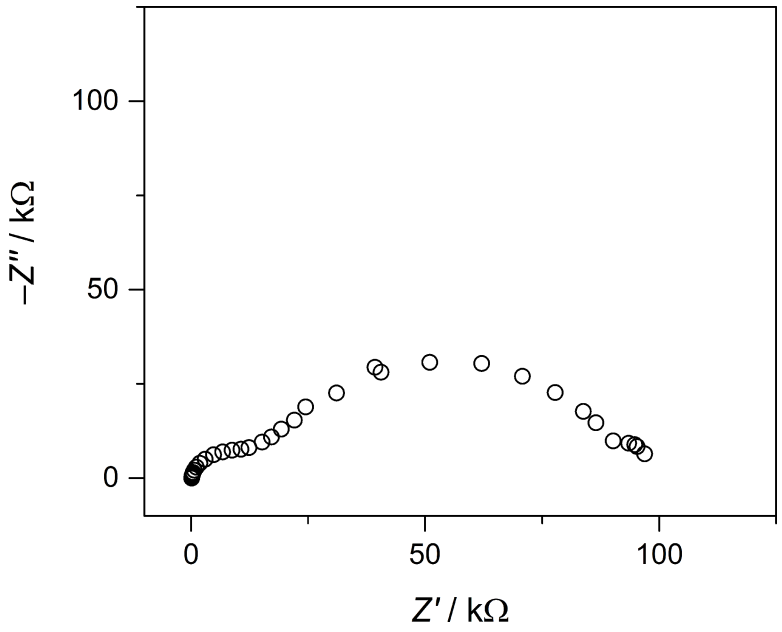

Figure 3.8 Nyquist plot for EIS data measured in 0.5 M KB_i and 0.2 M KCl at pH 7.00, AM1.5G irradiation at 100 mW/cm^2, and 1.20 V *vs* RHE. Two charge transfer events are identified.

the material as opposed to a defect associated with the synthesis method. The Fermi level pinning in the dark also provides evidence for a permanent mid-gap state as opposed to a photogenerated one. As mentioned briefly in the introduction, cobalt oxide or cobalt oxide stabilized by phosphate has been deposited onto metal oxide surfaces like that of Fe_2O_3,[48] $BiVO_4$,[49] WO_3[50] acting as a hole scavenger preventing detrimental surface recombination due to slow surface kinetics associated with the 4-proton and 4-electron water oxidation reaction. However, when these cobalt oxide species are deposited onto $CuWO_4$ sol gel or single crystal electrodes, there is a decrease in photocurrent observed for the water oxidation reaction. We believe this is due to the role of these Cu(3d) orbitals within the gap preventing the oxidation of Co^{3+} to Co^{4+} therefore rendering it much less active for water oxidation.

Photoemission studies such as angle resolved, resonance, or inverse photoemission spectroscopy are being pursued and will help to verify the experimental evidence obtained from our EIS studies.[51] Understanding the influence of a mid-gap state on the photoelectrochemistry of $CuWO_4$ informs us how to optimize its performance. So far, co-catalyst loading strategies common to $BiVO_4$ and Fe_2O_3 have proven to be unfruitful for increasing the photocurrent density. Therefore, the knowledge gained from this EIS study as well as pinpointing the energetic location by photoemission spectroscopy provides valuable insight for identifying improvements for enhanced performance.

3.3 Conclusions

We used electrochemical impedance spectroscopy to probe the surface/solution interface and electronic characteristics of $CuWO_4$ in the dark and under AM1.5G illumination. The evolution of two events in the Nyquist and Bode data as well as Fermi level pinning from 0.81-1.01 under illumination suggests a mid-gap state is present. The presence of Fermi level pinning in the same potential range in the dark suggests that the state is permanent, and not photogenerated. The data were fit with a suitable equivalent circuit, and revealed two parallel relationships: *RC1*, non-Faradaic events, C_{sc} and R_{trap}, represent the trapping/detrapping of electrons to and from the mid-gap state; and *RC2*, Faradaic events, C_{mg} and $R_{ct,mg}$, represent water oxidation through the mid-gap state. Differing illumination intensity supports the equivalent circuit assignment. The pH dependence of the mid-gap state is shown at pH 7.00 and 9.24 to shift at ~62 mV/pH demonstrating a Nernstian response.

3.4 Experimental Section

3.4.1 Synthesis and Electrode Fabrication

The synthesis and characterization of the thin-film $CuWO_4$ photoanodes is presented in reference 5. Briefly, $CuWO_4$ was prepared from an ethylene glycol mixture of $Cu(NO_3)_2 \bullet 3H_2O$ and $(NH_4)_6H_2W_{12}O_{14}$, and was deposited on an FTO substrate by sol-gel processing. Films were heated at 550 °C for 1 h in a muffle furnace, with 1 h ramp for heating and cooling. The thin films are ~200 nm thick interconnected crystallites (Figure B.14). Electrode areas were defined using a 60 μm surlyn film (Solaronix) with a 0.32 cm^2 area. Surlyn was attached by heating the films to 180 °C for 10 min and cooled in ambient air. Single crystals were synthesized by a molten salt synthesis similar to that of reference 52 where an equimolar mixture of Na_2WO_4 and $Cu(NO_3)_2$ was ground together and heated in a ceramic crucible at 950 °C for 15 hours with a slow cooling rate of 2 °C per hour to 700 °C then 50 °C per hour down to room temperature. The crystals were cleaved and the polished using alumina powder of particle size 1 μm, 0.3 μm and 0.05 μm. An electrode was made by contacting the single crystal using indium gallium eutectic to silver print. The silver print was contacted to a tin coated copper wire and epoxied to glass tubing. X-ray diffraction displays pure $CuWO_4$ with (010), (020), and (030) hkl peaks in Figure 3.9.

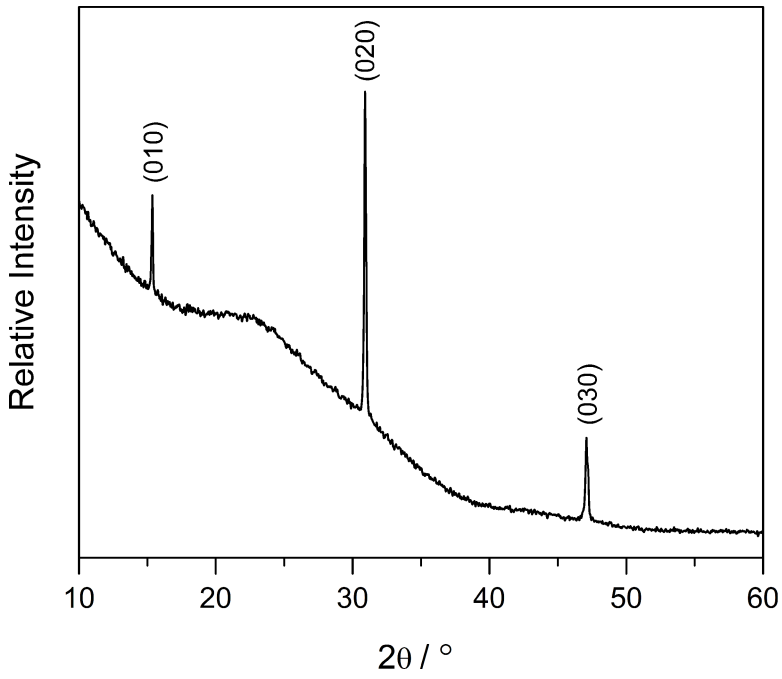

Figure 3.9 XRD of $CuWO_4$ single crystal synthesized by molten salt synthesis with (010) face exposed. The broad peak at 22° 2θ is due to the glass slide.

3.4.2 Photoelectrochemistry and Electrochemical Impedance Spectroscopy

Photoelectrochemical (PEC) measurements were performed using a custom-built, three-electrode Pyrex glass cell with a quartz viewing window. The cell contained the working thin-film $CuWO_4$ photoanode, Ag/AgCl reference electrode in saturated KCl (+0.20 V *vs* NHE), and a platinum auxiliary electrode. For water oxidation, the supporting electrolyte used was a 0.5 M potassium borate buffer (KB_i) solution at pH 7.00 and at pH 9.24 with 0.2 M potassium chloride supporting electrolyte. Electrical contact was made to the FTO substrate by attaching copper wire purchased from Fisher Scientific and using CG Electronics Silver Print II. Electrodes were sealed using Loctite Hysol 1C epoxy. The light source was a Newport-Oriel 150 W Xe arc lamp fitted with a Newport AM 1.5G filter to simulate incident solar radiation. For certain experiments the lamp power was adjusted to 100 mW/cm^2, 50 mW/cm^2 and 15 mW/cm^2 as noted using an Newport 1918-R optical power meter equipped with a Newport 818P-015-19 thermopile

detector. Voltammetry measurements were performed with a CH Instruments 660C Electrochemical Workstation.

Electrochemical impedance spectroscopy was carried out with an Eco Chemie Autolab PGSTAT302N potentiostat with a frequency-response analysis (FRA) module. Measurements were recorded from 0.0 to 0.80 V *vs* Ag/AgCl at pH 7.00 (0.61 to 1.41 V *vs* RHE) and –0.30 to 0.80 V *vs* Ag/AgCl at pH 9.24 (0.44 to 1.54 V *vs* RHE) in 50 mV increments with a 5-minute equilibration time at each potential. A range of frequencies between 0.01 and 65,000 Hz was used with a 10 mV amplitude perturbation. Data were fit using Zview™ software.

3.5 References

1. Herrero, C.; Lassalle-Kaiser, B.; Leibl, W.; Rutherford, A. W.; Aukauloo, A. Artificial Systems Related to Light Driven Electron Transfer Processes in PSII *Coord. Chem. Rev*. **2008**, *252*, 456-468.
2. Armaroli, N.; Balzani, V. The Future of Energy Supply: Challenges and Opportunities *Angew. Chem. Int. Ed.* **2007**, *46*, 52-66.
3. Currao, A. Photoelectrochemical Water Splitting *Chimia* **2007**, *67*, 815-819.
4. Yourey, J. E.; Bartlett, B. M. Electrochemical Deposition and Photoelectrochemistry of $CuWO_4$, a Promising Photoanode for Water Oxidation *J. Mater. Chem.* **2011**, *21*, 7651-7660.
5. Yourey, J. E.; Pyper, K. J.; Kurtz, J. B.; Bartlett, B. M. Chemical Stability of $CuWO_4$ for Photoelectrochemical Water Oxidation *J. Phys. Chem. C* **2013**, *117*, 8708-8718.
6. Zhong, D. K.; Gamelin, D.R. Photoelectrochemical Water Oxidation by Cobalt Catalyst ("Co-Pi")/α-Fe_2O_3 Composite Photoanodes: Oxygen Evolution and Resolution of a Kinetic Bottleneck *J. Am. Chem. Soc.* **2010**, *132*, 4202-4207.
7. Berglund, S. P.; Flaherty, D. W.; Hahn, N. T.; Bard A. J.; Mullins, C. B. Photoelectrochemical Oxidation of Water Using Nanostructured $BiVO_4$ Films *J. Phys. Chem. C* **2011**, *115*, 3794-3802.
8. Cowan, A.C ; Tang J.; Leng,W.; Durrant, J. R; Klug, D. R. Water Splitting by Nanocrystalline TiO2 in a Complete Photoelectrochemical Cell Exhibits Efficiencies Limited by Charge Recombination J. Phys. Chem. C 2010, 114, 4208-4214.
9. Gerischer, H.; Mattes, I. Über die Mitwirkung von Oberflächenzuständen bei Redoxreaktionen an Halbleitern Z. Phys. Chem. 1967, 52, 60-72.
10. Mora-Seró, I.; Luo, Y.; Garcià-Belmonte, G.; Bisquert, J.; Muñoz, D.; Voz, C.; Puigdollers, J.; Alcubilla, R. Recombination Rates in Heterojunction Silicon Solar Cells Analyzed by Impedance Spectroscopy at Forward Bias and Under Illumination Sol. Energy Mater. Sol. Cells 2008, 92, 505-509.

11. Chou, J-C.; Lin, S-A.; Lee, C-Y.; Gan, J-Y. Effect of Bulk Doping and Surface-trapped States on Water Splitting with Hematite Photoanodes J. Mater. Chem. A 2013, 1, 5908-5914.
12. Sivula, K.; Zboril, R.; Formal, F. L.; Robert, R.; Weidenkaff, A.; Tucek, J.; Frydrych, J.; Grätzel, M. Photoelectrochemical Water Splitting with Mesoporous Hematite Prepared by a Solution-Based Colloidal Approach J. Am. Chem. Soc. 2010, 132, 7436-7444.
13. Klahr, B.; Gimenez, S.; Fabregat-Santiago, F.; Bisquert, J.; Hamann, T. W. Electrochemical and Photoelectrochemical Investigation of Water Oxidation with Hematite Electrodes Energy Environ. Sci. 2012, 5, 7626-7636.
14. Klahr, B. W.; Gimenez, S.; Fabregat-Santiago, F.; Bisquert, J.; Hamann, T. W.Photoelectrochemical Impedance Spectroscopic Investigation of Water Oxidation with "Co-Pi" coated Hematite Electrodes J. Am. Chem. Soc. 2012, 134, 4294-4302.
15. Brillet, J.; Grätzel, M.; Sivula, K. Decoupling Feature Size and Functionality in Solution-Processed, Porous Hematite Electrodes for Solar Water Splitting Nano Lett. 2010, 10, 4155-4160.
16. Beermann, N.; Vayssieres, L.; Lindquist, S-E.; Hagfeldt, A. Photoelectrochemical Studies of Oriented Nanorod Thin Films of Hematite J. Electrochem. Soc. 2000, 147, 2456-2461.
17. Cesar, I; Kay, A.; Martinez, J. A. G.; Grätzel, M. Translucent Thin Film Fe_2O_3 Photoanodes for Efficient Water Splitting by Sunlight: Nanostructure-directing Effect of Si-doping J. Am. Chem. Soc. 2006, 128, 4582-4583.
18. Shinar, R.; Kennedy, J. H. Photoactivity of Doped α- Fe_2O_3 Electrodes Sol. Energy Mater. 1982, 6, 323-335.
19 Sanchez, C.; Siber, K. D.; Somorjai, G. A. The Photoelectrochemistry of Niobium Doped α- Fe_2O_3 J. Electroanal. Chem. and Intrafac. Electrochem. 1988, 252, 269-290.
20. Abdi, F. F.; Van de Krol, R. J. Nature and Light Dependence of Bulk Recombination in Co-Pi Catalyzed $BiVO_4$ Photoanodes J. Phys. Chem. C 2012, 116, 9398-9404.
21. Seabold, J. A.; Choi, K-S. Effect of a Cobalt-based Oxygen Evolution Catalyst on the Stability and the Selectivity of Photo-oxidation Reactions of a WO3 Photoanode Chem. Mater. 2011, 23, 1105.
22. McDonald, K. J.; Choi, K-S. Photodeposition of Co-based Oxygen Evolution Catalysts on α- Fe_2O_3 Photoanodes Chem. Mater. 2011, 23, 1686.
23. Sivula, K.; Le Formal, F.; Grätzel, M. Solar Water Splitting: Progress Using Hematite (α- Fe_2O_3) Photoelectrodes Chem. Sus. Chem. 2011, 4, 432-449.
24. Cardon, F. Impedance- and Noise-Spectrum Calculation for a Semiconductor-Electrolyte Interface with Electron Transfer Through Surface States Physica 1972, 57, 390-396.
25. Bisquert, J. Theory of the Impedance of Charge Transfer via Surface States in Dye-Sensitized Solar Cells J. Electroanal. Chem. 2010, 646, 43-51.
26. Bard, A. J.; Fan, F-R. F.; Gioda, A. S.; Nagasubramanian, G.; White, H. S. On the Role of Surface States in Semiconductor Electrode Photoelectrochemical Cells Faraday Discuss. Chem. Soc. 1980, 70, 19-31.
27. Orazem, M. E, The Impedance Response of Semiconductors: an Electrochemical Engineering Perspective Chem. Eng. Ed. 1990, 24, 48-55.

28. Orazem, M. E.; Tribollet, B. Electrochemical Impedance Spectroscopy, John Wiley & Sons, Inc., 2008; Chp. 9; pp. 156, 163.
29. Bertoluzzi, L.; Bisquert, J. Equivalent Circuit of Electrons and Holes in Thin Semiconductor Films for Photoelectrochemical Water Splitting Applications J. Phys. Chem. Lett. 2012, 3, 2517-2522.
30. Klahr, B. W.; Gimenez, S.; Fabregat-Santiago, F.; Bisquert, J.; Hamann, T. W.Photoelectrochemical Impedance Spectroscopic Investigation of Water Oxidation with "Co-Pi" coated Hematite Electrodes J. Am. Chem. Soc. 2012, 134, 4294-4302.
31. Zhong, D. K; Choi, S.; Gamelin, D. R. Near-complete Suppression of Surface Recombination in Solar Photoelectrolysis by "Co-Pi" Catalyst-modified W: $BiVO_4$ J. Am. Chem. Soc. 2011, 133, 18370-18377.
32. Orazem, M. E.; Tribollet, B. Electrochemical Impedance Spectroscopy, John Wiley & Sons, Inc., 2008; Chp. 12; pp. 227-229
33. Horowitz, G. Capacitance-Voltage Measurements and Flat-Band Potential Determination on Zr-Doped α- Fe_2O_3 Single-Crystal J. Electroanal. Chem. 1983, 159, 421-436.
34. Orazem, M. E.; Tribollet, B. Electrochemical Impedance Spectroscopy, John Wiley & Sons, Inc., 2008; Chp. 13; pp. 225
35. Mahé, E.; Rouelle, F.; Darolles, I.; Devilliers, D. Electrochemical Characterization of Silicon Electrodes: Part 1: Capacitance-voltage Method J. New Mat. Electr. Sys. 2006, 9, 257-268.
36. Bard, A. J.; Bocarsly, A. B.; Fan, F-R. F.; Walton,E. G.; Wrighton M. S. The Concept of Fermi Level Pinning at Semiconductor/Liquid Junctions. Consequences for Energy Conversion Efficiency and Selection of Useful Solution Redox Couples in Solar Devices J. Am. Chem. Soc. 1980, 102, 3671-3677.
37. Cowley, A. M.; Sze, S. M. Surface States and Barrier Height of Metal-semiconductor Systems J. Appl. Phys. 1965, 36, 3212.
38. Klahr, B. M.; Gimenez, S.; Fabregat-Santiago, F.; Hamann, T. W.; Bisquert, J. Water Oxidation at Hematite Photoelectrodes: The Role of Surface States J. Am. Chem. Soc. 2012, 134, 4294-4302.
39. Hens, Z. The Electrochemical Impedance of One-Equivalent Electrode Processes at Dark Semiconductor|Redox Electrodes Involving Charge Transfer through Surface States. 1. Theory J. Phys. Chem. B 1999, 103, 122-129.
40. Hens, Z.; Gomes, W. P. The Electrochemical Impedance of One-Equivalent Electrode Processes at Dark Semiconductor|Redox Electrodes Involving Charge Transfer through Surface States. 2. The n-GaAs/Fe3+ System as an Experimental Example. J. Phys. Chem. B 1999, 103, 130-138.
41. Mora-Seró, I.; Bisquert, J. Fermi Level of Surface States in TiO2 Nanoparticles Nano Lett. 2003, 3, 945-949.
42. Orazem, M. E.; Tribollet, B. Electrochemical Impedance Spectroscopy, John Wiley & Sons, Inc., 2008; Chp. 13; pp. 330
43. Lalić, M. V.; Popović, Z. S.; Vukajlović, F. R. Electronic Structure and Optical Properties of $CuWO_4$: An Ab Initio Study Comp. Mat. Sci. 2012, 63, 163-167.

44. Ruiz-Fuertes, J.; Segura, A.; Rodriguez, F.; Errandonea, D.; Sanz-Ortiz, M. N. Anomalous High-Pressure Jahn-Teller Behavior in $CuWO_4$ Phys. Rev. Lett. 2012, 108, 166402.
45. Doumerc, J.-P.; Hejtmanek, J.; Chaminade, J.-P.; Pouchard, M.; Krussanova, M. A Photoelectrochemical Study of $CuWO_4$ Single Crystal Phys. Stat. Sol. 1984, 82, 285-294.
46. Kuzman, A.; Kalinko, A.; Evarestov R. A. Ab Initio LCAO Study of the Atomic, Electronic and Magnetic Structure and the Lattice Dynamics of Triclinic $CuWO_4$ Acta Mater. 2013, 61, 371-378.
47. Khyzhun, O. Y.; Strunskus, T.; Cramm, S.; Solonin, Y. M. Electronic Structure of $CuWO_4$: XPS, XES, and NEXAFS Studies J. Alloys Compd. 2005, 389, 14-20.
48. McDonald, K.J.; Choi, K.-S. Photodeposition of Co-Based Oxygen Evolution Catalysts on α- Fe_2O_3 Photoanodes Chem. Mater. 2011, 23, 1686-1693.
49. Jeon, T.H.; Choi, W.; Park, H. Cobalt-Phosphate Complexes Catalyze the Photoelectrochemical Water Oxidation of $BiVO_4$ Electrodes Phys. Chem. Chem. Phys. 2011, 13, 21392-21401.
50. Seabold, J. A.; Choi, K.-S. Effect of a Cobalt-Based Oxygen Evolution Catalyst on the Stability and the Selectivity of Photo-Oxidation Reactions of a WO3 Photoanode Chem Mater. 2011, 23, 1105-1112.
51. Carstensen, H.; Claessen, R.; Manzke, R.; Skibowsk, M. Direct Determination of III-V Semiconductor Surface Band Gaps Phys. Rev. B 1990, 41, 9880-9885.
52. Doumerc, J.-P.; Hejtmanek, J.; Chaminade, J.-P.; Pouchard, M.; Krussanova, M. A Photoelectrochemical Study of $CuWO_4$ Single Crystals Phys. Stat. Sol. A 1984, 82, 285.

Chapter 4

Synthesis and Characterization of α-$SnWO_4$ Electrodes for Water Oxidation

Portions of this chapter have been published:
Reproduced with permission from Pyper, K. J.; Evans, T.C.; Bartlett, B.M. *Chinese Chem. Lett.* 2015, *26*, 474-478. Copyright 2015 Elsevier
http://www.sciencedirect.com/science/article/pii/S1001841715000509

4.1 Introduction

With an increasing demand and use of energy worldwide, using semiconductors to harness solar energy has been identified as a viable solution for generating chemical fuels,[1] both to provide the driving force for transforming water into hydrogen, as well as a means to provide the oxidizing power for large industrial processes, thereby replacing harsh chemical oxidants.[2,3] Many metal oxide semiconductors have been interrogated for their chemical stability, optical properties, and surface catalytic reactivity. For example, TiO_2 (Eg = 3.0 eV)[4], Fe_2O_3 (2.2 eV)[5], WO_3 (2.7 eV)[6], $BiVO_4$ (2.4 eV)[7], and $CuWO_4$ (2.4 eV)[8] are n-type semiconductors that have been studied for oxidative catalysis such as water oxidation. A large emphasis has been placed on using materials with a band gap between 2–3 eV since this energy encompasses maximum of the solar spectrum (400 – 800 nm light comprises ~50% of the solar flux that reaches the earth's surface) and

accounts for reaction overpotential. For these purposes, we began exploring the optical and electronic properties of α-$SnWO_4$ as a thin film electrode.

Despite its calculated band gap of 2.5 eV,[9] there are several synthetic challenges for producing α-$SnWO_4$ due to the relative instability of Sn^{2+} compared to Sn^{4+}. Several groups have produced powder samples of orthorhombic α-$SnWO_4$ as well as cubic β-$SnWO_4$ by calcining in either an inert or vacuum atmosphere as well as by hydrothermal processes.[10,11,12] Inert or vacuum atmosphere is necessary because Sn^{2+} is readily oxidized to Sn^{4+} in air. There are examples of forming α-$SnWO_4$ by hydrothermal synthesis methods using surfactants under milder, less oxidizing conditions.[12, 13] However, these syntheses start from an amorphous precipitate having a 1:1 Sn:W ratio. Therefore synthetic methods with these restrictions become increasingly more complicated when extrapolated to thin film synthesis. The most common technique to produce thin film electrodes is depositing a solution of dissolved precursors onto a conducting substrate, followed by high temperature calcination and annealing. In the case of generating $SnWO_4$, the precipitation reaction to generate powder takes place if both precursors are co-dissolved ($SnCl_2(aq) + Na_2WO_4(aq) \rightarrow SnWO_4(s) + 2NaCl(aq)$). Also, solution methods employing WCl_6 and $SnCl_2$ carried out in organic solvents (i.e. ethanol) to control morphology are problematic since combustion of the solvent cannot occur in a reducing or vacuum atmosphere. Herein we demonstrate the first synthetic method to produce phase pure α-$SnWO_4$ film electrodes (i.e.—not produced from a powder slurry) by a simple hydrothermal method on a fluorinated tin oxide (FTO) transparent conducting substrate without using inert or vacuum atmosphere. This synthesis was

accomplished by first synthesizing monoclinic WO_3 on FTO and converting it to α-$SnWO_4$ in an aqueous $SnCl_2$ solution.

4.2 Synthesis, Structure and Morphology

The goal of this work is to synthesize α-$SnWO_4$ electrodes using a simple method that excludes the need for an inert or vacuum atmosphere, and avoids adding an annealing step. We synthesized pure α-$SnWO_4$ films in aqueous $SnCl_2$ solution from a previously synthesized monoclinic WO_3 film. The solution did not require deaeration or handling under inert conditions, as all of the synthetic steps were performed aerobically. Orthorhombic $WO_3 \cdot H_2O$ electrodes were generated by a known hydrothermal synthesis method. This compound is composed of layers of corner sharing octahedrally coordinated $WO_5(H_2O)$ units.[14] Corner sharing WO_6 octahedra comprise the structure after annealing, and a hydrothermal method was employed to convert monoclinic WO_3 to red-brown films of α-$SnWO_4$ in a subsequent hydrothermal reaction using a 0.5 M solution of $SnCl_2$ at pH 1, 4 and 7. XRD patterns show the complete conversion to α-$SnWO_4$ at each pH (Figure 4.1). The *hkl* reflections are shown for low 2θ values for the purposes of discussion. The final α-$SnWO_4$ product is orthorhombic, but also contains corner-sharing WO_6 octahedra with Sn atoms layered in between, illustrated in Scheme 4.1.

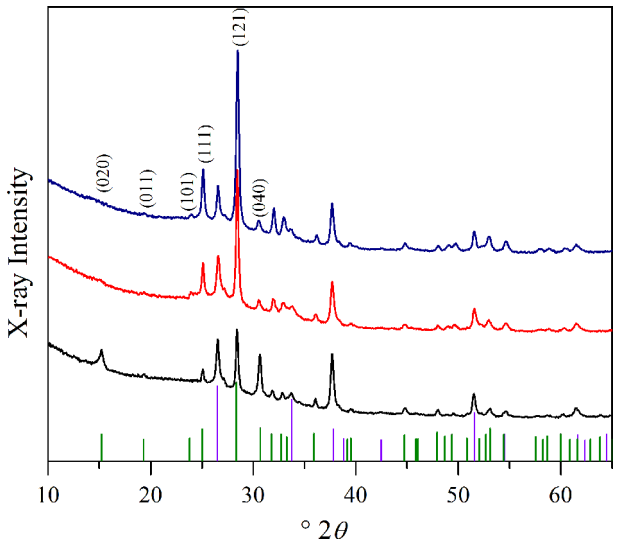

Figure 4.1 X-ray diffraction patterns of pure α-$SnWO_4$ films. From the bottom to the top the pH of the hydrothermal solution was pH 1 (black), pH 4 (red), and pH 7 (blue). FTO peaks are represented by the violet vertical lines and α-$SnWO_4$ is represented by the green vertical lines.

The XRD at pH 1 (black trace Figure 4.1) displays a difference in peak intensity for low 2θ values compared to pH 4 and 7. Specifically the (020), (111), (121), and (040) reflections show a change in intensity. Therefore, the preferred orientation or morphology of the film is directed by the pH of the $SnCl_2$ solution. Converting tungsten oxide hydrate (WO_3•H_2O) films to α-$SnWO_4$ also occurs under

similar conditions at pH 1 (Figure C.1), 3, 4 and 5 (Figure C.2). The WO_3•H_2O films converted to α-$SnWO_4$ at pH 3, 4, and 5 exhibit similar intensities to that of the crystalline WO_3 conversion to α-$SnWO_4$ at pH 4 and 7. However, WO_3•H_2O films converted to α-$SnWO_4$ at pH 1 display similar changes in intensity of *hkl* reflections as seen in the black trace in Figure 4.1. The intensities in

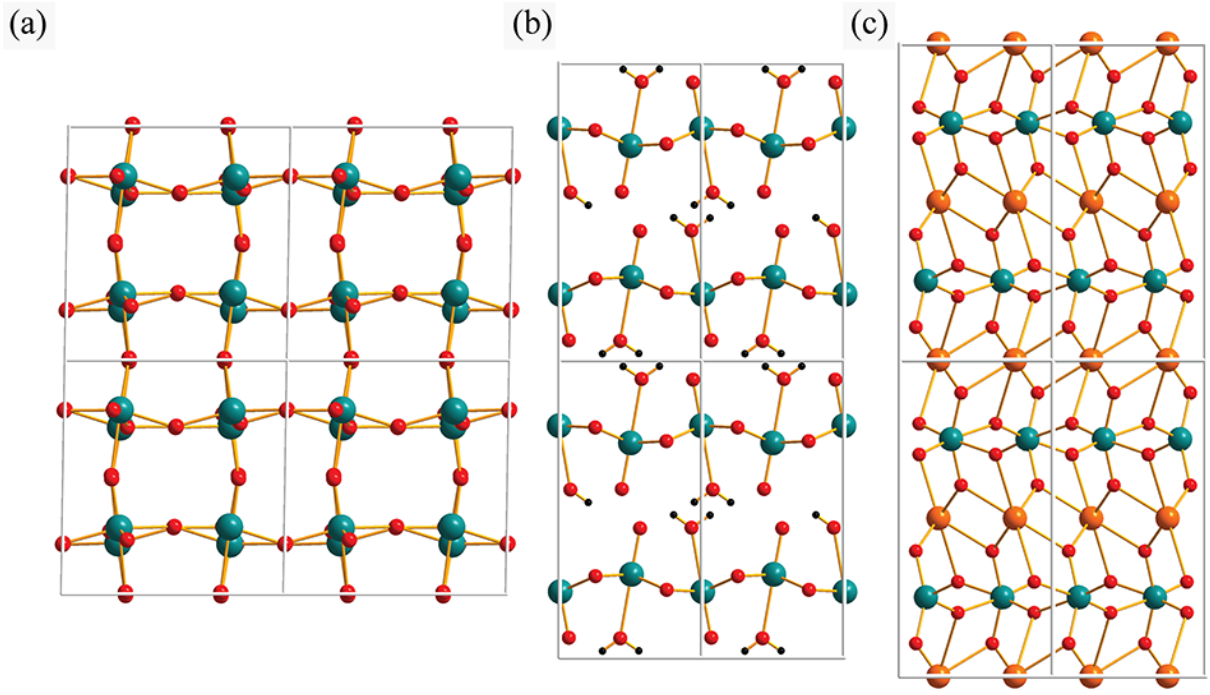

Scheme 4.1 Packing diagrams of a) monoclinic WO_3; b) $WO_3 \cdot H_2O$; c) α-$SnWO_4$

Figure C.1 are stronger than that of the pH 1 solution for crystalline WO_3, which is likely due to the fact that the orthorhombic structure is maintained from $WO_3 \cdot H_2O$ to α-$SnWO_4$ as similar reflections appear in the XRD of the $WO_3 \cdot H_2O$ film before conversion (Figure C.3).

Both $WO_3 \cdot H_2O$ and α-$SnWO_4$ crystallize as orthorhombic structures, and Sn^{2+} has been shown to undergo ion-exchange reactions into other hydrated oxide crystal structures.[14] The changes in intensities for either $WO_3 \cdot H_2O$ or monoclinic WO_3 to α-$SnWO_4$ at pH 1 conversion suggest there is preferred orientation that is different than at higher pH values explored. However, the data discussed in this paper unless otherwise noted refers to conditions and outcomes of the conversion of monoclinic WO_3 to orthorhombic α-$SnWO_4$. The proposed conversion reaction is: $Sn^{2+}(aq) + WO_3(s) +$

$H_2O(l) \rightarrow SnWO_4(s) + 2H^+(aq)$. Evidence in support of this reaction is that the pH of the solution after the reaction is consistently lower: it decreases from pH 7 to ~3; pH 4 decreases to ~2.5; and pH 1 decreases to ~0.65. Furthermore, after hydrothermal treatment, the precipitate remaining in the vessel was collected, and it indexed to $Sn_6O_4(OH)_4$ and SnO by XRD (Figure C.4). The formation of these precipitates also contributes to a drop in the pH of the solution after the completed hydrothermal reaction. While performing the synthesis and adjusting the pH, we found it important to over adjust the pH to 4.5, then and bring it back down to pH 4.0 by titrating in 3 M HCl. The solution composition, and ultimately the α-$SnWO_4$ conversion, depends on whether NaOH is used to adjust the pH, or if both NaOH and HCl are used. With no added HCl, the precipitate remaining after the hydrothermal reaction is dark grey, and indexes mostly to SnO with some $Sn_6O_4(OH)_4$ present (Figure C.5). However, with added HCl adjustment, the precipitate is a peach color and indexes mostly to $Sn_6O_4(OH)_4$ with some SnO present (Figure C.4), in which case we observe consistent conversion to α-$SnWO_4$.

To understand the mechanism by which $Sn_6O_4(OH)_4$ and SnO byproducts are formed, two identical 0.5 M $SnCl_2$ solutions were prepared in beakers under ambient room conditions without adding WO_3-coated FTO films. The pH of the solution in the first beaker (A) was adjusted to 7 with NaOH only, and the pH in the second beaker (B) was adjusted to 7 using NaOH and HCl. A peach-colored precipitate formed immediately from both solutions. The resulting mixtures were then stirred under ambient conditions for 24 hours. The precipitate in beaker A slowly turned light grey and got progressively darker over the course of the 24 hours. The dark grey precipitate indexed to SnO, with only a small amount of $Sn_6O_4(OH)_4$ present. The mixture in beaker B appeared virtually

unchanged after stirring for 24 hours and was indexed as $Sn_6O_4(OH)_4$. We surmise that an equilibrium between $Sn_6O_4(OH)_4$ and SnO exists according to the equation: $Sn_6O_4(OH)_4(s) \rightleftharpoons 6SnO(s) + 2H_2O(l)$, and that without added acid, the equilibrium shifts toward SnO formation due to the acidity of the proton in $Sn_6O_4(OH)_4(s)$. However, when HCl is used, the equilibrium is shifted back toward $Sn_6O_4(OH)_4$. Finally, when NaOH is used alone with $Sn^{2+}(aq)$ in the hydrothermal reaction with WO_3, the conversion is inconsistent and contains patches of unconverted material. This unconverted material appears blue, which indicates reduced tungsten to W^{5+}, commonly observed in the tungsten bronzes.[15] It is clear that once SnO is formed, the composition of the solution is no longer effective for transforming WO_3 to pure α-$SnWO_4$.

One possible film impurity, besides that of incomplete WO_3 conversion, is SnO_2 formation due to Sn^{2+} oxidation under aerobic conditions. Since it would be difficult to identify this phase on the underlying FTO substrate, material comprising the films synthesized at pH 7 was scraped off and characterized by XRD to show that no impurity is obtained (**Figure C.6**). Oxidizing Sn^{2+} is avoided by the use of this hydrothermal method. However, if the hydrothermally synthesized α-$SnWO_4$ product is annealed in air, the material degrades and SnO_2 is the only identifiable product (See Figure C.7 and Figure C.8).

SEM imaging was employed to determine the morphology as a function of pH in the hydrothermal reaction with $SnCl_2$ of which the film XRDs are plotted in Figure 4.1. The SEM image of the WO_3 film before conversion is shown in Figure 4.2a (also

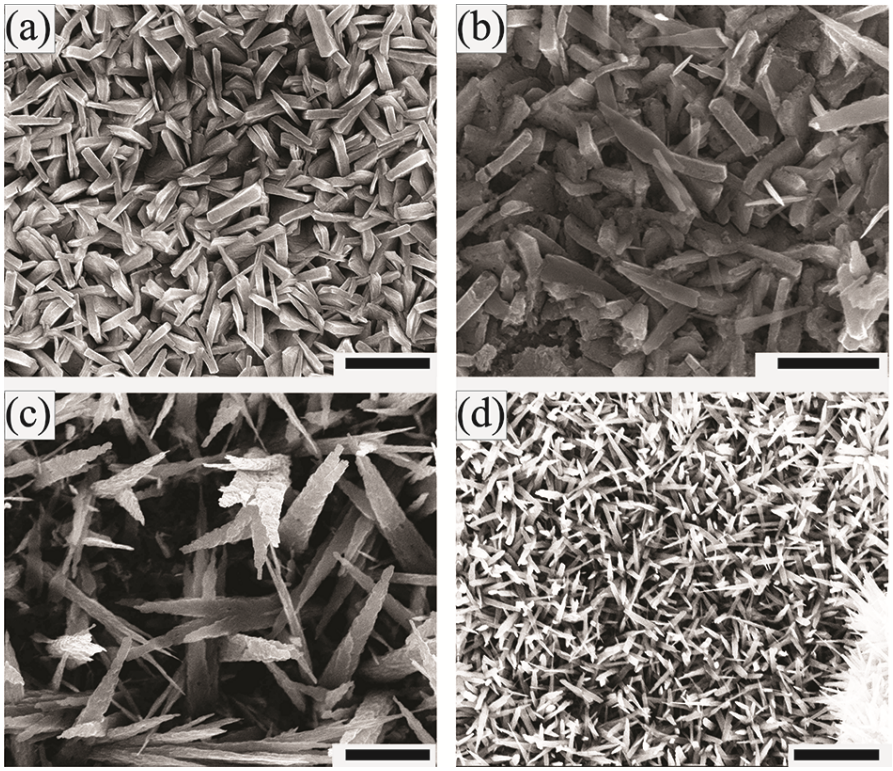

Figure 4.2 SEM images of (a) WO_3 prepared by annealing at 450 °C; b) *α*-$SnWO_4$ produced at pH 1; (c) pH 4; and (d) pH 7. The scale bar in all images is 2 μm.

representative of the $WO_3 \cdot H_2O$ morphology after the initial hydrothermal method). The morphology at pH 1 shows retention of the platelet morphology, except that it has become spongier in appearance. This change likely arises from an expansion of the crystal structure needed to accommodate Sn^{2+} and form the orthorhombic structure. The retention of morphology is also corroborated by the retention of the low two theta reflections at (020) and increase in intensity at (040) with subsequent decrease in the (121) and (111) peaks. There are also belts of material lying across the surface (Figure 4.2b), which possibly contribute to the decrease in intensity of the reflections at (020) that we would expect to appear based upon retaining the orthorhombic structure with preferred orientation in the nanoplatelet morphology. We propose the nanobelts are due to some tungsten oxide dissolution and recrystallization of α-$SnWO_4$ at the surface. A close up of the nanoplatelets before-and-after $SnCl_2$-treatment at pH 1 can be seen in Figure C.9. Two possibilities for α-$SnWO_4$ formation are 1) dissolution of WO_3 and complete recrystallization or 2) formation of α-$SnWO_4$ from Sn^{2+} diffusion into pitted WO_3 nanoplatelets. WO_3 is known to undergo an acid-base reaction to yield soluble WO_4^{2-} in aqueous solution having pH $\geq$ 5. Therefore as the pH increases, soluble WO_4^{2-} provides a plausible pathway for α-$SnWO_4$ crystallization. The morphology at pH 4 is more like that of a branched nanowire morphology, and is shown in Figure 4.2c. The loss in nanoplatelet morphology is also evident in the XRD for the films at pH 4 shown in the red trace in Figure 4.1 as the *hkl* reflections of (020) and (040) show a decrease in intensity as the preferred orientation changes. At pH 7, the film forms dense nanorods, shown in Figure 4.2d. In this case the XRD also displays something similar to that of pH 4 as a nanorod morphology is obtained and the *hkl* reflections of (020) and (040) again

decrease with increasing (111) and (121) peaks. If WO_3 films are included at pH 7 without $SnCl_2$ at 180 °C for 12, 18, and 24 hours, the WO_3 is no longer present on the FTO after the hydrothermal reaction. The same is true if the reaction is carried out in a solution of 1 M NaCl (same chloride concentration). It is evident that crystal structure of the starting material (monoclinic WO_3) must play an important role in the conversion to pure orthorhombic α-$SnWO_4$. Therefore, crystal structure along with solution pH directs morphology and preferred orientation of α-$SnWO_4$ formation. From a synthetic materials standpoint, this experimental evidence supports precedence for conversion of other metal tungstates (*i.e.*—conversion of monoclinic WO_3 to monoclinic $NiWO_4$).

4.3 Visible Light Absorption and Photoelectrochemistry

α-$SnWO_4$ has previously been investigated in powder form as a photocatalyst for oxygen evolution from water, and therefore thin films were of interest to us to employ in a photoelectrochemical cell to carry out the reaction. To determine its suitability for the reaction, we first measured the diffuse reflectance UV-vis spectrum, which is plotted in Figure 4.3. Notably, the absorption onset is at ~650 nm, and α-$SnWO_4$ is determined to be an indirect band gap material with a band-gap energy, E_g = 1.9 eV, shown in the Tauc plot inset of Figure 4.3. A 1.9 eV band gap is significantly smaller than many other *n*-type metal oxide semiconductors such as WO_3, $BiVO_4$, and $CuWO_4$, which makes it of interest for further exploration under visible light irradiation conditions.

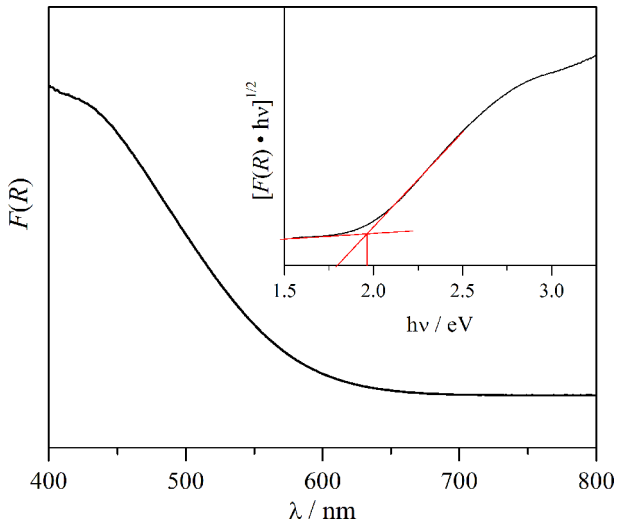

Figure 4.3 Diffuse reflectance UV-vis spectrum (black line). Inset: indirect band-gap Tauc plot.

Next, the photoelectrochemical characteristics were measured to test activity for water oxidation. A chopped light linear sweep voltammogram (LSV) at 100 mW/cm^2 and AM 1.5 (1-sun) illumination in a 0.1 M KP$_i$ buffer solution at pH 5 shows a visible-light response that produces 32 μA/cm^2 at the thermodynamic potential for water oxidation, 1.23 V vs RHE (Figure 4.4). However, long term stability of the material in a highly oxidizing atmosphere is necessary for sustainable use. Investigating the material during

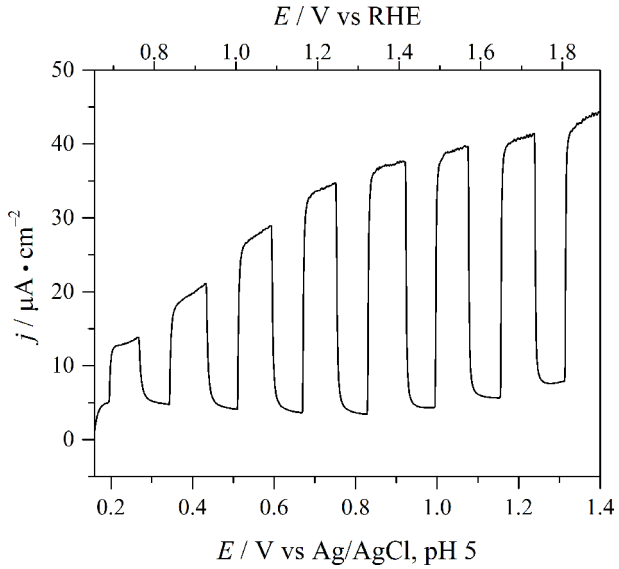

Figure 4.4 Chopped light linear sweep voltammogram of $SnWO_4$ thin films in 0.1 M KP$_i$ buffer at pH 5.00 and AM 1.5G irradiation at 100 mW/cm^2.

long-term photoelectrolysis in a pH 5 0.1 M KP_i buffer at 1-sun illumination and 1.23 V *vs.* RHE (Figure 4.5) shows a steady decrease in the current response (stability) over the course of 6 hours. The data in Figure 4.4 and Figure 4.5 represent films produced at pH 1

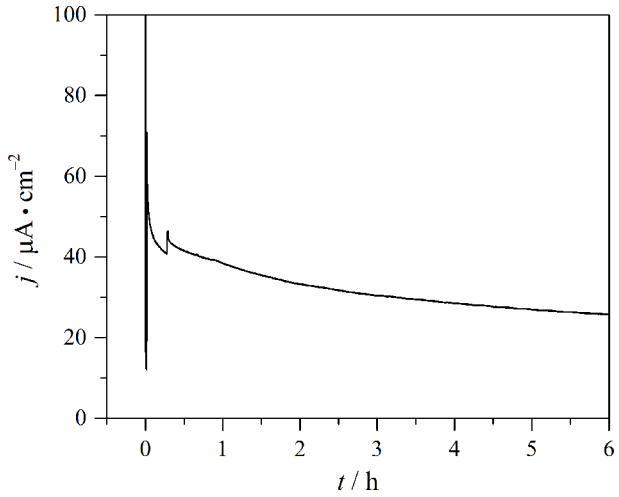

Figure 4.5 Bulk electrolysis at 1.23 V *vs.* RHE of $SnWO_4$ thin films in 0.1 M KP_i buffer at pH 5.00 and AM 1.5G irradiation at 100 mW/cm^2.

with the platelet-like morphology retained. LSV traces under the same conditions were performed on films converted at pH 4 and pH 7, and lower photocurrent was obtained (Figure C.10). Therefore, the sponge-like platelet morphology must play a role in providing increased catalytic activity. The improved photocurrent observed using the films synthesized at pH 1 could also be due to less exposed FTO, which could reduce recombination at the FTO/α-$SnWO_4$ junction. There is also nonzero current under dark conditions that could arise form Sn^{2+} oxidation with increasing potential. We note that the standard electrode potential for $Sn^{4+} + 2e^- \rightarrow Sn^{2+}$ is only + 0.15 V *vs*. NHE. This oxidation occurs readily in aqueous conditions, either in the dark or under illumination. However, no oxidation is observed in non-aqueous and air free conditions when performing a cyclic voltammogram (see Figure C.11). It is unknown whether an oxide surface layer forms or if complete oxidation occurs under long-term photoelectrolysis

conditions. Future work aims to deposition of a thin oxide material such as TiO_2 on the surface of α-$SnWO_4$ to passivate the surface.

4.4 Experimental Section

All reagents were purchased from Sigma Aldrich and used as received with no further purification. FTO films (Pilkington glass) were washed with ethanol and acetone and sonicated for 15 minutes each. WO_3 was prepared by a known procedure.[16] Sodium tungstate dihydrate, $Na_2WO_4 \bullet 2H_2O$, (0.308 g, 9.34×10^2 mmol) was dissolved in 40 mL deionized water. 3 M HCl (13.34 mL, 4×10^4 mmol) was added dropwise to the stirring solution, which formed a yellow precipitate. Next, ammonium oxalate, $(NH_4)_2C_2O_4$, (0.267 g, 2.15×10^3 mmol) was added and the solution became clear and colorless. An additional 40 mL of deionized water was added, and the solution was stirred for 30 minutes. Then, 11.5 mL aliquots of solution were transferred to 23 mL PTFE liners (Parr Instrument Company). The FTO films were masked off with PTFE tape to a surface area of 1 cm^2 so that deposition onto the FTO area was controlled. The films were placed face down in the liner and sealed in a stainless steel autoclave. The vessels were held at 120 °C for 12 hours with a 10 °C/min ramp rate. These films were either kept as is ($WO_3 \bullet H_2O$, yellow/green in appearance) or annealed in air at 450 °C for 1 hour (monoclinic WO_3, green/white in appearance). A 0.5 M $SnCl_2$ solution was made that had an initial pH of ~1. Next the $WO_3 \bullet H_2O$ or WO_3 films were placed face down in the hydrothermal vessel filled with 14 mL of 0.5 M $SnCl_2$ solution whose pH was 1 or adjusted to 4 or 7 with 7 M NaOH and 3 M HCl. The vessels were sealed in steal autoclaves and heated for 24 hours at 180 °C with a 10 °C/min ramp rate. The films were rinsed with 3 M HCl to remove any tin chloride hydroxide crystals that formed during the

hydrothermal reaction (Figure C.13). In a control experiment WO_3 films were placed face down in the hydrothermal vessel filled with 14 mL of water adjusted to pH 7 with 7 M NaOH. This control experiment was also carried out in 1 M NaCl to keep the ionic strength of chloride constant in the reaction.

X-ray diffraction patterns were recorded on a Bruker D8 Advance diffractometer equipped with a graphite monochromator, a Lynx-Eye detector, and parallel beam optics using Cu-Kα radiation (λ = 1.54184 Å). Patterns were collected using a 0.6 mm incidence slit, with a step size and scan rate of 0.04°/step and 0.5 s/step, respectively. Phases were identified as $WO_3 \bullet H_2O$ (JCPDF 43-0679), WO_3 (JCPDF 72-1465), and $SnWO_4$ (JCPDF 70-1049) using MDI Jade version 5.0. UV-vis spectra were recorded using a Cary 5000 spectrophotometer (Agilent) equipped with an external diffuse reflectance accessory. Spectra were recorded in reflectance mode, and Tauc plots were then generated using the Kubelka-Munk function, $F(R) = (1-R)^2/2R$. Scanning electron microscope images were collected using a FEI Nova Nanolab SEM/FIB with an accelerating voltage of 15 kV.

Photoelectrochemical (PEC) measurements were performed using a custom-built, three-electrode Pyrex glass cell with a quartz viewing window. The cell contained the working thin-film $SnWO_4$ photoelectrode, an Ag/AgCl reference electrode in saturated KCl (+0.20 V *vs*. NHE), and a platinum auxiliary electrode. For water oxidation reactions, the supporting electrolyte used was a 0.1 M potassium phosphate buffer (KP_i) solution at pH 5.00. Electrical contact was made to the FTO substrate by attaching copper wire purchased from Fisher Scientific and using CG Electronics Silver Print II. Electrodes were sealed using Loctite Hysol 1C epoxy. The light source was a Newport-

Oriel 150 W Xe arc lamp fitted with a Newport AM 1.5G filter to simulate incident solar radiation. The lamp power was adjusted to 100 mW/cm^2 using a Newport 1918-R optical power meter equipped with a Newport 818P-015-19 thermopile detector. Voltammetry measurements were performed with a CH Instruments 660C Electrochemical Workstation.

4.5 References

1. Herrero, C.; Lassalle-Kaiser, B.; Leibl, W.; Rutherford, A.W.; Aukauloo, A. Artificial systems related to light driven electron transfer processes in PSII Coord. Chem. Rev. 2008, 252, 456-468.
2. Ren, Y.; Ma, Z.; Bruce, P.G. Ordered mesoporous metal oxides: synthesis and applications Chem. Soc. Rev. 2012, 42, 4909-4927.
3. Shen, G.Z.; Chen, P.-C.; Ryu, K.; Zhou, C.W. Devices and chemical sensing applications of metal oxide nanowires J. Mater. Chem. 2009, 19, 828-839.
4. Fujishima, A.; Honda, K. Electrochemical photolysis of water at a semiconductor electrode Nature 1972, 283, 37-38.
5. Sivula, K.; Zboril, R.; Formal, F.L. Photoelectrochemical water splitting with mesoporous hematite prepared by a solution-based colloidal approach J. Am. Chem. Soc. 2010, 132, 7436-7444.
6. González-Borrero, P.P.; Sato, F.; Medina, A.N. Optical band-gap determination of nanostructured WO3 film Appl. Phys. Lett. 2010, 96, 061909.
7. Berglund, S.P.; Flaherty, D.W.; Hahn, N.T.; Bard, A.J.; Mullins, C.B. Photoelectrochemical oxidation of water using nanostructured $BiVO_4$ films J. Phys. Chem. C 2011, 115, 3794-3802.
8. Yourey, J. E.; Pyper, K. J.; Kurtz, J. B.; Bartlett, B. M. Chemical Stability of $CuWO_4$ for Photoelectrochemical Water Oxidation J. Phys. Chem. C 2013, 117, 8708-8718.
9. Lacomba-Perales, R.; Ruiz-Fuertes, J.; Errandonea, D.; Martínez-García, D.; Segura, A. Optical absorption of divalent metal tungstates: correlation between the band-gap energy and the cation ionic radius Europhys. Lett. 2008 , 83, 37002.
10. Jeitschko, W.; Sleight, A.W. Synthesis, Properties and Crystal Structure of β-$SnWO_4$, Acta Cryst. 1972, B28, 3174-3178.
11. Cho, I.-S.; Kwak, C.H.; Kim, D.W.; Lee, S.; Hong, K.S. Photophysical, Photoelectrochemical, and Photocatalytic Properties of Novel $SnWO_4$ Oxide Semiconductors with Narrow Band Gaps J. Phys. Chem. C 2009, 113, 10647-10653.
12. Dong, H.; Li, Z.; Ding, Z.X. Nanoplates of α- $SnWO_4$ and SnW3O9 Prepared via a Facile Hydrothermal Method and Their Gas-Sensing Property Sensors and Actuators B, 2009, 140, 623-628.
13. Zhu, G.Q.; Que, W.X.; Zhang, J.; Zhong, P. Photocatalytic Activity of $SnWO_4$ and SnW3O9 Nanostructures Prepared by a Surfactant-Assisted Hydrothermal Process Materials Science and Engineering B 2011, 176, 1448-1445.

14. Uma, S.; Singh, J.; Thakral, V. Facile room temperature ion exchange synthesis of Sn2+ incorporated pyrochlore-type oxides and their photocatalytic activities Inorg. Chem. 2009, 48, 11624-11630.
15. Dickens, P.G.; Whittingham, M.S. The tungsten bronzes and related compounds Quart. Rev. Chem. Soc. 1968, 22 30-44.
16. Yang, J.; Li, W.Z.; Li, J.; Sun, D.B.; Chen, Q.Y. Hydrothermal synthesis and photoelectrochemical properties of vertically aligned tungsten trioxide (hydrate) plate-like arrays fabricated directly on FTO substrates J. Mater. Chem. 2012, 22, 17744-17752.

Chapter 5

Photoelectrochemical Oxidation of Primary Amines to Imines using $CuWO_4$ Photoanodes

5.1 Introduction

Green chemistry is defined as "the design of chemical products and processes that reduce or eliminate the use and generation of hazardous substances."[1] The subject of this chapter relates to green chemistry, which are described by 12 key principles. The goals of this project align well with these principles, which I will outline below. The first is *prevention of waste* rather than treatment or cleanup. With the use of $CuWO_4$ external oxidants are no longer needed and therefore prevention of waste is achieved. 2) *Atom economy* is described by maximum incorporation of materials used in the synthetic process to the desired product. Again, we will help to achieve this by eliminating external materials like external oxidants that are not a part of the synthetic product. 3) *Less hazardous chemical syntheses* are attained by the use of nonhazardous and reusable $CuWO_4$ as well as removal of toxic external chemical oxidants. 4) Synthetic organic laboratories will hopefully be able to use $CuWO_4$ and visible light to *design safer chemicals*, which is the fourth principle of green chemistry. 5) The ideal system in which to perform organic oxidations is in water, which will be the end goal of this project to achieve *safer solvents and auxiliaries*. 6) *Design for energy efficiency* is a large reason to use $CuWO_4$ and sunlight because it has a lower environmental and economic impact than

current methods as well as conducted at room temperature and pressure. 7) Since $CuWO_4$ is easily removed from the reaction mixture and reusable it represents green principle number seven, *use of renewable feedstocks*. 8) There may be a possibility of reducing the amount of steps needed for organic reactions using $CuWO_4$ to *reduce derivatives* by selective oxidations at the $CuWO_4$ surface. 9) $CuWO_4$ is also able to perform the reaction *catalytically* as opposed to stoichiometrically. 10) Chemical products should be *designed for degradation*. 11) *Real-time analysis of products and side-products for pollution prevention* of hazardous substances. 12) *Inherently safer chemistry for accident prevention* is achieved when using inert and nontoxic $CuWO_4$.

This chapter focuses on the outlook for metal oxides like those of $CuWO_4$, $Zn_{1-x}Cu_xWO_4$, and $BiVO_4$, and how they may be used for other reactions besides water oxidation. One of the applications $CuWO_4$ could be used for is greener methods and alternatives to oxidation of organic compounds. The environmental impact of many organic transformations relates to 1) use of external oxidants, 2) expensive catalysts and catalytic supports, 3) catalyst lifetimes, and 4) high temperatures. Each problem above is addressed by utilizing metal oxide semiconductor photocatalysts. Specifically, visible light absorbing metal oxides can alleviate the issues by 1) removal of external oxidants utilizing only that of O_2, 2) use of abundant, cheap semiconductor catalysts, 3) durable and reusable metal oxides, and 4) use of sunlight to photochemically drive the reaction.

Designing a catalyst capable of selectively oxidizing an organic substrate, but not over-oxidizing that substrate is a need in the synthetic field. For example, a common chemical oxidant used in organic reactions is potassium permanganate ($KMnO_4$). However, MnO_4^- will always convert a functionalizable organic group all the way to its

most oxidized product. For example, a primary alcohol is oxidized to the carboxylic acid, even when the 2-electron oxidation to the aldehyde is preferred. Cr^{6+} compounds such as H_2CrO_4 and $K_2Cr_2O_7 \cdot H_2SO_4$ can oxidize a primary alcohol all the way to the carboxylic acid as well. However, in non-aqueous solutions, primary alcohols can be oxidized to the aldehyde without going all the way to the carboxylic acid because the Cr intermediate requires hydrolysis to continue the oxidation. In any case, chromates are not ideal as they have a high toxicity level. Therefore, homogeneous catalysts, such as Cu-based catalysts have been implemented using O_2 as an oxidant and TEMPO (TEMPO = 2,2,6,6-tetramethyl-1-piperidinyloxyl).[23] Utility in Cu-based catalysts has improved cost from Ru-based catalysts and others using Au supports. However, the stability and ease with which to recover the catalyst are still issues that need to be addressed with these homogenous catalysts as well as removing external oxidants like TEMPO.

I therefore want to place a specific emphasis on mixed metal oxides for application in catalytic reactions for organic synthesis. Mixed metal oxides or MMOs are classified as two or more metallic ions in differing stoichiometries in combination with oxygen. MMOs are known for their catalytic activity based on the presence of partially filled d-shells and the influence of these partially filled d-shells on the oxide ligand field.[4] The stability and durability of MMOs also makes them favorable due to existing in their most oxidized form, typically. They are also identified as one of the largest groups of industrially important heterogeneous catalysts (Figure 5.1) and have been shown to often out perform their component oxide counterparts in various reactions. For example, Ni-Fe oxides were tested for electrolytic oxygen-evolution activity and the best activities were observed with oxides containing Ni and Fe, together with third metal ion.[5]

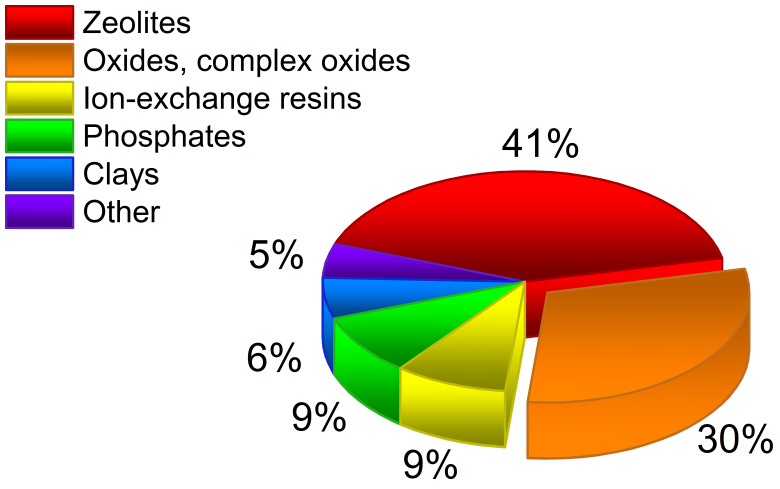

Figure 5.1 Depiction of industrially important heterogeneous catalysts.[2]

This could be due to a higher number of active acidic and basic sites as well as an increase in surface area.[4] Since MMOs have an impressive track record for organic transformations[6], it makes sense to pursue photochemical organic oxidations on materials such as $CuWO_4$, $Zn_{1-x}Cu_xWO_4$, and $BiVO_4$ and other possible MMO combination of these semiconductors.

5.2 Oxidation of Benzylamine on $CuWO_4$ and Outlook

Specifically as an example and outlook, I will focus on the oxidation of a primary amine group to its respective imine under illumination using a $CuWO_4$ electrode. Compared to the biomimetic or enzymatic reactions of amine oxidation, industrial processes for these reactions require external oxidants and often reactions temperatures over 100 °C. Amine oxidations are important from the standpoint of not only improving synthetic organic processes, but they also have biological implications.[7] A metal oxide photocatalyst to draw inspiration from is TiO_2, which has been studied for a wide range of applications especially within the field of photocatalysis. It has been exploited for alcohol and amine oxidation by Zhao et al. who utilized UV light absorption and O_2 as an external oxidant involved in the reaction.[8] The importance of O_2 in the catalytic cycle

was realized as the mechanism goes through a benzaldehyde intermediate for both alcohol and amine oxidation.[910] However, the drawbacks of using TiO_2 for organic oxidations are that it over-oxidizes the substrate due to the high energy 3 eV holes generated in the valence band, and it has a large band gap (E_g = 3.0-3.2 eV), which results only in a UV response (Figure 5.2).[11] Another metal oxide photocatalyst that has been used for selective amine oxidation is Nb_2O_5, in which the band gap is 3.2-3.4 eV (Figure 5.2), yet there are claims to use visible light up to 450 nm for alcohol and amine oxidation.[12] For both alcohol and amine oxidation, the claim is that once the alcohol or amine species binds, it represents an "*in situ* doping" where an electron is excited from this new donor level and the reaction is propelled forward under this new visible light excitation. For this reason, the authors claim the selectivity increases over Nb_2O_5 for amine oxidation (98%) over that of TiO_2 and ZnO (89% and 94%). However, the same experiment was completed on TiO_2 to address any

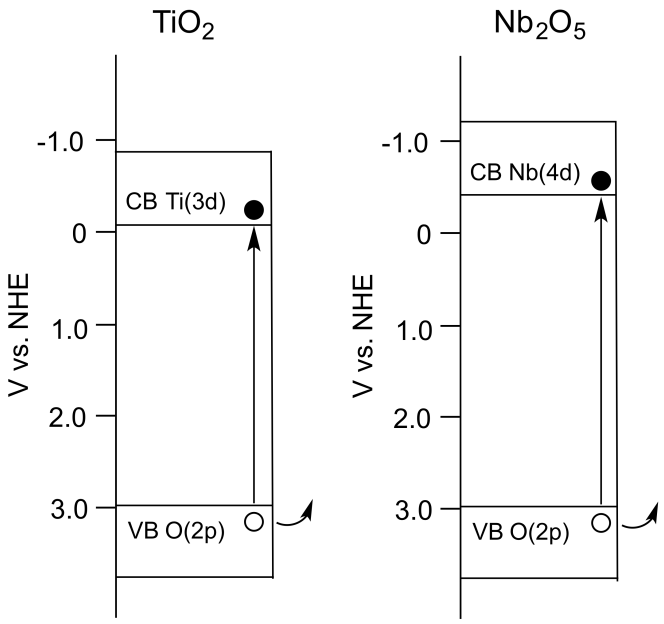

Figure 5.2 Band structures of n-type TiO_2 and Nb_2O_5 showing e^-/h^+ separation.

possible visible light absorption after adsorption of the starting material onto TiO_2. The same response was observed: absorption was extended further into the visible region, with absorption beginning at ~450 nm just like that of Nb_2O_5.[9] This result provides evidence that *in situ* doping alone is not the only contributor to the difference in selectivity observed when comparing different catalyst materials such as Nb_2O_5 and TiO_2. However, for the oxidation of benzylamine to N-benzylidenebenzylamine on TiO_2 the

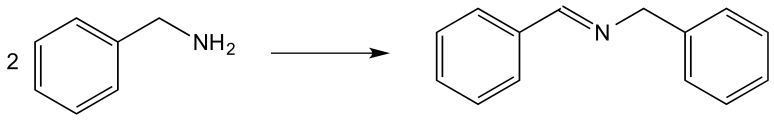

Scheme 5.1 Oxidation of benzylamine to benzylidenebenzylamine.

authors ran the reaction at $\lambda > 420$ nm, which excludes excitation of TiO_2. Conversion to desired product was still observed and the selectivity, contingent upon the TiO_2 catalyst used, was from 94-98%. This yield seems to suggest that valence band holes are not directly involved in the oxidation process, which eliminates reaction pathways using high energy radicals such as •OH and O_2•$^-$/HO_2• caused by valence band holes or reduction of O_2 by conduction band electrons. However, in later published results the same authors used $\lambda > 300$ nm (300 nm = 3.54 eV) or $\lambda > 350$ nm (350 nm = 4.13 eV) for experimental conditions, which includes the 3 eV excitation region for TiO_2.[10,11]

In using the heterogeneous catalyst $CuWO_4$, we will attempt to address some of the issues we identified for organic transformation reactions. As discussed previously, $CuWO_4$ has a raised valence band (2.7 eV) compared to that of TiO_2 and Nb_2O_5 (3.0-3.4 eV) due to the Cu(3d) orbital contribution; therefore it has a smaller oxidizing power from valence band holes. Also, its band gap energy is smaller, 2.3 – 2.4 eV allowing us to use visible light. For this reason, protection against overoxidation as well as an increase

in selectivity may be possible with $CuWO_4$. Not only does it have a raised VB, but the mid-gap states may also contribute to the reaction mechanism.

As a test reaction on $CuWO_4$, benzylamine was chosen to carry out the reaction in Scheme 5.1. The reaction was carried out on a film electrode of $CuWO_4$ made by sol-gel processing. An excess of benzylamine starting material was added to the reaction in order to prevent any diffusion limitation. The reaction was performed in acetonitrile (at 1 atm) with tetrabutylammonium hexafluorophophate ($TBAPF_6$) as supporting electrolyte. Linear sweep voltammetry was performed on the electrode in the dark and light using a 150 Xe lamp fitted with a blue cut-on filter from 300-600 nm and focuser producing 450 mW/cm^2 of light onto the electrode. Figure 5.3 represents dark, illuminated, and chopped-light linear sweep voltammograms recorded during benzylamine oxidation.

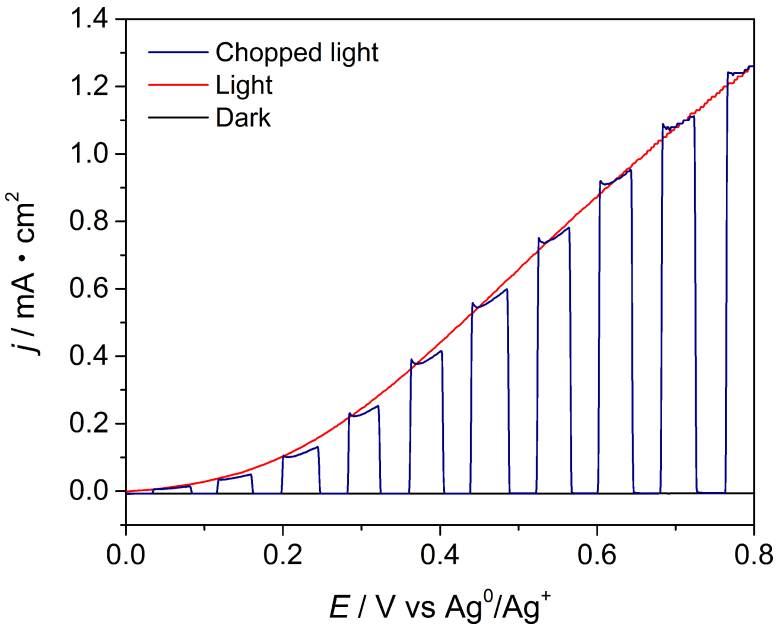

Figure 5.3 Dark (black), light (red), and chopped light (navy) linear sweep voltammograms of benzylamine oxidation on $CuWO_4$

From the linear sweep voltammogram, there is oxidation that is taking place at the surface of the electrode. There is a small amount of transient photocurrent observed in the

chopped light linear sweep voltammogram, which points to a lack of recombination at the surface. To determine the oxidation product, bulk electrolysis was performed on an electrode poised at 0.7 V vs Ag^0/Ag^+ (Figure 5.4), in which 3.5 *C* of charge was passed in order to produce enough product for gas chromatography (GC) detection. The bulk electrolysis has an initial spike in current that decreases over the span of ~15 minutes, after which it remains constant for the remainder of the experiment. This initial decrease could be due to oxidation of a small amount of water since the acetonitrile used is not dried. The

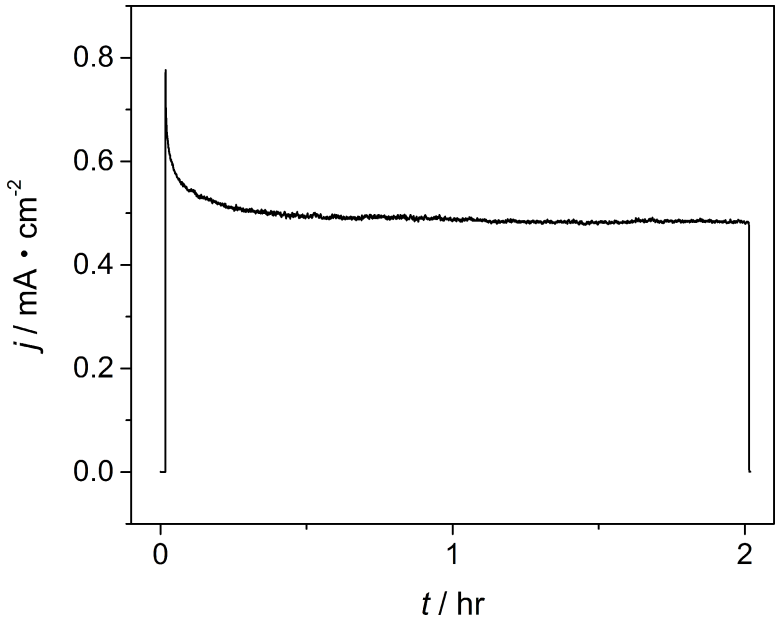

Figure 5.4 Bulk electrolysis of benzylamine oxidation at the surface of a $CuWO_4$ electrode at 0.7 V vs Ag^0/Ag^+ in 0.5 M benzylamine solution with 0.1 M $TBAPF_6$ in acetonitrile.

reaction is carried out at ambient atmospheric conditions with acetonitrile exposed to air and kept at room temperature and pressure. One of the positive aspects of these types of reactions is that solvents do not have to be dry and air free in order to carry out the synthetic process at the metal oxide surface. This was experimentally determined in

previous results using TiO_2 and as stated previously, exposure to air or O_2 is necessary to propel the reaction forward using O_2 as an external oxidant. Therefore, all of the reactions were run in similar conditions as Zhao et al. as a test system like that of TiO_2.[11] However, since the reaction is being carried out electrochemically on a $CuWO_4$ photoanode the reaction conditions were adapted for photoelectrochemistry where an electrolyte was added for solution conductivity and a sacrificial oxidant ($[Fe(CN)_6]^{3-}$) was added in the counter electrode compartment. The required addition of high concentration electrolyte species that must be removed before a GC test required a work-up to remove the electrolyte, yet solubilize the product (n-benzylidenebenzylamine and similar products) and internal standard (bromobenzene). Accordingly, after the reaction was finished, the work-up for GC analysis is: 1) rotovapping down to crude oil by removing the acetonitrile; 2) adding ethyl ether to crash out $TBAPF_6$; 3) filtering through Celite; 4) rotovapping down to crude oil; 5) dissolving in $CHCl_3$ to run the GC trace. The benzylidenebenzylamine product and bromobenzene internal standard are both soluble in the solvents chosen throughout the work-up. The GC shows production of benzylidenebenzylamine in yields of 88-94%. A representative gas chromatogram is shown in Figure 5.5.

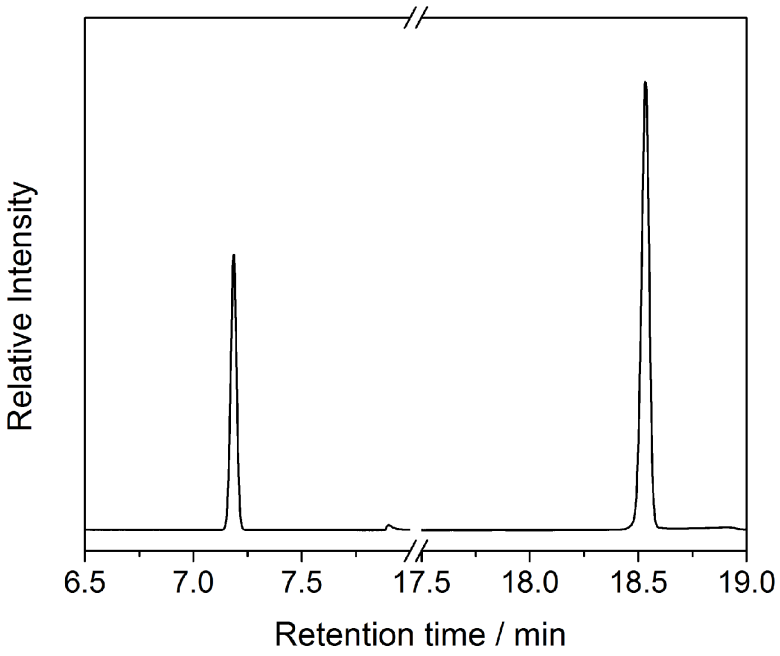

Figure 5.5 Gas chromatogram of benzylidenebenzylamine (retention time 18.55) and bromobenzene internal standard (retention time 7.19).

When carrying out this reaction with $CuWO_4$ powder, since no electrolyte is required, the work-up becomes greatly simplified with less potential product loss. Powdered catalysts also have the advantage of many surface catalytic sites to increase product formation over time compared to a thin-film. On the other hand, when performing the reaction at an electrode surface, one is able to track the charge passed and compare to the moles of product produced, which helps account for what may be taking place at the $CuWO_4$ surface. The reaction in Scheme 5.1 was also performed with $CuWO_4$ powder synthesized by a co-precipitation reaction and further treated hydrothermally.[14] In this experiment, the reaction conditions were mimicked to that of the TiO_2 powder reactions performed by Zhao *et al*. The reaction conditions are 10 mg of $CuWO_4$ powder, bromobenzene as the internal standard, and 0.1 mmol of benzylamine in 2 mL of acetonitrile. The illumination conditions were held the same as with the electrode at 450 mW/cm^2 measured lamp power with a blue cut-on filter (300-600 nm)

and focuser in a single quartz cell. The illumination setup of TiO_2 could not necessarily be mimicked due to the vague setup description (100 W Hg lamp cutting off light below 300 nm).[11] Unfortunately, this lack of experimental detail is common when comparing across reaction conditions in the literature for photochemical reaction studies. The reaction was carried out overnight, and we find that all of the starting material is converted to benzylidenebenzylamine. For this reaction, the solvent is removed by rotovapping and the crude oil is dissolved in chloroform to run GC. We have shown that simple primary amine (benzylamine) oxidation is possible on $CuWO_4$ electrodes as well as $CuWO_4$ powder.

The mechanistic pathway of amine oxidation on $CuWO_4$ now requires further investigation, and represents the most pressing direction for new exploration. To continue this project, an expanded substrate scope with record yields and selectivities are required. $CuWO_4$ may be a unique case (compared to that of TiO_2) since it has a unique electronic structure as discussed in depth in Chapter 3 as well as a mixed metal structure. This thesis work demonstrates that water oxidation on $CuWO_4$ proceeds through a mid-gap state. Therefore a question to ponder is whether or not amine oxidation would follow the same mechanistic pathway or interact directly with VB holes (if VB holes are the proponent of the oxidation reaction in the first place).

This brings about a discussion of expanding the substrate scope to alcohol oxidation on $CuWO_4$ as well. This leads us to again discuss mechanistic pathways in terms of a mid-gap Cu(3d) state involvement. A photocurrent doubling effect was observed at the surface of $CuWO_4$ in a solution of 10% methanol in 0.1 M Na_2SO_4 (pH 5.6) for a film synthesized by electrodeposition by Dr. Joseph Yourey.[13] Therefore, we

know that oxidation of an alcohol group does take place at the $CuWO_4$ surface, although we have not yet quantified the products of this reaction. Performing methanol oxidation on TiO_2 produces a product distribution of methylformate and carbon dioxide.[14] In preliminary work, I have also performed EIS on $CuWO_4$ in a 10% methanol solution in 0.5 M KB_i and 0.2 M KCl at pH 7. The photocurrent production is shown in the chopped light linear sweep voltammogram in Figure 5.6 (red trace) and has a slightly earlier photocurrent onset but does not

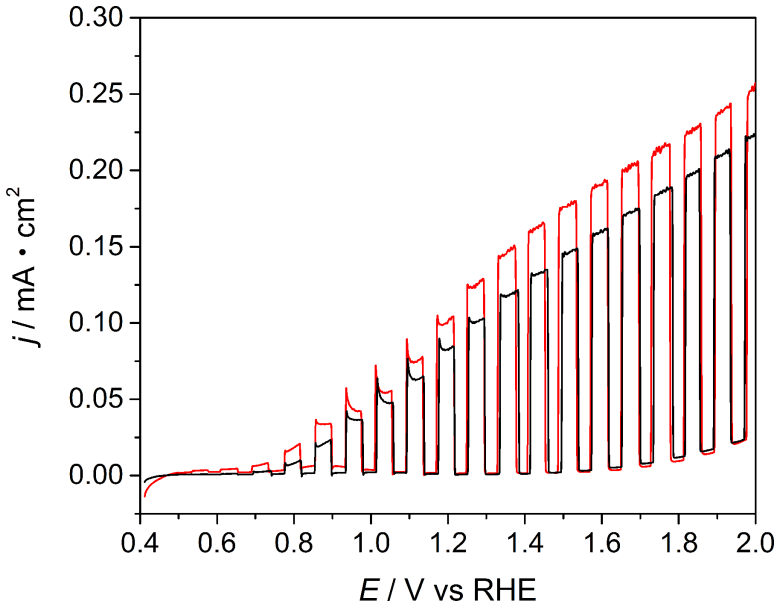

Figure 5.6 Chopped light linear sweep voltammogram of a $CuWO_4$ electrode in 0.5 M KB_i, 0.2 KCl pH 7 (black) with 10% methanol (red) at 100 mW/cm^2 with an AM1.5 filter.

display a significant amount of increased photocurrent compared to the same conditions at pH 7 without methanol (black trace in Figure 5.6) Performing EIS on $CuWO_4$ with 10% methanol at pH 7 also displays a depressed semicircle similar to what is observed with water oxidation on $CuWO_4$. Further experimental evidence and data fitting to the equivalent circuit in Figure 3.1b confirm multiple charge transfer events take place in the presence of methanol. Also, the transient photocurrent at the onset region is observed in

the same potential region as that of water oxidation on $CuWO_4$. Fermi level pinning is observed from 0.7 to 1.05 V vs RHE in the Mott Schottky of $CuWO_4$ in Figure 5.7 in KB_i with 10% methanol. The pinning corresponds to the onset of photocurrent in the LSV in Figure 5.6. Therefore, the mechanism of methanol oxidation is likely similar to that of water oxidation at the surface of $CuWO_4$.

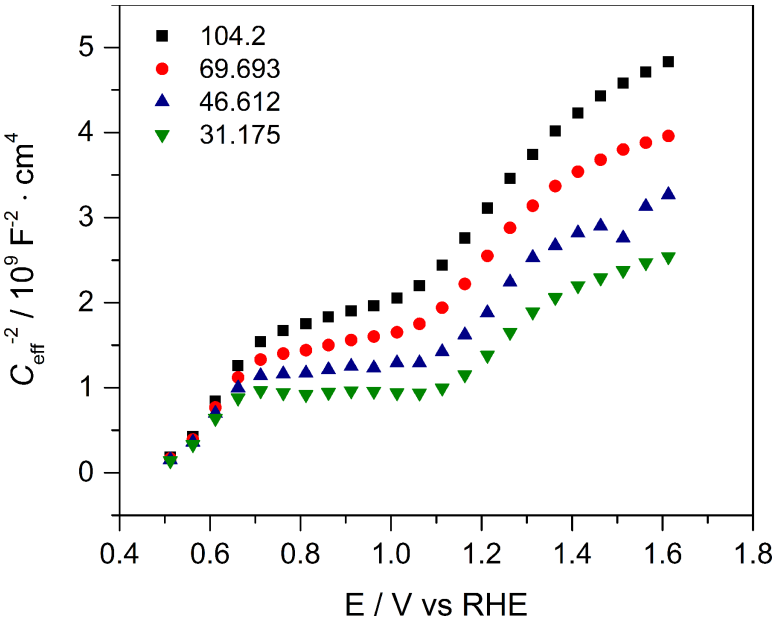

Figure 5.7 Mott Schottky analysis of a $CuWO_4$ electrode in 0.5 M KB_i, 0.2 KCl pH 7 with 10% methanol at 100 mW/cm^2 with an AM1.5 filter.

There may be a possibility for selective oxidation of alcohol groups through a similar mechanistic pathway to that of water oxidation (oxidation through Cu(3d) states within the gap) while an amine may react instead directly with valence band holes (Figure 5.8). Even if amine oxidation does in fact still take place via oxidation through use of Cu(3d) states in the gap if there is a different kinetic reaction mechanism selectivity may still be imparted. With a large overpotential for photoelectrochemical

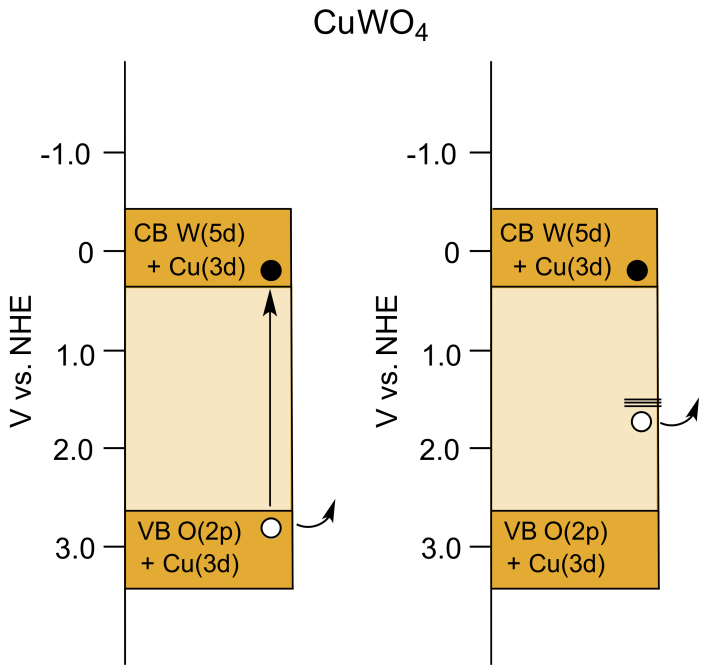

Figure 5.8 Band structure of $CuWO_4$ with e^-/h^+ separation and hole location in the VB vs hole location at states within the gap.

oxidation of water due to this mid-gap state interaction it may also be possible to control selectivity based on applied potential for the same mechanistic reason described above. By operation at a lower potential where there are slow kinetics to oxidize an alcohol group, selectivity in that case may be high for primary amine oxidation.

5.3 Experimental Section

All reagents and solvents used were obtained commercially. Amines were and purified by distillation with zinc dust under reduced pressure. Gas chromatography (GC) measurements were performed with a Thermo Scientific Trace 1300 Gas Chromatograph equipped with an FID detector and a TraceGOLD TG-5MS Amine GC column using N_2 as a carrier gas. Conditions during injection are as follows: 1 μL of solution was injected and the injector temperature was 180 °C operating in splitless with a split flow of 60 mL/min, split ration of 30, and splitless time of 0.20 min. The purge flow was set at 3.000

mL/min. with a ramp from 40-300 °C with 10 per min rate, held for 0.5 minutes then 2 minute hold time at 250 °C. The detector temperature was 325 °C with airflow of 350.0 mL/min and a makeup gas flow of 40.0 mL/min. Photocatalytic reactions were carried out in a double-sided cell with a quartz window. The working electrode side consisted of a Ag^0/Ag^+ or $Ag/AgNO_3$ reference electrode and the working electrode, which is a $CuWO_4$ electrode. The $CuWO_4$ electrode was produced by sol-gel processing from heating a solution of copper(II) nitrate trihydrate and ammonium metatungstate in a 12:1 ethylene glycol to water mixture. The sol was spin-coated onto an FTO substrate and annealed at 550 °C for 1 hour to form crystalline $CuWO_4$ (see reference 15). $CuWO_4$ powder was produced through a coprecipitation reaction as described in reference 16. A 250 mL solution of 0.04 M $Cu(NO_3)_2 \bullet H_2O$ (10 mmol) was adjusted to pH 5.0 using 1 M NaOH and then heated in an oil bath at 60 °C. A 250 mL solution of 0.04 M $Na_2WO_4 \bullet 2H_2O$ (10 mmol) was slowly added dropwise to the copper nitrate solution. As precipitate formed in the flask the solution became cloudy and formed a yellow/green precipitate. The solution was then slowly heated to 90 °C and heated for 3 hours. The precipitate was collected and washed with water to remove any excess ions and then dried overnight at 60 °C. The precipitate was annealed at 500 °C for 3 hours. Pure phase was identified as $CuWO_4$ (JCPDF 70-1732) using MDI Jade version 5.0.

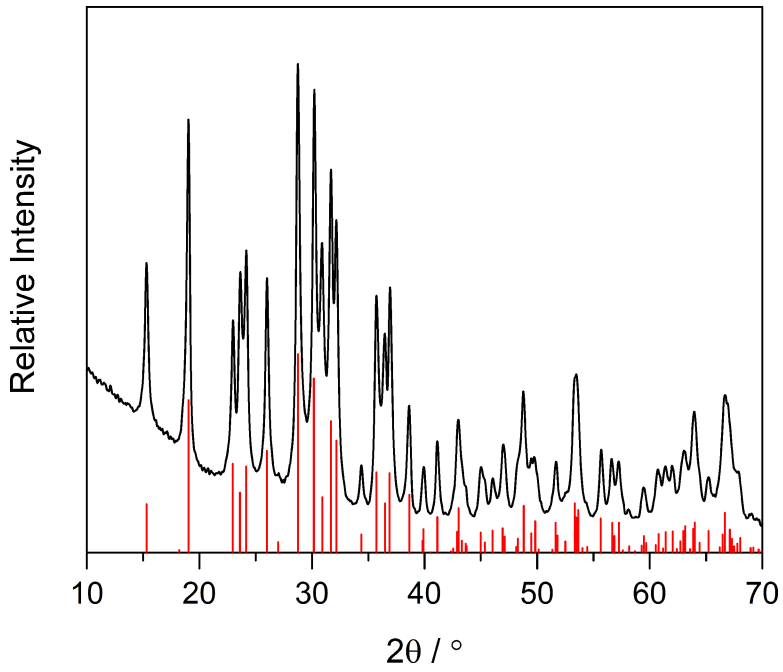

Figure 5.9 X-ray Diffraction of pure $CuWO_4$ powder (black) synthesized by coprecipitation and annealed at 500 °C. Indexed peaks are represented by the red vertical lines.

The film was contacted to a tin-coated copper wire with silver print paint and made into an electrode using glass tubing and 1Hysol epoxy. The counter electrode compartment housed a platinum mesh that was separated from the working and reference electrode by a fine glass frit. The solvent used was acetonitrile with 0.1 M tetrabutlyammonium hexafluorophosphate ($TBAPF_6$). In the working electrode compartment was 0.5 M amine (3 mmol benzylamine) and 0.016 M internal standard (0.095 mmol bromobenzene) in 6 mL of acetonitrile. In the counter electrode compartment was added .018 M $FeCl_3$ (0.062 mmol) as a sacrificial reductant. Voltammetry was performed with a CH Instruments 660C Electrochemical Workstation. Dark, light, and chopped light linear sweep voltammetry were taken under the conditions described above from 0.0 – 0.8 V *vs* Ag^0/Ag^+. Bulk electrolysis was performed under illumination at 0.7 V *vs* Ag^0/Ag^+. The light source was a Newport-Oriel 150 W Xe arc

lamp fitted with a blue cuton filter from 300-600 nm so as to prevent substrate excitation at wavelengths below 300 nm as well as a focuser. The power was measured at 450 mW/cm^2 using an Newport 1918-R optical power meter equipped with a Newport 818P-015-19 thermopile detector. A 1 cm^2 area was irradiated through the quartz window in all cases. The reaction was open to the air by a needle in a septum at the open port on the working electrode side.

5.4 References

1. Anastas, P.T., Warner, J.C. Green Chemistry: Theory and Practice. Oxford University Press: New York, 1998, p. 30.
2. Hoover, J.M.; Stahl, S.S. Highly Practical Copper(I)/TEMPO Catalyst System for Chemoselective Aerobic Oxidation of Primary Alcohols J. Am. Chem. Soc. 2011 133, 16901-16910.
3. Hoover, J. M.; Ryland, B. L.; Stahl S. S.; Copper/TEMPO-Catalyzed Aerobic Alcohol Oxidation: Mechanistic Assessment of Different Catalyst Systems ACS Catal. 2013, 3, 2599-2605.
4. Gawande, M. B.; Pandey, R. K.; Jayaram, R. V. Role of Mixed Metal Oxides in Catalysis Science—Versatile Applications in Organic Synthesis Catal. Sci. Technol. 2012, 2, 1113-1125.
5. Gerken, J. B.; Shaner, S. E.; Masse, R. C.; Porubsky, N. J.; Stahl, S. S. A Survey of Diverse Earth Abundant Oxygen Evolution Electrocatalyst Showing Enhanced Activity from Ni-Fe Oxides Containing a Third Metal Energ Environ. Sci. 2014, 7, 2376-2382.
6. Tanabe, K.; Holderich, W. F. Industrial Application of Solid Acid-Base Catalysts Appl. Catal., A, 1999, 181, 399-434.
7. Murahashi, S-I. Synthetic Aspects of Metal-Catalyzed Oxidations of Amines and Related Reactions Angew. Chem. Int. Ed. Engl. 1995, 34, 2443-2465.
8. Lang, X.; Ma, W.; Chen, C.; Ji, H.; Zhao, J. Selective Aerobic Oxidation Mediated by TiO2 Photocatalysis Accounts Chem. Res. 2013, 47, 355-363.
9. Lang, X.; Ma, W.; Zhao, Y.; Chen, C.; Ji, H.; Zhao, J. Visibe-Light-Induced Selective Photocatalytic Aerobic Oxidation of Amines into Imines on TiO2 Chem. Eur. J. 2012, 18, 2624-2631.
10. Zhang, M.; Wang, Q.; Chen, C.; Zang, L.; Ma, W.; Zhao, J. Oxygen Atom Transfer in the Photocatalytic Oxidation of Alcohols by TiO2: Oxygen Isotope Studies Angew. Chem. Int. Ed. 2009, 48, 6081-6084.
11. Li, N.; Lang, X.; Ma, W.; Ji, H.; Chen, C.; Zhao, J. Selective Aerobic Oxidation of Amines to Imines by TiO2 Photocatalysis in Water Chem. Commun. 2013, 49, 5034-5036.

12. Furukawa, S.; Ohno, Y.; Shishido, T.; Teramura, K.; Tanaka, T. Selective Amine Oxidation Using Nb2O5 Photocatalyst and O2 ACS Catal. 2011, 1, 1150-1153.
13. Yourey, J.E.; Bartlett, B.M. Electrochemical Deposition and Photoelectrochemistry of $CuWO_4$ a Promising Photoanode for Water Oxidation J. Mater. Chem. 2011, 21, 7651.
14. El-Roz, M.; Bazin, P.; Daturi, M.; Thibault-Starzyk, F. On the Mechanism of Methanol Photooxidation to Methylformate and Carbon Dioxide on TiO2: An Operando-FTIR Study Phys. Chem. Chem. Phys. 2015, 17, 11277.
15. Yourey, J. E.; Pyper, K. J.; Kurtz, J. B.; Bartlett, B. M. Chemical Stability of $CuWO_4$ for Photoelectrochemical Water Oxidation J. Phys. Chem. C 2013, 117, 8708-8718.
16. Chen, H.; Leng, W.; Xu, Y. Enhanced Visible-Light Photoactivity of $CuWO_4$ through a Surface-Deposited CuO *J. Phys. Chem. C.* **2014**, *118*, 9982-9989.

Appendix A

Supporting data for Chapter 2

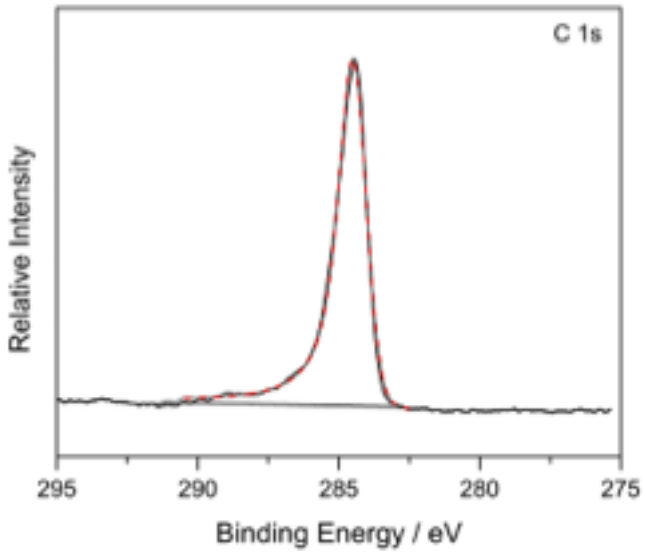

Figure A.1 X-ray photoelectron spectrum of GR deposited onto FTO displaying the C 1s peak at 284.5 eV.

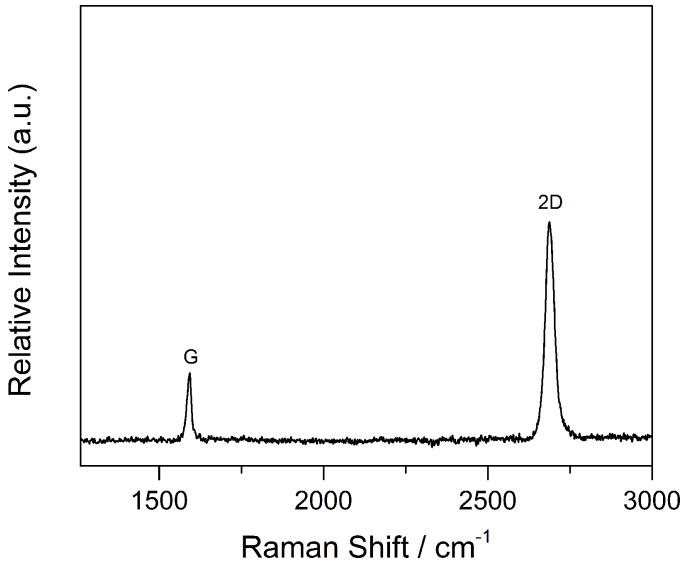

Figure A.2 Raman spectrum of GR on FTO with a laser excitation of 514 nm.

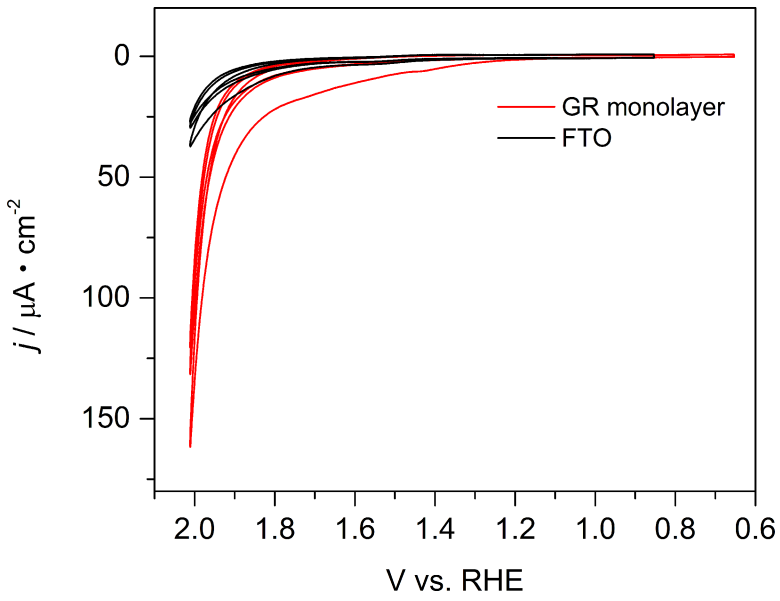

Figure A.3 Cyclic voltammogram of FTO|GR in 0.1 M KP_i, pH 5 at 20 mV/s.

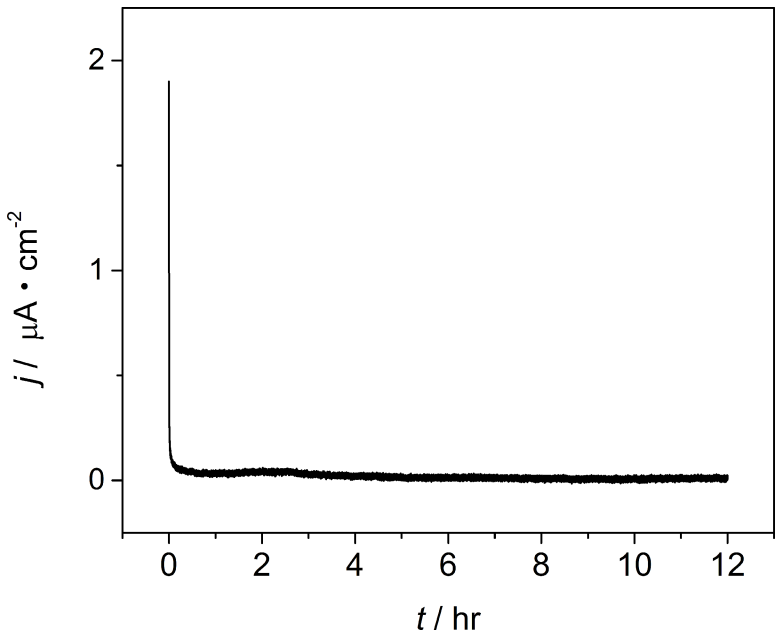

Figure A.4 Bulk electrolysis of FTO|GR at 1.23 V vs. RHE in 0.1 M KP_i, pH 5 solution.

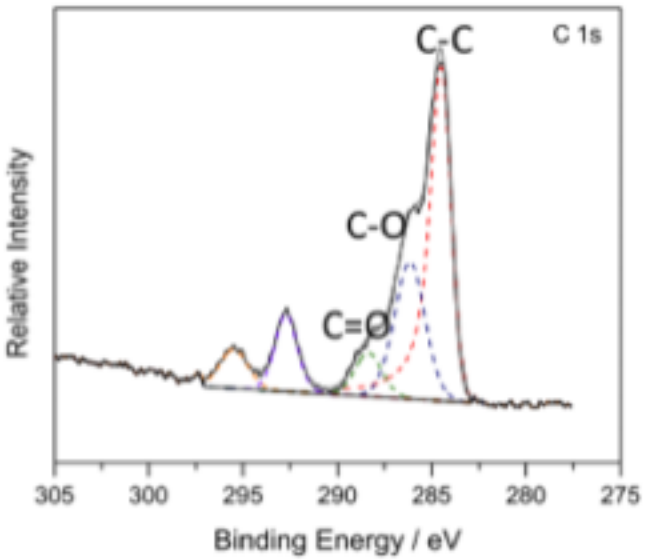

Figure A.5 XPS after GR oxidation by bulk electrolysis at 0.618 V vs. Ag/AgCl for 12 hours.

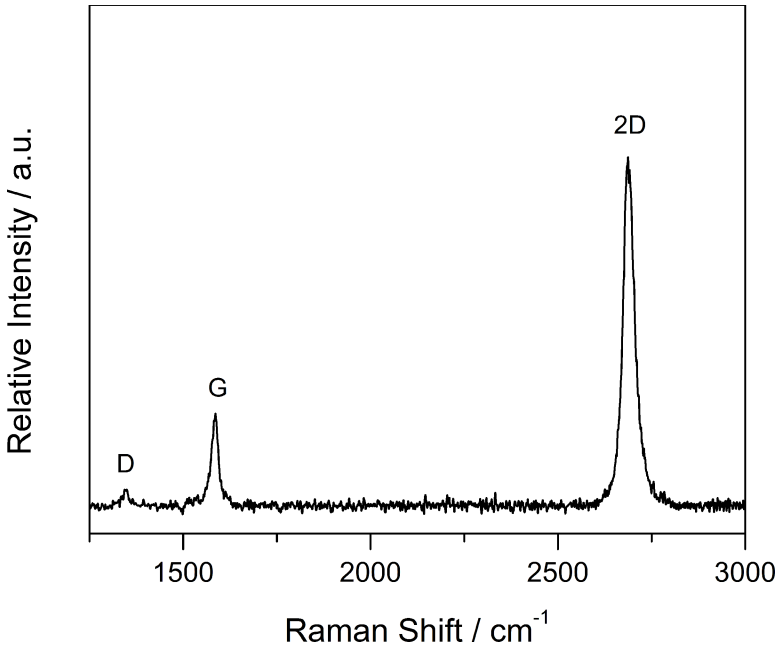

Figure A.6 Raman spectrum taken after cyclic voltammogram from 0.2 to 1.4 V vs. Ag/AgCl under illumination in 0.1 M KP_i, pH 5 at a sweep rate of 20 mV/s.

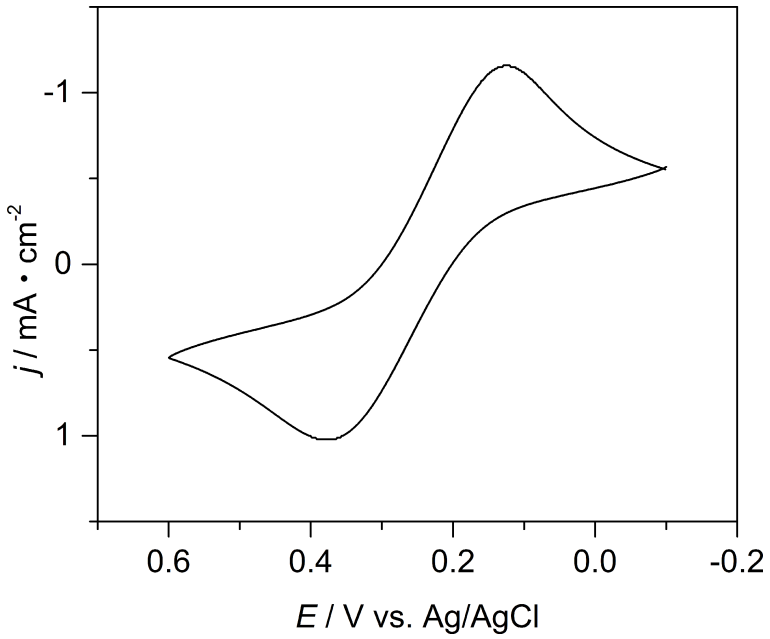

Figure A.7 Cyclic voltammogram to determine the $E_{1/2}$ of the $Fe(CN)_6^{3-/4-}$ reaction in an equimolar 10 mM $Fe(CN)_6^{3-/4-}$ solution.

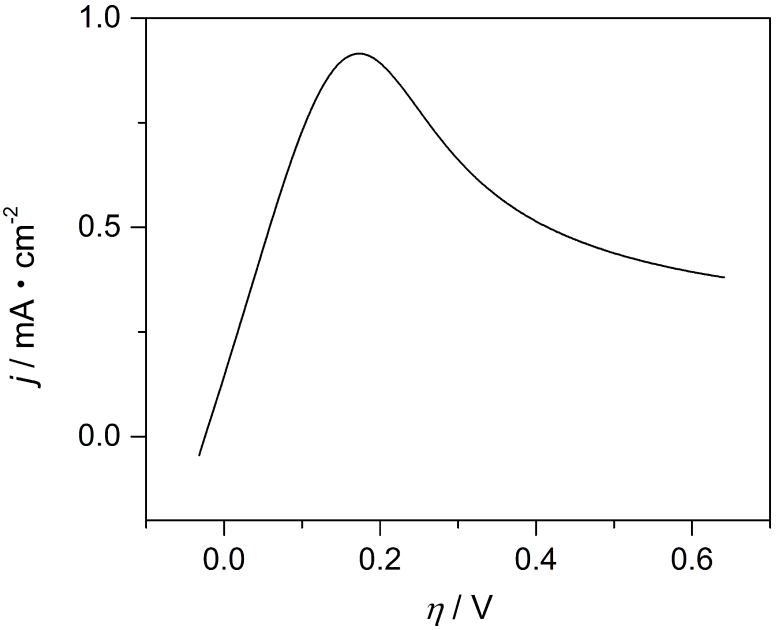

Figure A.8 Overpotential vs current density from a linear sweep voltammogram of FTO in 10 mM solution of $Fe(CN)_6^{3-/4-}$ and 0.1 M KP_i.

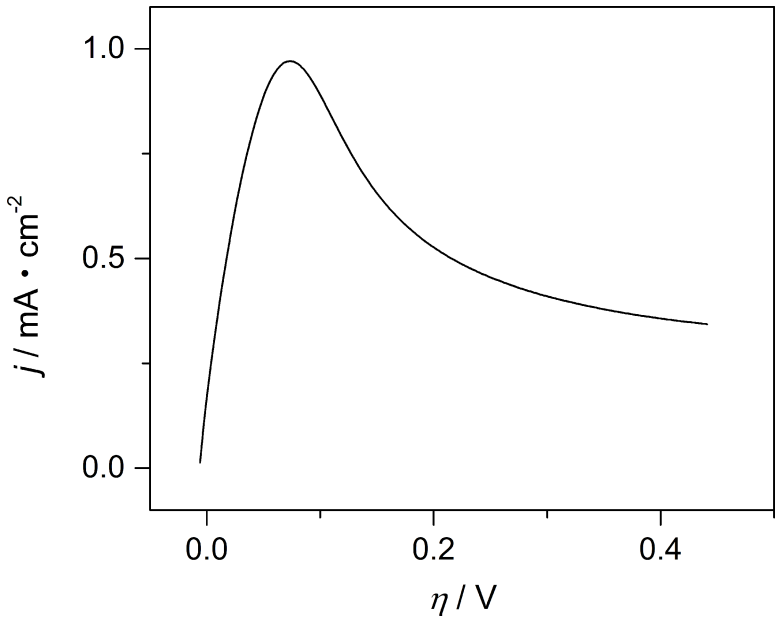

Figure A.9 Overpotential vs current density from a linear sweep voltammogram of FTO|GR in 10 mM solution of $Fe(CN)_6^{3-/4-}$ and 0.1 M KP_i.

Table A.1. R_{ct} values calculated from the negative reciprocal of the slope of the LSV curve shown in Figures S8 and S9 compared to R_{ct} values obtained from EIS.

	Slope	**EIS R_{ct}, Ω**	**LSV R_{ct}, Ω**
FTO	-0.00602	~105	~160
GR	-0.02452	~20	~40

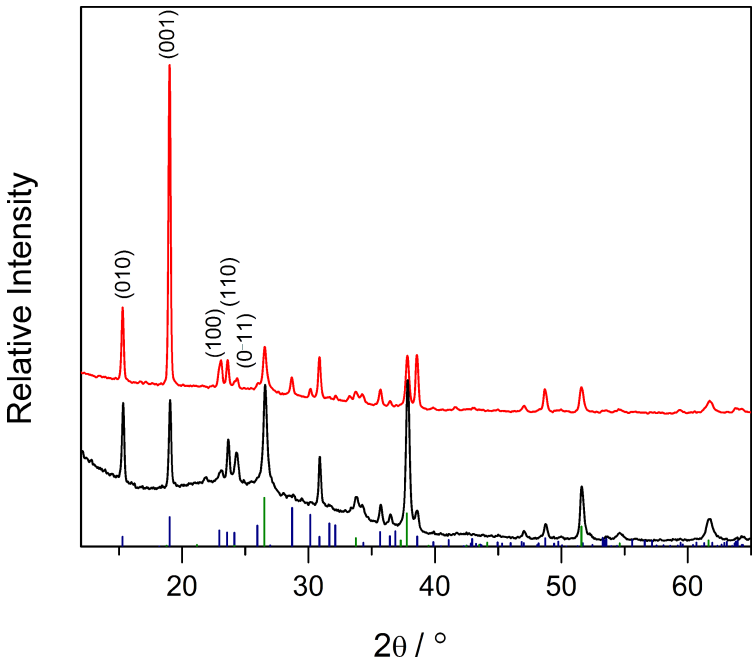

Figure A.10 X-ray diffraction patterns of FTO|GR|$CuWO_4$ at 600 °C, 20 minute growth (black) and 60 minute growth (red). FTO peaks are represented by the green vertical lines and $CuWO_4$ is represented by the navy vertical lines.

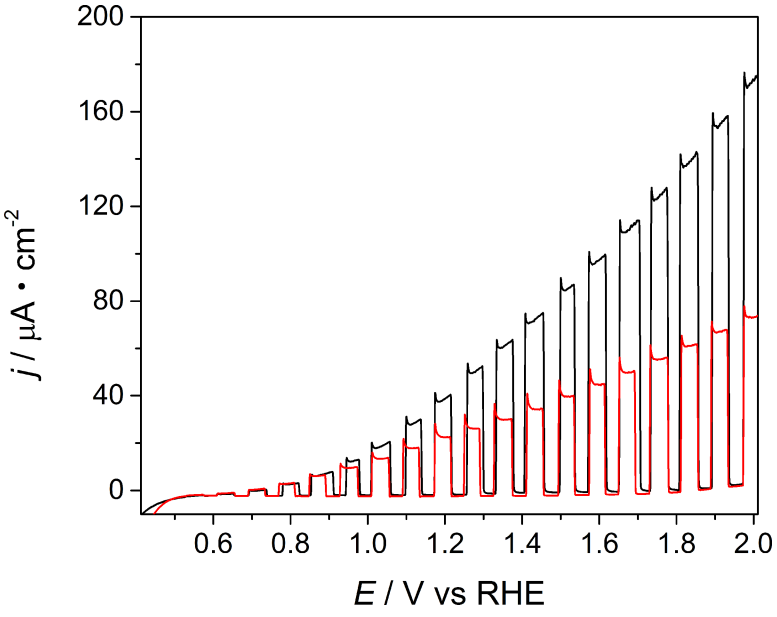

Figure A.11 Chopped light linear sweep voltammogram of the FTO|$CuWO_4$ electrode (black) and FTO|GR|$CuWO_4$ (red) in 0.1 M KP_i, pH 5 at 500 mW/cm^2.

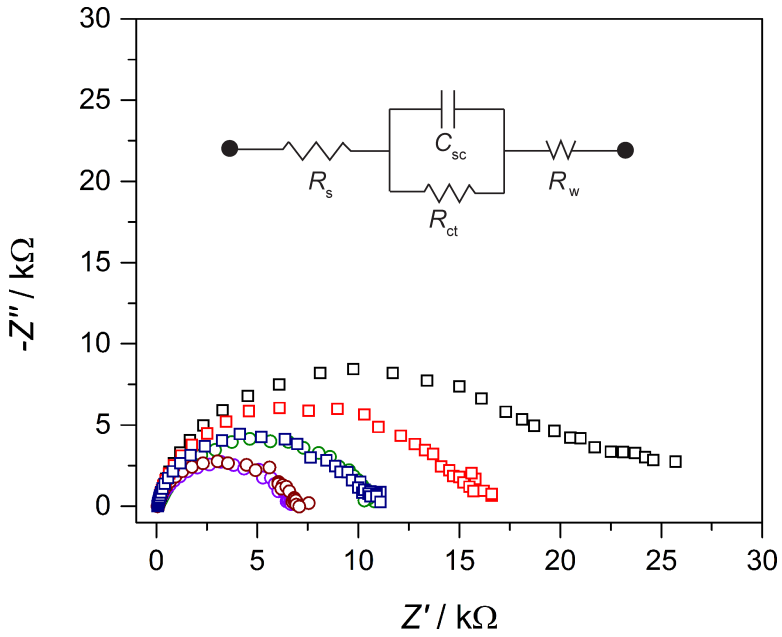

Figure A.12 Nyquist plot of the resistance to water oxidation on FTO|$CuWO_4$ and FTO|GR|$CuWO_4$ under AM1.5 G, 5-sun illumination (500 mW/cm^2) in 0.1 M KP_i, pH 5 solution. The inset shows the equivalent circuit with which the data was fit.

Appendix B
Supporting data for Chapter 3

Justification for use of a CPE to fit EIS data under illumination

The capacitance of C_{sc} and C_{mg} were modeled with a constant phase element (CPE) to fit the data. The CPE describes our system in the way of frequency dispersion of a 2-D distribution of impedance across the electrode surface, characterized by surface heterogeneities, grain boundaries and differing exposed crystal faces[1], representative of our $CuWO_4$ photoanodes. In order to assume this *RC* behavior containing a CPE, we have referred to the Bode plots. The asymptote of the log *f vs.* total Z Bode plot, at high frequencies will trend toward R_e (solution resistance) and the magnitude at low frequency will trend toward $R_{ct} + R_e$ (charge transfer resistance + solution resistance). We do, in fact, confirm this is true of our system. Additionally, in the Bode plot of log *f vs.* phase angle, the phase angle should approach zero at low frequencies, which indicates that the current and potential are in phase, and the phase angle should also approach zero at high frequencies because of the influence of the solution resistance, which our results also validate.[2]

To calculate the capacitance, the CPE component was fit with a CPE-P and CPT-T component, we use the equation: $C_{\text{eff}} = \left[Q\left(\frac{1}{R_e} + \frac{1}{R_t}\right)^{(\alpha-1)}\right]^{1/\alpha}$ where CPE-P represents α and CPE-T = Q, R_e = solution resistance, and R_t = charge transfer resistance.

Table B.1 Table of fitting values of CPE-P, and CPE-T values for the water oxidation reaction on $CuWO_4$ under 100 mW/cm^2 AM1.5G illumination 0.5 M KB_i, 0.2 KCl buffer at pH 7.00.

E **/ V *vs* Ag/AgCl, pH 7**	***E*** **/ V *vs* RHE**	C_{sc}, CPE-T / 10^{-5}	C_{sc}, CPE-P	C_{mg}, CPE-T / 10^{-5}	C_{mg},CPE-P
0.00	**0.61**	1.53	0.74998	0.932	1.075
0.05	**0.66**	1.01	0.7412	0.709	1.073
0.10	**0.71**	1.35	0.87743	0.214	1.057
0.15	**0.76**	1.49	0.89233	0.138	1.029
0.20	**0.81**	1.77	0.86728	0.304	1.025
0.25	**0.86**	2.04	0.81339	1.06	0.97187
0.30	**0.91**	1.51	0.83778	3.51	0.89206
0.35	**0.96**	1.19	0.86127	7.16	0.8504
0.40	**1.01**	1.03	0.87461	11.896	0.80441
0.45	**1.06**	0.970	0.87888	19.12	0.80344
0.50	**1.11**	0.919	0.88207	40.322	0.76534
0.55	**1.16**	0.869	0.88691		
0.60	**1.21**	0.783	0.90085		
0.65	**1.26**	0.798	0.88912		
0.70	**1.31**	0.751	0.89302		
0.75	**1.36**	0.656	0.90632		
0.80	**1.41**	0.590	0.91499		

Table B.2 Table of fit values for C_{sc}, C_{mg}, R_{trap} and $R_{ct,mg}$ under 100 mW/cm^2 AM1.5G illumination 0.5 M KB$_i$, 0.2 KCl buffer at pH 7.00 with calculated capacitances.

E **/ V *vs* Ag/AgCl, pH 7**	***E*** **/ V *vs* RHE**	R_s / Ω cm^2	C_{sc}, calcd / F cm^{-2}	R_{trap} / Ω cm^2
0.00	**0.61**	42.06	3.27×10^{-5}	~0
0.05	**0.66**	42.66	3.09×10^{-5}	~0
0.10	**0.71**	41.28	3.98×10^{-5}	~0
0.15	**0.76**	42.82	6.73×10^{-5}	1.43×10^{3}
0.20	**0.81**	43.06	1.28×10^{-4}	3.31×10^{3}
0.25	**0.86**	43.07	1.73×10^{-4}	1.71×10^{3}
0.30	**0.91**	42.99	1.04×10^{-4}	1.11×10^{3}
0.35	**0.96**	42.99	7.50×10^{-5}	1.09×10^{3}
0.40	**1.01**	43.16	6.26×10^{-5}	1.32×10^{3}
0.45	**1.06**	43.17	5.81×10^{-5}	1.82×10^{3}
0.50	**1.11**	41.75	5.14×10^{-5}	2.58×10^{3}
0.55	**1.16**	44.6	5.14×10^{-5}	3.56×10^{3}
0.60	**1.21**	44.89	4.46×10^{-5}	4.37×10^{3}
0.65	**1.26**	45.29	4.36×10^{-5}	5.45×10^{3}
0.70	**1.31**	45.72	4.02×10^{-5}	6.1×10^{3}
0.75	**1.36**	45.49	3.26×10^{-5}	6.92×10^{3}
0.80	**1.41**	45.37	2.84×10^{-5}	7.72×10^{3}

Table B.2 continued

E / V *vs* Ag/AgCl, pH 7	E / V *vs* RHE	R_{trap} / Ω cm^2	C_{mg}, calcd / F cm^{-2}	$R_{ct,mg}$, Ω cm^2
0.00	**0.61**	~0	3.14×10^{-6}	288140
0.05	**0.66**	~0	1.63×10^{-6}	346970
0.10	**0.71**	~0	1.63×10^{-6}	198760
0.15	**0.76**	1.43×10^{3}	1.20×10^{-6}	42554
0.20	**0.81**	3.31×10^{3}	2.70×10^{-6}	10622
0.25	**0.86**	1.71×10^{3}	1.05×10^{-5}	4489
0.30	**0.91**	1.11×10^{3}	6.72×10^{-5}	2405
0.35	**0.96**	1.09×10^{3}	1.83×10^{-4}	1444
0.40	**1.01**	1.32×10^{3}	4.66×10^{-4}	983
0.45	**1.06**	1.82×10^{3}	1.12×10^{-3}	681
0.50	**1.11**	2.58×10^{3}	1.25×10^{-3}	463
0.55	**1.16**	3.56×10^{3}		
0.60	**1.21**	4.37×10^{3}		
0.65	**1.26**	5.45×10^{3}		
0.70	**1.31**	6.1×10^{3}		
0.75	**1.36**	6.92×10^{3}		
0.80	**1.41**	7.72×10^{3}		

In Tables B.1 and B.2 C_{mg} and $R_{ct,mg}$ do not produce any data after 1.11 V because the response at 1.16 V and after only respond to the parallel circuit of C_{sc} and R_{trap} and therefore one circuit element is used producing data for those circuit elements only.

Table B.3 Table of resistance values, R_{trap} and $R_{ct,mg}$, as a function of applied potential under AM1.5 G 100 mW/cm^2 illumination in 0.5 M KB$_i$, 0.2 KCl buffer at pH 7.00.

***E* / V *vs* Ag/AgCl, pH 7**	***E* / V *vs* RHE**	**R_{trap} / Ω cm^2**	**$R_{ct,mg}$ / Ω cm^2**
0.15	0.76	143	42,554
0.20	0.81	3,311	10,622
0.25	0.86	1,715	4,489
0.30	0.91	1,106	2,405
0.35	0.96	1,089	1,444
0.40	*1.01*	*1,315*	*982*
0.45	1.06	1,824	681
0.50	1.11	2,577	462
0.55	1.16	3,555	-
0.60	1.21	4,371	-
0.65	1.26	5,447	-
0.70	1.31	6,098	-
0.75	1.36	6,916	-
0.80	1.41	7,716	-

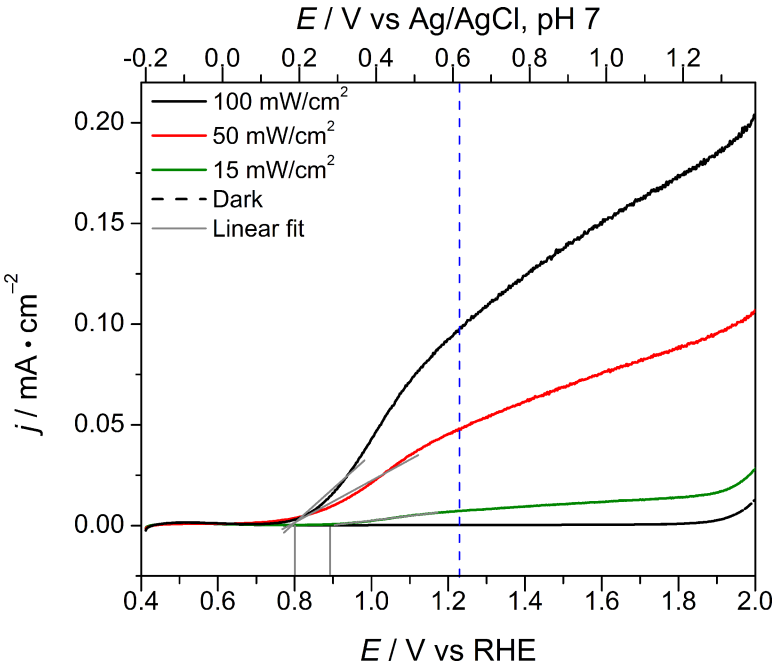

Figure B.1 LSV of $CuWO_4$ in 0.5 M KB_i, 0.2 M KCl at pH 7.00 showing linear fit line for photocurrent onset of 0.8 for 100 and 50 mW/cm^2 and 0.9 for 15 mW/cm^2. The dashed blue line at 1.23 V RHE represents the standard thermodynamic potential for water oxidation.

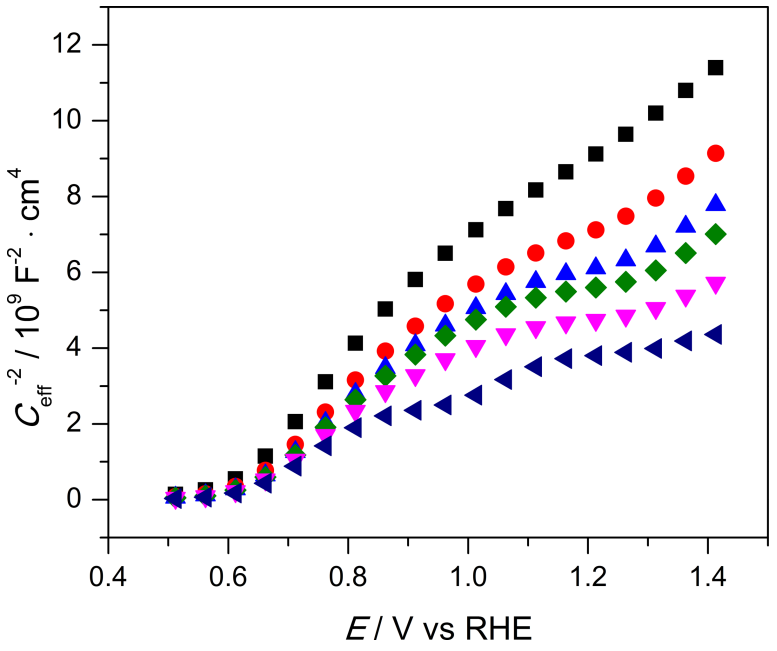

Figure B.2 Mott-Schottky analysis of EIS data on $CuWO_4$ electrodes in the dark in a 0.5 M KB_i, 0.2 KCl buffer at pH 7.00: 1164 Hz (black squares), 348 Hz (red circles), 104 Hz

(blue up triangles), 47 Hz (green diamonds), 9 Hz (pink down triangles), and 0.55 Hz (navy left triangles).

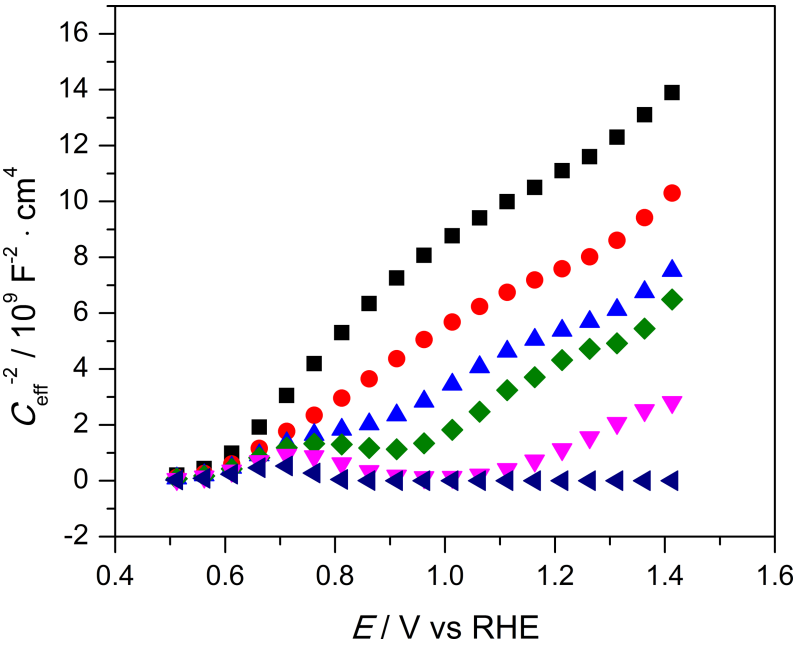

Figure B.3 Mott-Schottky analysis of EIS data on $CuWO_4$ electrodes at 100 mW/cm^2 in a 0.5 M KB_i, 0.2 KCl buffer at pH 7.00: 1164 Hz (black squares), 348 Hz (red circles), 104 Hz (blue up triangles), 47 Hz (green diamonds), 9 Hz (pink down triangles), and 0.55 Hz (navy left triangles).

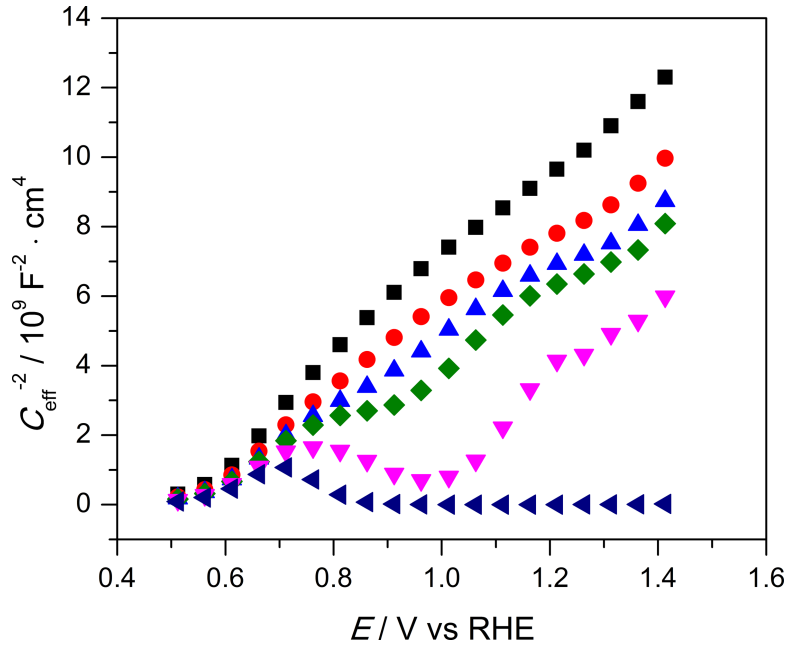

Figure B.4 Mott-Schottky analysis of EIS data on $CuWO_4$ electrodes at 50 mW/cm^2 in a 0.5 M KB_i, 0.2 KCl buffer at pH 7.00: 1164 Hz (black squares), 348 Hz (red circles), 104

Hz (blue up triangles), 47 Hz (green diamonds), 9 Hz (pink down triangles), and 0.55 Hz (navy left triangles).

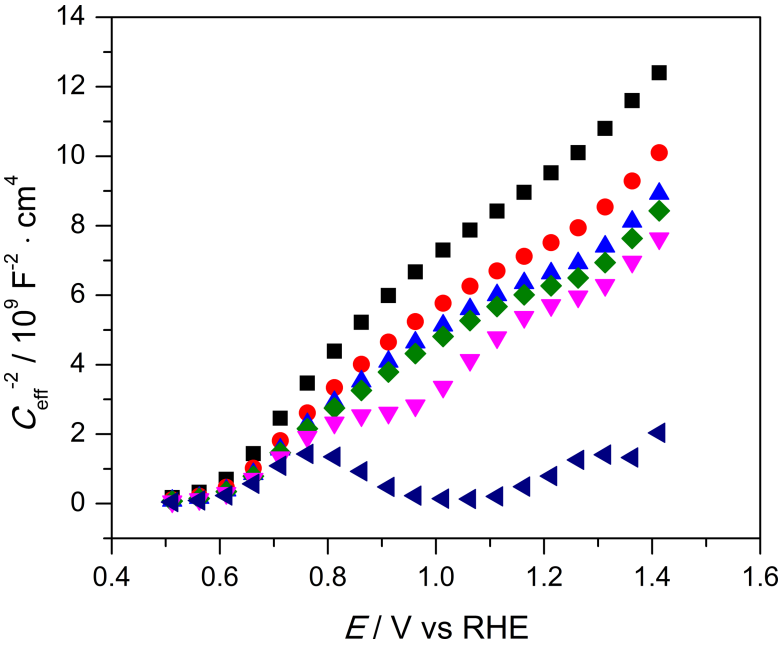

Figure B.5 Mott-Schottky analysis of EIS data on $CuWO_4$ electrodes at 15 mW/cm^2 in a 0.5 M KB_i, 0.2 KCl buffer at pH 7.00: 1164 Hz (black squares), 348 Hz (red circles), 104 Hz (blue up triangles), 47 Hz (green diamonds), 9 Hz (pink down triangles), and 0.55 Hz (navy left triangles).

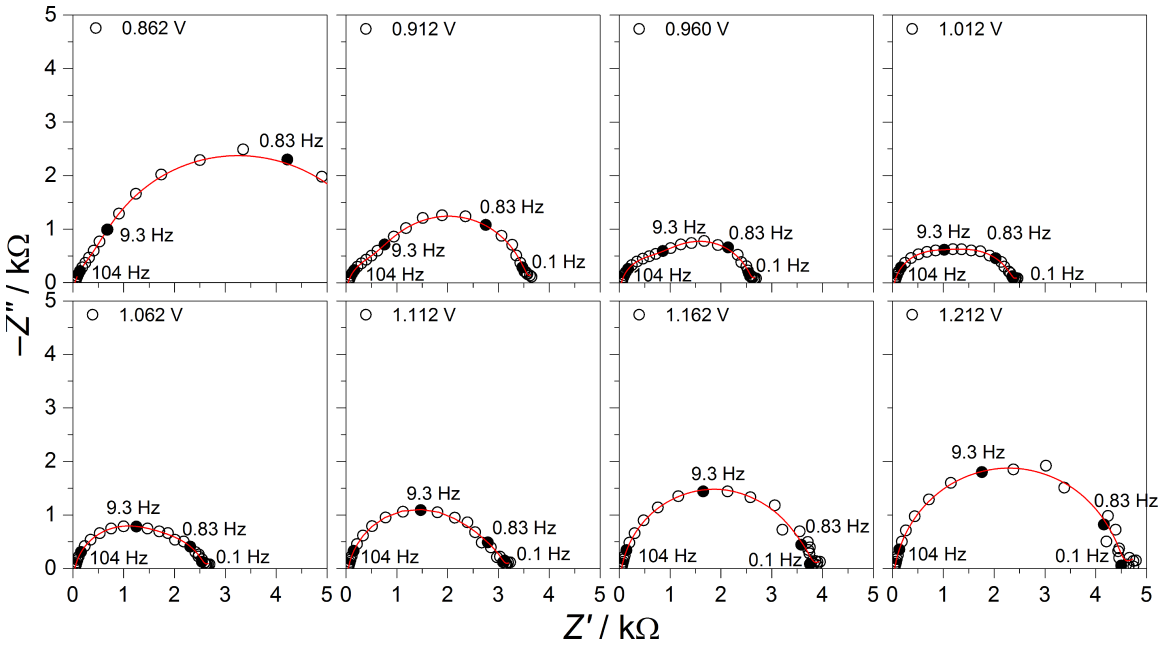

Figure B.6 Nyquist plots from 0.86-1.21 V *vs* RHE including fit lines under 100 mW/cm^2 AM1.5G illumination in a 0.5 M KB_i, 0.2 KCl buffer at pH 7.00.

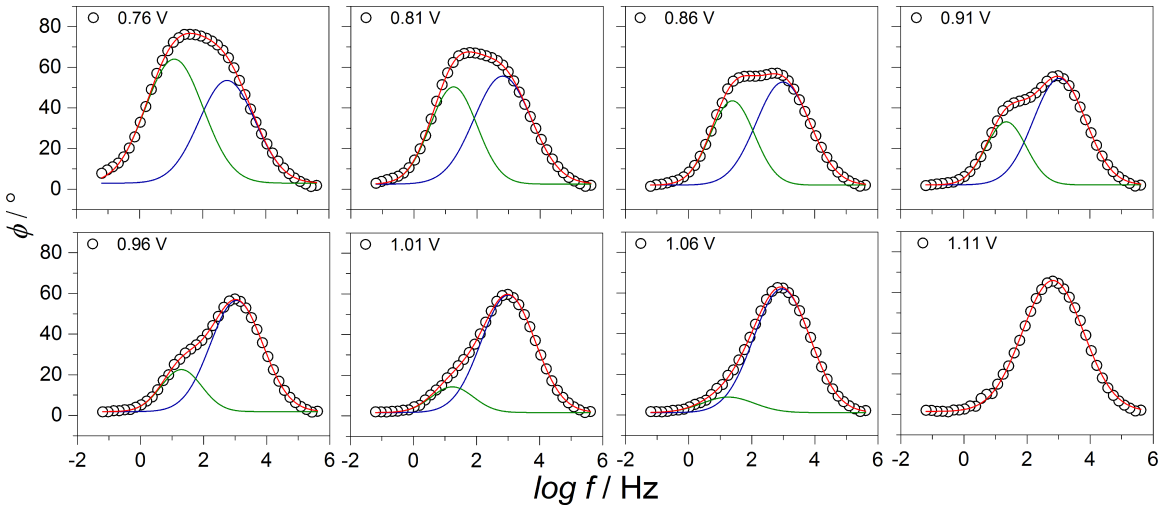

Figure B.7 Bode plots from 0.76-1.11 V *vs* RHE including fit lines for Gaussian multiple peak fit under 100 mW/cm^2 AM1.5G illumination in a 0.5 M KB$_i$, 0.2 KCl buffer at pH 7.00.

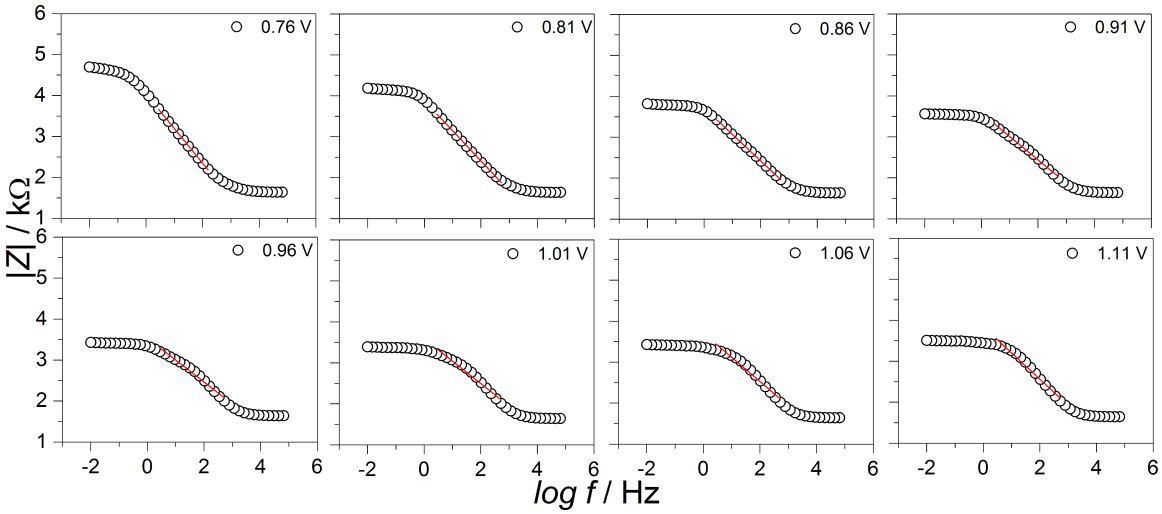

Figure B.8 Bode plots of total impedance (|*Z*|) from 0.76-1.11 V *vs* RHE including slope lines for linear fit (red line) under 100 mW/cm^2 AM1.5G illumination in a 0.5 M KB$_i$, 0.2 KCl buffer at pH 7.00.

Table B.4 Slope values for Bode plots for total impedance (|*Z*|)

E / V *vs* Ag/AgCl, pH 7	*E* / V *vs* RHE	Slope
0.15	0.76	-0.85
0.20	0.81	-0.74
0.25	0.86	-0.65
0.30	0.91	-0.57
0.35	0.96	-0.53
0.40	1.01	-0.54
0.45	1.06	-0.59
0.50	1.11	-0.64

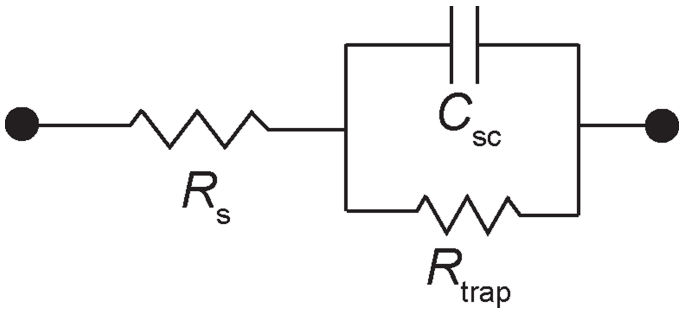

Figure B.9 Randles circuit used to fit the single semicircle observed at 1.16 V and above in the EIS under illumination. R_s represents the solution resistance and electrode resistance in this circuit and the circuit in Figure 3.1b.

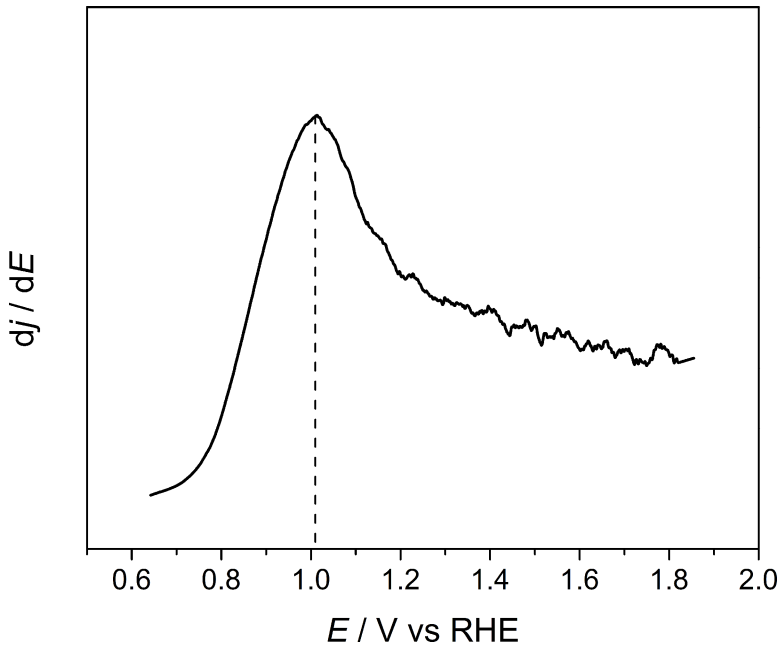

Figure B.10 Derivative of LSV curve at 100 mW/cm^2 in pH 7 borate buffer showing greatest change in photocurrent occurs at 1.01 V vs RHE, 0.4 V vs Ag/AgCl at pH 7.00.

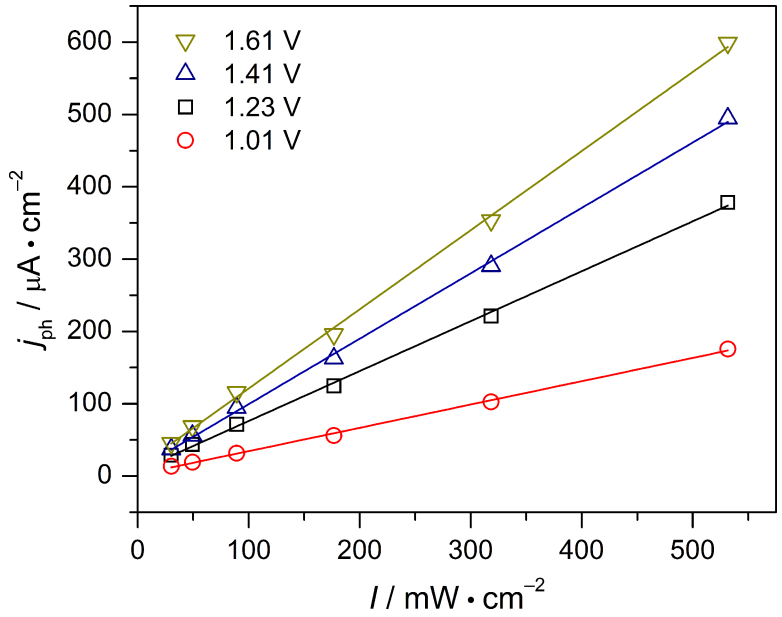

Figure B.11 j_{ph} as a function of illumination intensity of $CuWO_4$ at constant applied potential in 0.5 M KB$_i$, 0.2 M KCl at pH 7.00.

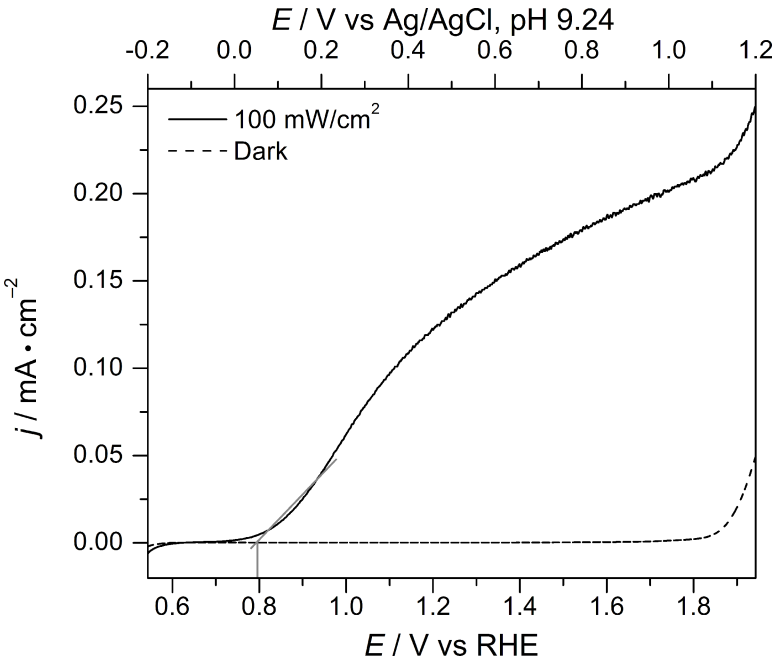

Figure B.12 LSV of $CuWO_4$ in pH 9.24 KB_i buffer (0.5 M, 0.2 M KCl) at 100 mW/cm^2. Onset potential identified as 0.79 V *vs* RHE.

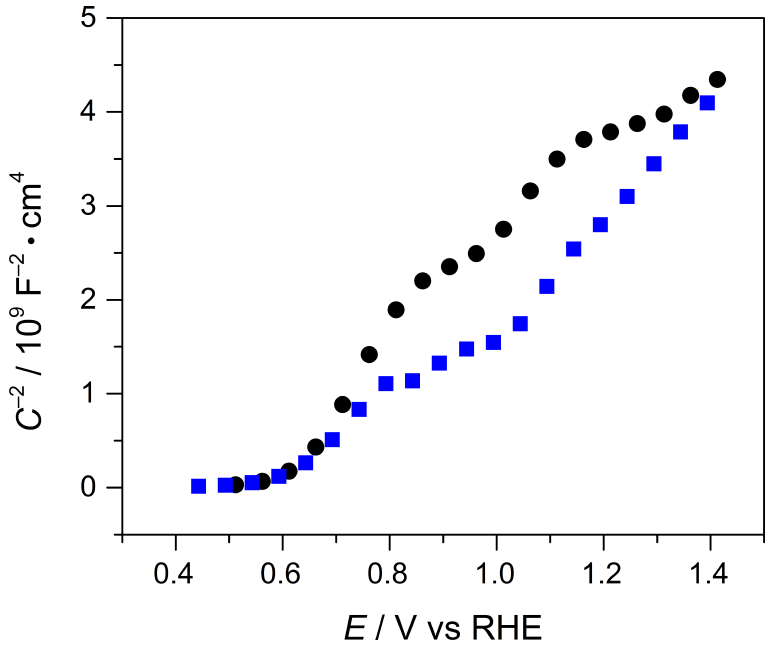

Figure B.13 Mott-Schottky analysis of EIS data on $CuWO_4$ electrodes in the dark in a 0.5 M KB_i, 0.2 KCl buffer at pH 7.00 (black circles) and 9.24 (blue squares) at 0.55 Hz.

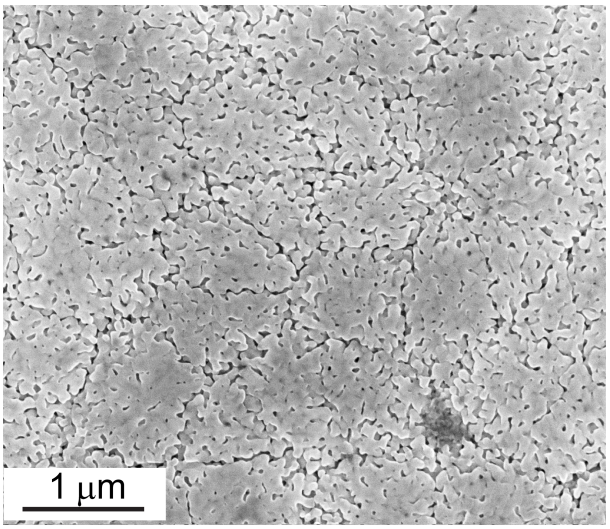

Figure B.14 Representative SEM of $CuWO_4$ thin film.

---

1. Orazem, M.E.; Tribollet, B. *Electrochemical Impedance Spectroscopy*, John Wiley & Sons, Inc., 2008; Chp. 13; pp. 233-234
2. Orazem, M.E.; Tribollet, B. *Electrochemical Impedance Spectroscopy*, John Wiley & Sons, Inc., 2008; Chp. 17; p. 335

Appendix C

Supporting data for Chapter 4

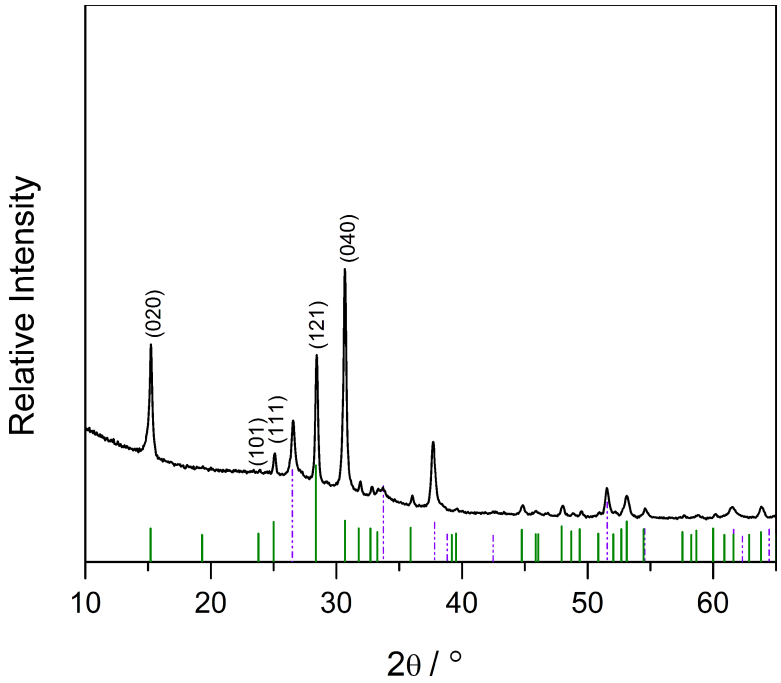

Figure C.1 X-ray diffraction of $WO_3 \bullet H_2O$ conversion to α-$SnWO_4$ at pH 1. FTO peaks are represented by the violet dashed vertical lines and α-$SnWO_4$ is represented by the green vertical lines.

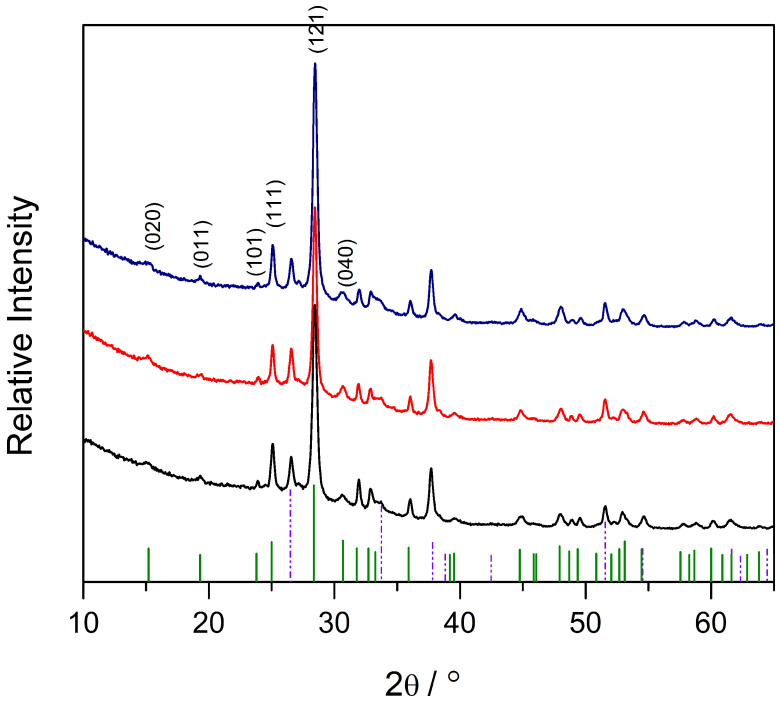

Figure C.2 X-ray diffraction patterns of pure α-$SnWO_4$ films converted from WO_3•H_2O. From the bottom to the top the pH of the hydrothermal solution was pH 3 (black), pH 4 (red), and pH 5 (blue). FTO peaks are represented by the violet dashed vertical lines and α-$SnWO_4$ is represented by the green vertical lines.

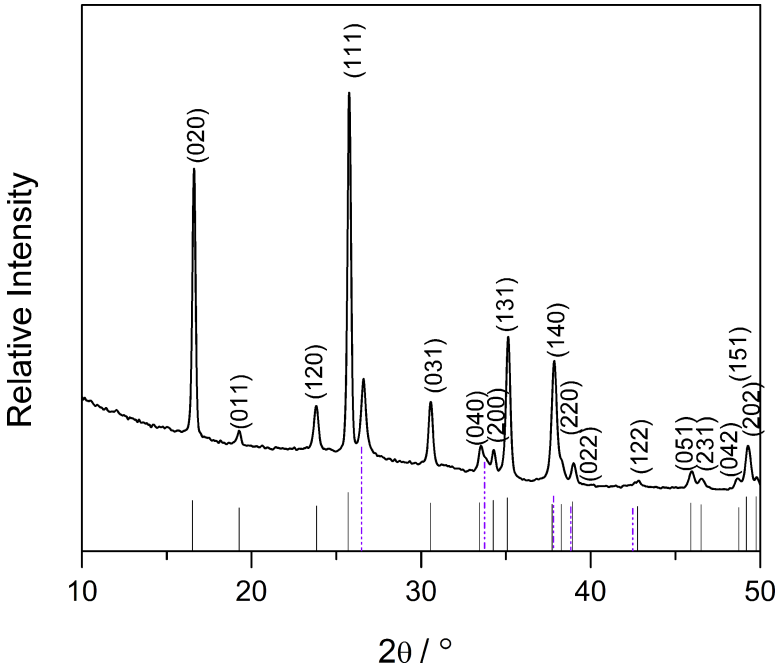

Figure C.3 X-ray diffraction of WO_3•H_2O represented by black vertical lines. FTO peaks are represented by the violet dashed vertical lines.

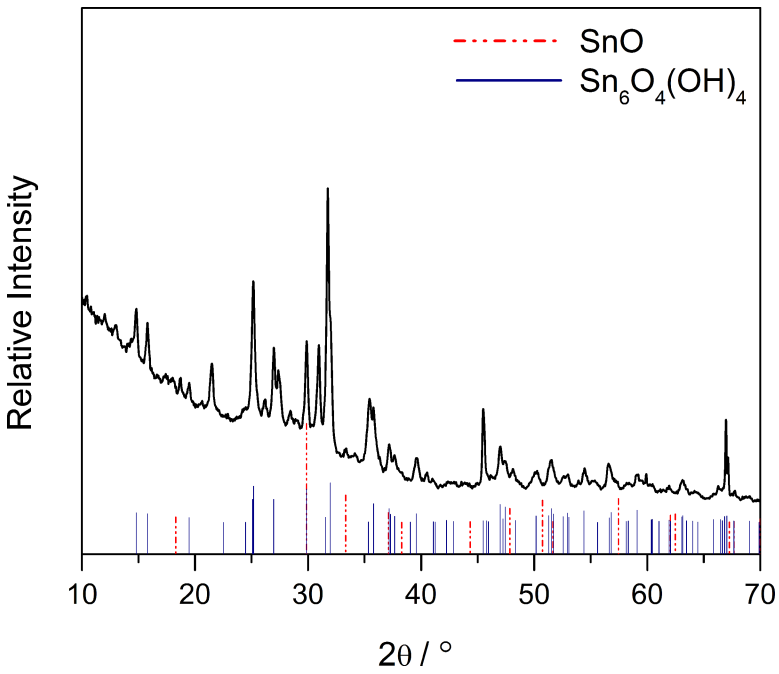

Figure C.4 X-ray diffraction of precipitate collected after hydrothermal conversion of WO_3 to α-$SnWO_4$ using NaOH and HCl for pH adjustment. The dotted red lines index to SnO (Jade PDF#85-0423) and blue vertical lines index to $Sn_6O_4(OH)_4$ (Jade PDF#84-2157).

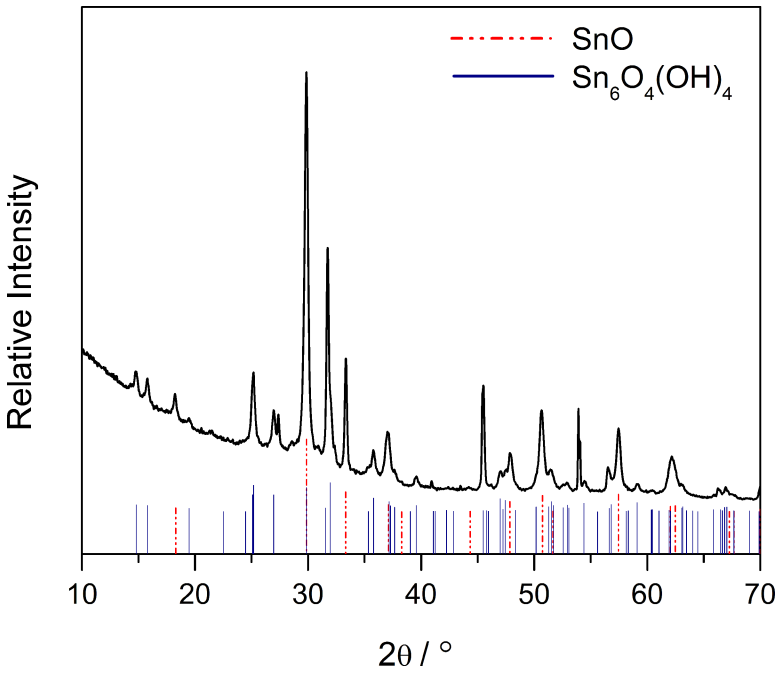

Figure C.5 X-ray diffraction of precipitate collected after hydrothermal conversion of WO_3 to α-$SnWO_4$ using only NaOH for pH adjustment. The dotted red lines index to SnO (Jade PDF#85-0423) and blue vertical lines index to $Sn_6O_4(OH)_4$ (Jade PDF#84-2157).

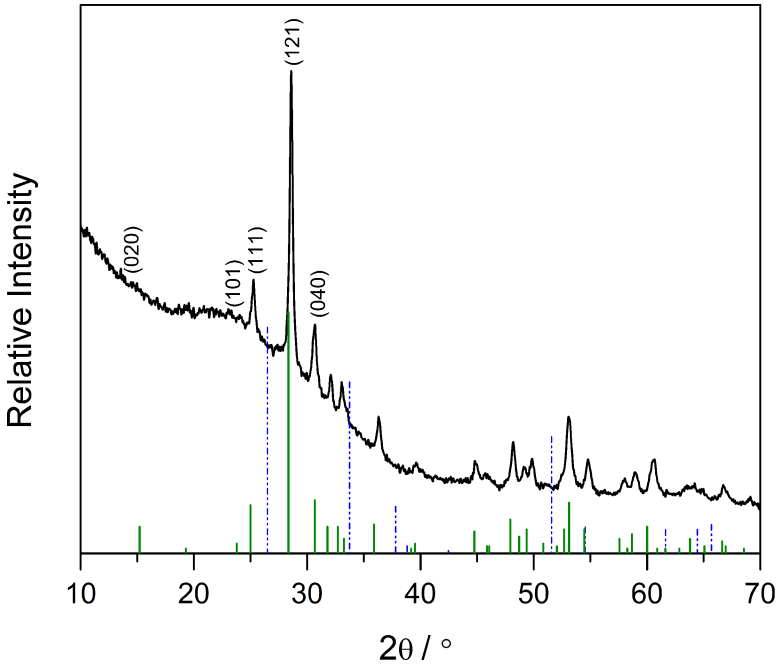

Figure C.6 X-ray diffraction of α-$SnWO_4$ material removed from film surface. Violet dotted lines represent index to SnO_2 and the green vertical lines represent α-$SnWO_4$.

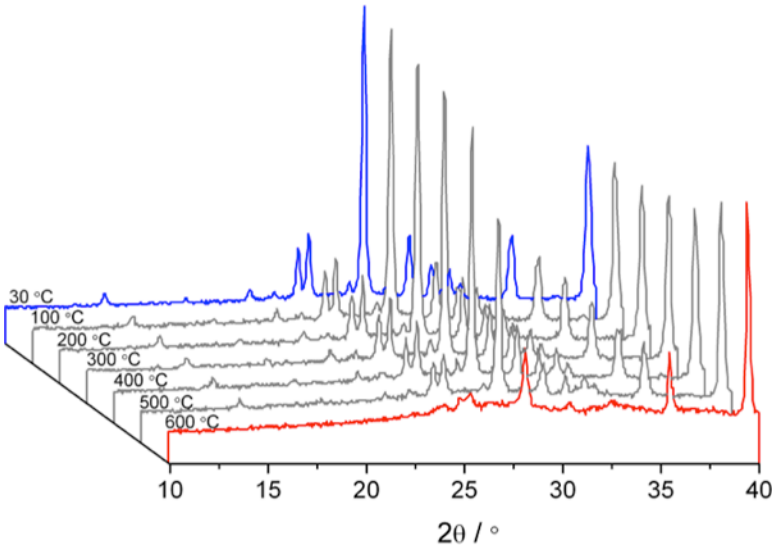

Figure C.7 Temperature XRD taken of α-$SnWO_4$ powder synthesized by coprecipitation of a 1:1 mol precursor of $SnCl_2$ and Na_2WO_4 and annealed in a vacuum sealed ampoule at 650 °C for 8 hours. The temperature was increased from 30-600 °C in an air atmosphere and degradation of the material is observed.

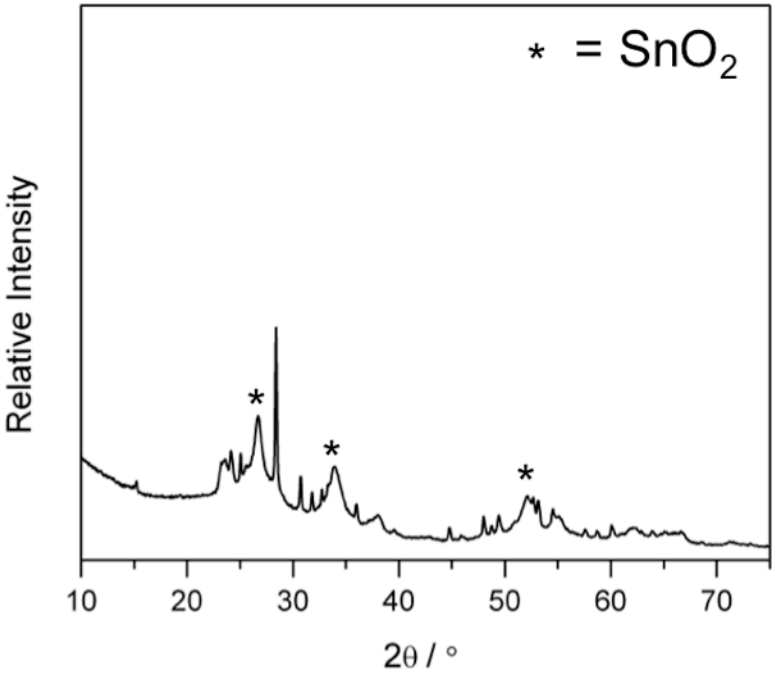

Figure C.8 X-ray diffraction of α-$SnWO_4$ powder annealed at 600 °C in air for 2 hours.

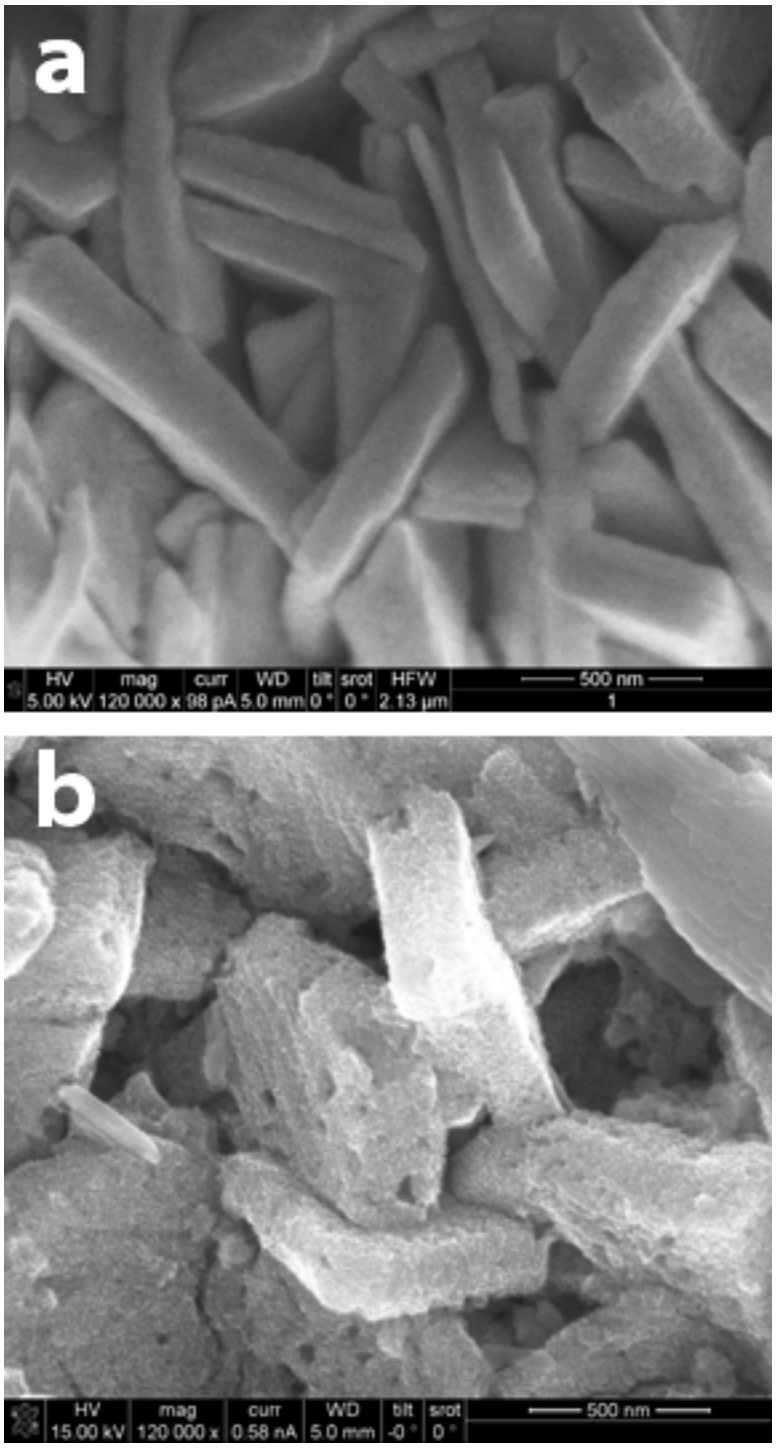

Figure C.9 a) SEM images of WO_3 nanoplatelet film before α-$SnWO_4$ hydrothermal reaction b) Pure α-$SnWO_4$ film after hydrothermal reaction at pH 3.

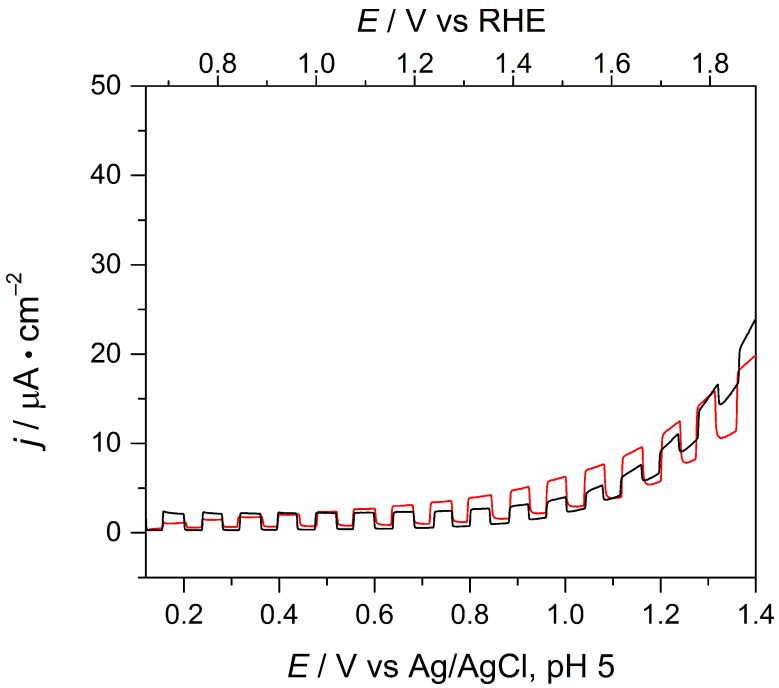

Figure C.10 Chopped light linear sweep voltammogram of α-$SnWO_4$ thin films produced at pH 4 (black) and pH 7 (red) in 0.1 M KP_i buffer at pH 5 and AM1.5G irradiation at 100 mW/cm^2.

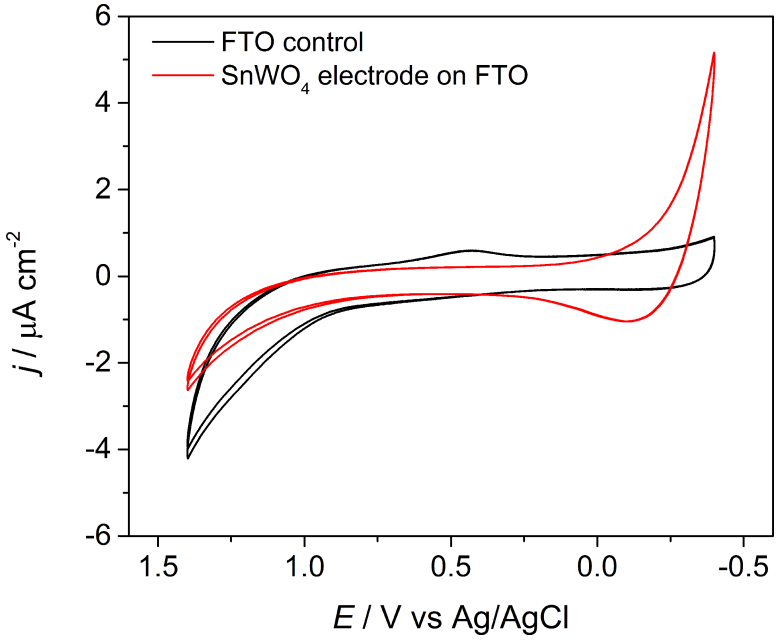

Figure C.11 Cyclic voltammogram (CV) of α-$SnWO_4$ in air free and dry acetonitrile solution (red) in 0.1 M $TBAPF_6$ supporting electrolyte. CV of FTO control is in black. Film used was synthesized at pH 1.

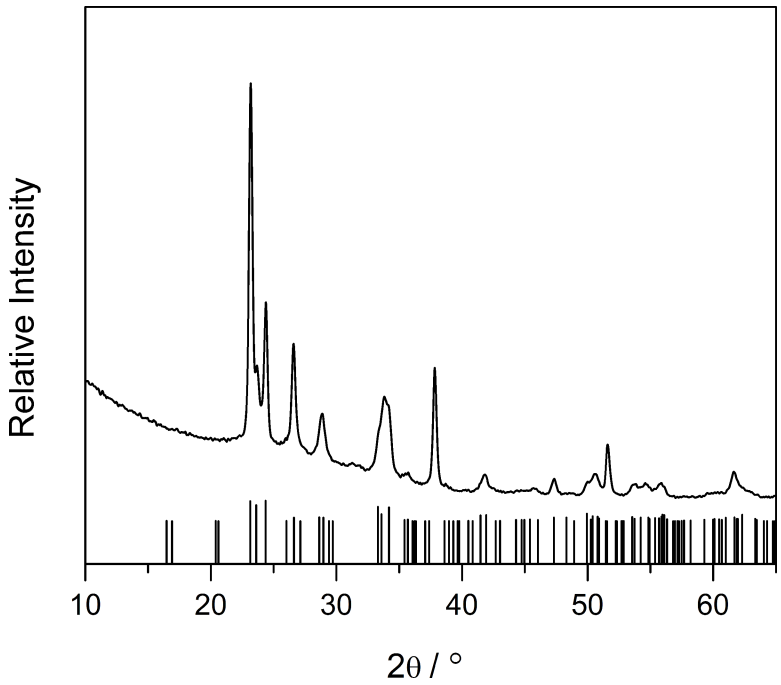

Figure C.12 X-ray diffraction of monoclinic WO_3 obtained by annealing hydrothermally grown $WO_3 \bullet H_2O$ at 450 °C for 1 hour. The black lines index to monoclinic WO_3 (Jade PDF#72-1465).

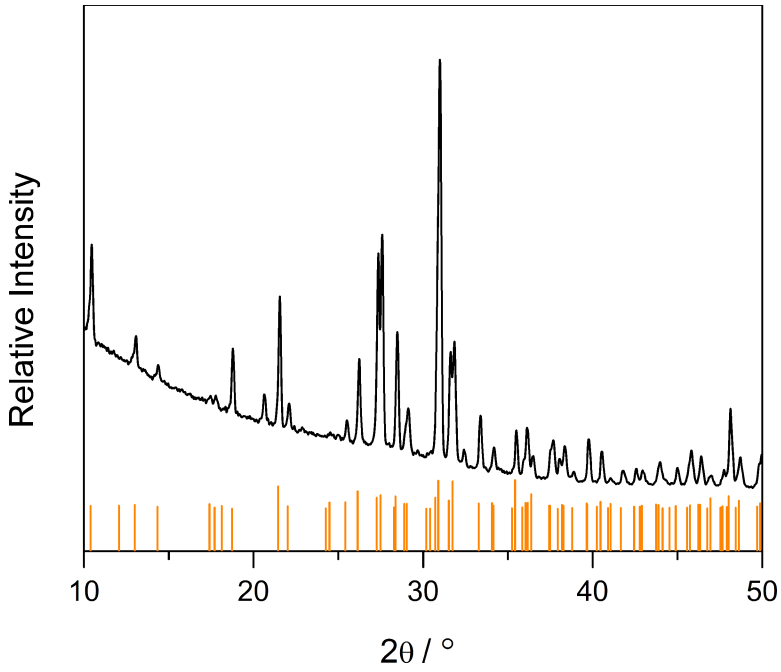

Figure C.13 X-ray diffraction of $SnWO_4$ films pre-acid treatment. The orange lines index to $Sn_{21}Cl_{16}(OH)_{14}O_6$ (Jade PDF#35-0907).